Universidade de Aveiro Departamento de Física
Ano 2011

João Nuno Santos Gonçalves

Medida e modelização de propriedades hiperfinas em materiais ferróicos

Measurement and modeling of hyperfine properties in ferroic materials

Universidade de Aveiro Departamento de Física
Ano 2011.

João Nuno Santos Gonçalves

Medida e modelização de propriedades hiperfinas em materiais ferróicos

Measurement and modeling of hyperfine properties in ferroic materials

Tese apresentada à Universidade de Aveiro para cumprimento dos requisitos necessários à obtenção do grau de Doutor em Física, realizada sob a orientação científica do Doutor Vítor Brás de Sequeira Amaral, Professor Catedrático do Departamento de Física da Universidade de Aveiro e do Doutor João Guilherme Martins Correia, Investigador Principal do Instituto Tecnológico e Nuclear.

To my family

o júri

presidente

Prof. Doutor Mário Guerreiro Silva Ferreira
professor catedrático da Universidade de Aveiro

Prof. Doutor Tilman Butz
prof. doutor rer. nat. habil, Institut für Experimentelle Physik II – Nukleare Festkörperphysik Linnéstrasse, Universität Leipzig

Prof. Doutor Vítor José Babau Torres
professor catedrático da Universidade de Aveiro

Doutor Alessandro Stroppa
investigador da Universitá degli Studi dell'Aquila

Doutora Armandina Maria Lima Lopes
investigadora do Centro de Física Nuclear da Universidade de Lisboa

Doutor João Guilherme Martins Correia
investigador principal do Instituto Tecnológico e Nuclear, Physics Department – CERN

Prof. Doutor Vítor Brás de Sequeira Amaral
professor catedrático da Universidade de Aveiro

agradecimentos

I thank my supervisors Prof. Dr. Vítor Amaral and Dr. João Guilherme Correia for their enthusiastic and very supportive guidance.

At Universidade de Aveiro, Rosário Soares and Dr. Soma Das helped with X-ray and magnetization measurements.

At CERN, Tânia Mendonça helped in many of my PAC measurements, and Dr. Armandina Lopes in PAC theory and measurements, but other fellow colleagues who helped in the beam-times, unfortunately too many to name here, all have my thanks.

Prof. Dr. Pedro Tavares provided synthesis and useful discussions of manganite samples.

I thank Dr. Heinz Haas for his helpful assistance with the use of WIEN2k.

Tânia Mendonça and Dr. André Pereira involved me in some of their interesting studies.

Dr. Alessandro Stroppa invited me to work in a great research environment at L'Aquila, and I thank him for his supervision in the work with ferroelectrics. I also thank Prof. Dr. Tilman Butz, for his useful contribution and discussion in this work.

Finally, I sincerely thank all my colleagues for their friendship.

I acknowledge FCT for the PhD grant.

palavras-chave hiperfina, magnetismo, manganites, ferroeléctrico, polarização, PAC, DFT

resumo

Esta tese apresenta os resultados de experiências de correlações angulares perturbadas (PAC), uma técnica experimental que mede as interacções hiperfinas em sondas - iões radioactivos implantados nos materiais a estudar, o que permite inferir informação local à escala de dimensões atómicas. Foram também utilizados cálculos ab-initio utilizando a teoria de funcionais da densidade electrónica, obtendo resultados que complementam directamente as experiências, e outros resultados também usados para investigação teórica.

Estes métodos foram aplicados em duas famílias de materais. As manganites, com a possível existência de ordens magnéticas, de carga, orbital e ferroeléctrica, têm interesse fundamental e tecnológico. Cálculos iniciais na manganite de Ca provam a sua utilidade como complemento de experiências PAC neste tipo de materiais. Os resultados experimentais são depois obtidos nas manganites de terra-alcalina- Ba e Sr, com especial interesse estrutural devido à variedade de polimorfos possíveis. Com as sondas de Cd e In conseguiu-se estabelecer localização dos iões de sonda e a sua estabilidade num intervalo de temperatura grande, e uma comparação com os cálculos permite a interpretação mais aprofundada dos resultados. Cálculos das propriedades hiperfinas nas manganites de terras-raras também são apresentados. O segundo tipo de materiais em que foram estudadas as propriedades hiperfinas são os pnictídeos de Manganês: MnAs, MnSb, e MnBi. Os resultados experimentais obtidos consideram principalmente o MnAs, cuja transição magneto-estrutural tem maior interesse. A transição foi estudada em detalhe com a resolução local da técnica, com a obtenção de informação do carácter da transição, também com o complemento de outras técnicas mais convencionais.

O último estudo desenvolvido nesta tese utiliza apenas os cálculos de primeiros princípios, continuando com o tema das interacções hiperfinas, mas desta vez em relação com a ferroelectricidade. São considerados vários óxidos com metais de transição com estruturas de perovskite ou distorcidas. O gradiente de campo eléctrico existente devido à interacção quadrupolar nos núcleos é relacionado com a polarização eléctrica espontânea, que é a principal quantidade medida em ferroeléctricos. Este estudo dá uma base fundamental teórica a alguns estudos empíricos antigos, sugerindo novas direcções de investigação em ferroeléctricos e multiferróicos utilizando técnicas de medida do gradiente de campo eléctrico.

keywords hyperfine, magnetism, manganites, ferroelectric, polarization, PAC, DFT

abstract

This thesis presents the results of perturbed angular correlation (PAC) experiments , an experimental technique which measures the hyperfine interaction at probes (radioactive ions implanted in the materials to study), from which one infers local information on an atomic scale. Furthermore, ab-initio calculations using density functional theory electronic obtain results that directly complement the experiments, and are also used for theoretical research.

These methods were applied in two families of materials. The manganites, with the possible existence of magnetic, charge, orbital and ferroelectric orders, are of fundamental and technological interest. The experimental results are obtained in the alkaline-earth manganites (Ca, Ba, Sr), with special interest due to the structural variety of possible polymorphs. With probes of Cd and In the stability of the probe and its location in a wide temperature range is established and a comparison with calculations allows the physical interpretation of the results. Calculations of hyperfine properties in rare-earth manganites are also presented. The second type of materials in which hyperfine properties were studied are the Manganese pnictides: MnAs, MnSb, and MnBi, compounds in which magnetism is fundamental. The experimental results obtained mainly consider the MnAs compound, whose magneto-structural transition is of great interest. The transition is analyzed in detail with the local resolution characteristic of the technique, obtaining information of the character of the transition also with complementary, more conventional techniques.

The last work in this thesis uses only the first principles calculations, continuing the theme of the hyperfine interactions, but this time with respect to ferroelectrics. Several transition metal oxides with perovskite or distorted structures are considered. The electric field gradient which exists due to the quadrupole interaction in nuclei is related to the spontaneous electric polarization, the main quantity measured in ferroelectrics. This study provides a fundamental theoretical basis for previous empirical studies, suggesting new directions for research in ferroelectrics and multiferroics using techniques which measure the electric field gradient.

Contents

List of acronyms

CMR	Colossal Magnetoresistance
DOS	Density of States
DFT	Density Functional Theory
EFG	Electric Field Gradient
GGA	Generalized Gradient Approximation
ISOLDE	Isotope Separator On-Line
L/APW+lo	Linear/Augmented Plane Wave plus local orbitals method
LDA	Local Density Approximation
LSDA	Local Spin Density Approximation
MHF	Magnetic Hyperfine Field
NMR	Nuclear Magnetic Resonance
NQR	Nuclear Quadrupole Resonance
PAC or TDPAC	Time-Differential γ-γ Perturbed Angular Correlation spectroscopy
PAW	Projector Augmented-Wave method
PBE	Perdew-Burke-Ernzerhof parameterization of the GGA
VASP	Vienna Ab-initio Simulation Package
XRD	X-Ray Diffraction
WC	Wu-Cohen parametrization of the GGA

Chapter 1

Introduction and Thesis Outline

This thesis reports on research done from January 2008 until the end of 2011, at the Physics Department of Universidade de Aveiro, and at the ISOLDE-CERN (Isotope Separator On-Line) isotope production and implantation facilities, and associated solid-state physics laboratory.

The work here developed fits within the concept of the author's group, while using local probe nuclear techniques to study atomic scale phenomena in materials of interest, and, in a complementary way, the simulation of such properties. Looking forward to extend the analysis and interpretation capabilities, the present work presents simulations and measurements of hyperfine properties, by using some of the most accurate methods available.

The experimental part of the work concerns mainly the use of time-differential $\gamma-\gamma$ Perturbed Angular Correlation (PAC) spectroscopy (at the isotope separator on-line (ISOLDE) facility at CERN). The information obtained from this spectroscopy technique results from the hyperfine interaction of nuclear moments of excited nuclear states with their magnetic and charge local environment. In this case, radioactive isotopes with appropriate excited states are implanted into the samples to study.

The local information obtained with these probes may be unique and essential in many materials, in which it is thought that very local (atomic or nano scale) phenomena are key factors to understand the emergent physical properties, *e.g.* in colossal magnetoresistance manganites [1], multiferroics, or energetically frustrated materials, where different types of charge, spin, orbital, and lattice interactions correlate and compete.

The theoretical part of the work uses Density Functional Theory (DFT) calculations [2, 3]. Nowadays, development of computing power and sophisticated first-principles algorithms using powerful numerical methods allow accurate prediction of numerous interesting and useful material properties. New materials do not need to be created and studied, and the use of computations also gives the opportunity to investigate separate degrees of freedom; examples: only variation of a certain structural parameter is taken into account, or only variation in magnetic order is considered keeping the structure constant, or pressure variation, with a control and depth that is often not possible in experiments.

However, there is not a magic tool with advantages, without any limitation, and many cases are not yet fully understood using DFT calculations where the interpretation of the results is

still not straightforward. For example, among other things, Mott-like insulators and van der Waals forces are not well described with standard local and semi-local density approximations, although more sophisticated exchange-correlation approximations have been proposed to deal with these problems. But even disregarding fundamental limitations of the approximations used, in complex materials where many factors compete with equal weight to the determination of the stable states, technical limitations such as the numerical accuracy provided by a given code may become limiting. On the other hand, experimental hyperfine measurements suffer a difficult direct or poor empirical interpretation, without some kind of theoretical basis. Often the combination of experimental hyperfine measurements with the information taken from DFT calculations is the best approach required to do a confident analysis. Therefore, the larger part of this thesis conveniently provides both experiment and theory. In the present case, PAC experiments are the first motivation for the calculations, also working as a cross check of the calculated values, and the theory provides the underlying physical explanation, with complementary physical insight of different properties.

The sectioning and presentation of this work has a strong basis on previously prepared articles on similar topics. However, the work still pertains to different families of compounds, and some fragmentation of content was unavoidable. Nevertheless, there is a great degree of similarity, not only in the methods applied - mainly PAC and first-principles calculations - but as well as by providing an integrated analysis of the different results in the themes adressed, namely: transition-metal oxides (manganites and perovskite ferroelectrics), magnetism due to manganese and its interplay with other degrees of freedom (manganites and manganese pnictides).

The organization of this thesis report adopts new directives where the development of explanations of subjects and methods is reduced to reasonable minima when appropriate. Hence, the next chapter briefly presents the main techniques and references with no exhaustive survey of the methods. Still, the technical knowledge aspects, which are important for a deeper comprehension of the subsequent results, are presented.

The following chapters, embracing the results and discussion, are divided according to the different classes of materials studied: chapter 3 concerns the trioxide manganese based compounds commonly known as manganites. After an introduction to the whole chapter, section 3.2 consists of the exact reproduction of a published article [4] where DFT calculations of the electric field gradients and electronic structure study $CaMnO_3$. This is a natural starting point of the calculations, since there was already a considerable amount of experimental ^{111m}Cd/^{111}Cd & ^{111}In/^{111}Cd PAC data in $CaMnO_3$ and similar Ca based compounds [5, 6], which could be compared to theory. It serves also as an introduction to the subsequent experimental work in the other alkaline-earth manganites. The experimental PAC value in $CaMnO_3$ was successfully calculated while gaining more insight for the limitations and abilities of DFT calculations when applied to this topic and compound. The results presented in this section are also relevant to the previously studied Cd based manganites [7], since some calculations consider very high concentrations of Cd ($Cd_{0.5}Ca_{0.5}MnO_3$). However, this will not be explored in this thesis. The situation of very low Cd concentrations, corresponding to the highly diluted impurity limit used in the PAC measurements, is more relevant for our analysis.

The work on other alkaline-earth manganites ($SrMnO_3$ and $BaMnO_3$) is presented in section 3.3, and makes use of DFT calculations, with similar methods to those used in section 3.2, presenting, however, a more detailed study. In addition, PAC studies were conducted and complemented by magnetization and X-ray diffraction measurements. $BaMnO_3$ and $SrMnO_3$ are more complex, at least from the structural point of view, since they form hexagonal polymorphs, distorted forms of the basic perovskite structure. Many phases can be formed with different layer packing configurations of MnO_6 octahedra, and the amount of each phase depends sensitively on the synthesis conditions. Since one of the main purposes of this study was a direct comparison of experiment with theory, the emphasis was placed on mostly single-phase samples with simple structures. The $SrMnO_3$ form obtained, 4H, is relatively simple, while $BaMnO_3$, 6H, and especially 15R are notoriously more complex, with more atoms per unit cells, due to the higher number of atomic layers in the hexagonal c axis. The computational study presented is more detailed in the $SrMnO_3$ phase, where the simpler interpretation and better agreement with experiments are also achieved (the calculations consider the ^{111m}Cd probes used in the PAC experiments with Cd impurities diluted in supercells of 4H-$SrMnO_3$). The PAC results obtained in $BaMnO_3$ are more intriguing, with multiple observed electric field gradients, some agreeing perfectly with theory, for regular Cd cations on the lattice, but also small fractions which cannot be explained by the calculations considered and remain out of the scope of the interpretation, probably due to point defects not considered.

There is now great interest in the so-called multiferroics: materials where magnetic and electric orders coexist and couple, holding promises, for instance, in the creation of new functional devices or high density memory capacity [8, 9]. The rare-earth manganites, possessing both magnetic and ferroelectric orders at low temperatures, are examples which allow us to study this phenomenon. A last section in chapter 3 is devoted to the small radius rare-earth manganites ($YMnO_3$, $HoMnO_3$, $ErMnO_3$, $LuMnO_3$). These compounds present hexagonal structures, distinct from the perovskite based structures of other manganites [10]. The denser orthorhombic phases of these compounds can also be synthesized [11] in high-pressure or soft-chemistry conditions. Both forms exhibit interesting multiferroic properties [12, 13]. Whereas the orthorhombic phases are not the object of the current study, the hyperfine parameters still provide an opportunity to observe the local structure, with the potential to improve our understanding of the mechanisms at play in the coupling of the various orders. Profiting from the existing experimental work on the hexagonal manganites, within the author's group [14], we address the hyperfine parameters as studied by DFT calculations, which are quite sensitive to the exact calculation method and description of the compounds. This is a taste of the increased degree of difficulty due to materials complexity. Therefore, different calculations are tested, varying e.g. the magnetic order, structure, electronic correlations, and analysing the influence of these degrees of freedom in the hyperfine parameters. This chapter is mostly a speculative study, although some aspects of comparison with PAC experiments are explored in the last section.

Chapter 4 (peer-reviewed article [15], except for the appendix) continues with this methodology but a different family of compounds is studied: the manganese pnictides MnAs, MnSb, and MnBi. Special attention is given to MnAs, reflecting a larger interest in this system from

the scientific community in recent years. Some similarity is seen between MnAs and manganites, since there is, *e.g.* , a magnetoresistance effect, and other effects resulting from the interplay of magnetic and structural orders, such as spin-phonon coupling and magnetocaloric effect. The main result from experimental studies is a detailed analysis of the phase transition at an atomic scale. The calculations confirm a simple substitutional picture for the local probe used in the experiments (^{77}Br/^{77}Se), and give a general picture for the electronic structure of the manganese pnictides, improving previous calculations.

Chapter 5 is different both in the methods applied and in the studied properties of the materials. Calculations of spontaneous polarization are performed for a series of perovskite oxide structures, such as the classic ferroelectrics $BaTiO_3$ and $PbTiO_3$. In contrast with the previous topics, the magnetism is not an important degree of freedom in these compounds, where metal ions in the perovskite structures have formally empty *d*-shells. The original part of this chapter is solely based on DFT calculations. Nevertheless, some of the results focus on existing materials and are obviously compared with the relevant existing experimental results. While these materials are extensively studied, and both their ferroelectric properties and hyperfine parameters were measured in a variety of conditions, the relation between them was not considered except in a few works where experiments were compared to empirical models. The analysis presented here provides another point of view for this relation, based on *ab-initio* simulations, and showing a clear relationship between the electric field gradients and polarization.

The two specific methods which were used in this thesis for the implementation of DFT are: the projected augmented-wave (PAW) method, and the linear augmented plane wave method, respectively, with the VASP [16] and WIEN2K [17] codes. The first purpose of this work is the direct comparison of the quantities measured with PAC (electric field gradients and hyperfine fields), with the results from calculations, for which WIEN2K is the most tested code. However, the calculation of the electric polarization is more easily achievable with VASP, using the modern theory [18, 19].

The work presented in this thesis received financial support by research projects POCI/FP/81979/2007, CERN/FP/83643/2008, FP-109357-2009, CERN-FP-109272-2009, PTDC/FIS/105416/2008, CERN/FP/116320/2010, Isolde projects, EURONS, ENSAR, the AQUIFER research program at Universitá L'Aquila, and the FCT PhD grant SFRH/BD/42194/2007.

Chapter 2

Methods

2.1 Experimental radioactive methods

At the ISOLDE-CERN facility, where part of the work was done, high purity beams of a large variety of isotopes are produced by sending a 1 GeV proton beam to a target, where n-spallation, fragmentation, and fission reactions originate the isotopes. They are then separated according to their mass by magnetic fields and delivered as a low energy (< 60 keV) beam to different experiments. The probe nuclei are then implanted in very dilluted concentrations (at most, parts per million), therefore impurity-impurity interactions are negligible, and high solubility of the impurity probe in the host is not necessary, aiming to keep the probe element from changing the properties of the host material.

Still, ion implantation may create point defects, thus reducing the accuracy of the intended measurements. In order to minimize this effect it may be enough to anneal the sample, such that ideally the added thermal energy promotes the probes and their local surroundings to their equilibrium positions. This is done in high temperature furnaces typically at $\sim$ 700-1000 C, depending on the characteristics of the chosen sample, under controlled atmospheres.

The time-differential γ-γ perturbed angular correlation technique (PAC) uses radioactive isotopes and measures their nuclear spin precession due to the hyperfine interactions of extranuclear internal fields with the nuclear moments. The advantages of using radioactive isotopes rely on the fact that the excited states can be found with appropriate spin, μ - magnetic moments, and/or Q - quadrupole moment for a certain element, when their corresponding stable isotope has no appropriate states and NMR/NQR cannot be applied. An additional advantage of radioactive spectroscopy methods comes from the fact that generally an experiment requires a small amount of atoms $\sim 10^{11}$-10^{12}, which keeps impurity doping at very low levels, as required to study and simulate highly diluted systems. The variant of the PAC method considered in this work uses isotopes with a γ-γ decay cascade.

The coupling of the nuclear quadrupole and magnetic dipole moments with the local environment of the nuclei, due to the electric field gradient and magnetic hyperfine field, splits the nuclear energy magnetic sublevels. There are changes in the occupations of sublevels in the time of the interaction, and, consequently, the emission probability of a γ particle becomes

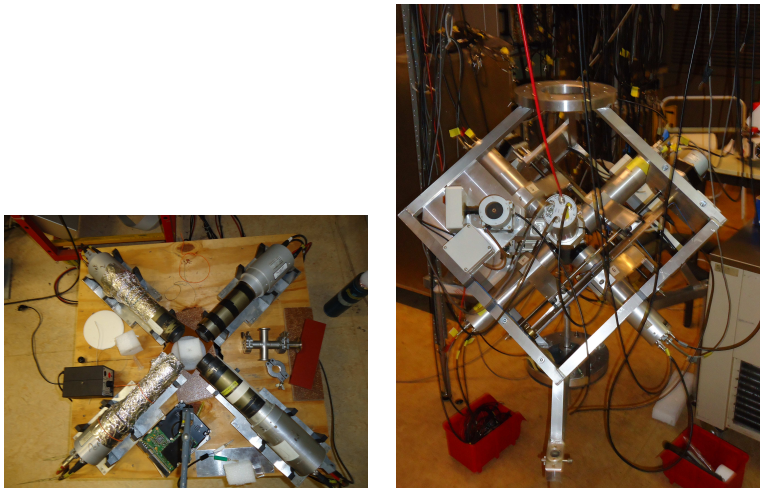

Figure 2.1: a) 4 detector PAC setup. b) 6 detector PAC setup.

time-dependent.

A PAC setup has an array composed of 6 or 4 detectors placed at relative angles of 90° and 180° [20]. A usual 4 detector setup is shown in figure 2.1(a), with the detectors at right angles to each other and the radioactive sample placed in the center. It is generally used for single crystalline samples. A 6 detector setup, shown in figure 2.1(b), can be more efficient. The experimental PAC observable function is built by combining spectra at 90° and 180°, and is generally expressed by

$$R(t) = 2\frac{N(180°,t) - N(90°,t)}{N(180°,t) + 2N(90°,t)}, \text{ where } N(\theta,t) = \sqrt[n]{\prod_{i=1}^{n} N_{0i}(\theta,t)}, \tag{2.1}$$

with $N_{0i}(\theta,t)$ being the experimental coincidence spectra taken at angle θ, as a function of time t, after subtraction of the chance coincidence background. This expression has several advantages: it corrects for severe systematic and geometric differences on efficiency of detectors ($\prod_{i=1}^{n}$), eliminates the exponential part of the intermediate state of the cascade, and it approximates to a simpler representation of the perturbation function $R(t) \sim A_{22}G_{22}(t)$; $G_{22}(t)$ contains all relevant information regarding the hyperfine interactions to study. Finally, 4-det./6-det. PAC setups have 4/6 det. at 180° and 8/24 at 90° combinations.

The start and stop photons are detected in accordance to their energies, in a selected energy window, and within a time window depending on the half-life of the intermediate state of the γ-γ cascade. After detecting the first photon, the nuclear spins precess in the intermediate state due to the extranuclear fields, the frequency of which is reflected in the second decay, in the time-dependence of the anisotropy of the radiation intensity, and the frequencies associated to these fields are detected by plotting the correlation function of the two decays $R(t)$. Therefore, during the lifetime of the second decay, the nuclei interact with their environment, and dynamic phenomena with times of the order of the ns half-life of typical probes may also be detected by

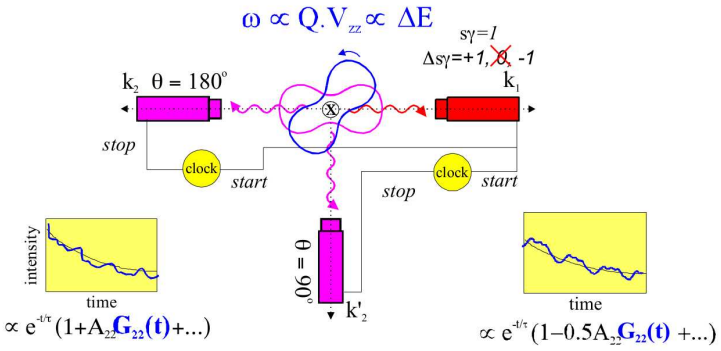

Figure 2.2: Schematic diagram of the PAC system and detection of the anisotropic radiation intensity by the detectors.

PAC.

Fig. 2.1 presents a schematic diagram of the measurement of two coincidence spectra.

The main advantage of this technique is that the hyperfine interactions are local and allow discrimination of different atomic environments of the probes in the lattice. Regarding other hyperfine interactions techniques such as Mössbauer effect spectroscopy, PAC has an efficiency that is temperature independent amid a large number of different isotopes, allowing to perform a variety of experiments with different probe elements.

The general formula for the perturbed angular correlation $W(k_1, k_2, t)$ for γ-emitted directions k_1, k_2, as a function of time t is

$$W(\mathbf{k}_1, \mathbf{k}_2, t) = \sum_{k_1,k_2,N_1,N_2} A_{k_1}(1)A_{k_2}(2)G^{N_1N_2}_{k_1k_2}(t)\frac{1}{\sqrt{(2k_1+1)(2k_2+1)}} \times Y^{N_1^\alpha}_{k_1}(\theta_1,\phi_1)Y^{N_2^\alpha}_{k_2}(\theta_2,\phi_2), \tag{2.2}$$

where $Y(\theta, \phi)$ are the spherical harmonics for inclination angle θ and azimuthal angle ϕ corresponding to the direction k, A are the anisotropy coefficients, $G(t)$ is the perturbation factor which contains the hyperfine interaction. k_i and N_i are restricted to $k_i = 0, 2, ...,\mathrm{Min}(2I, l_i + l'_i)$ and $|N_i| \leq k_i$. The perturbation factor is given by

$$G^{N_1N_2}_{k_1k_2}(t) = \sum_{M_a,M_b} (-)^{2I+M_a+M_b}\sqrt{(2k_1+1)(2k_2+1)}\times \tag{2.3}$$

$$\begin{pmatrix} I & I & k_1 \\ M'_a & -M_a & N_1 \end{pmatrix}\begin{pmatrix} I & I & k_2 \\ M'_b & -M_b & N_2 \end{pmatrix}\langle M_b|\Lambda_t|M_a\rangle\langle M'_b|\Lambda_t|M'_a\rangle^*, \tag{2.4}$$

where I is the nuclear angular momentum, M are the nuclear energy sublevels, and Λ is the time-evolution operator.

A complete and rigorous mathematical derivation of the theory behind PAC is lengthy and beyond the scope of this report. The interested reader may consult the references [21, 22], and references therein.

To get quantitative information from the PAC spectrum, a theoretical fit is performed by constructing a function $R_{fit}(t)$. This perturbation function is calculated by using a software which finds the eigenvalues and eigenstates of the electric, magnetic or combined interactions hamiltonian [23]. The function is constructed as

$$R_{fit}(t) = 2\frac{W'(180°,t) - W'(90°,t)}{W'(180°,t) + 2W'(90°,t)}. \tag{2.5}$$

In the case where more than one environment is present, the effective fit function is

$$\overline{W'(\theta,t)} = \sum_i f_i W'_i(\theta,t), \tag{2.6}$$

where f_i are the fractions of the different environments. Usually, even in the same environment the hyperfine interactions are not the same at all probes, but there is a distribution of hyperfine fields instead of a single value. This may be a consequence of intrinsic inhomogeneities and distributions of point defects inside a sample, and leads to the damping of the experimental PAC spectrum. The distribution of fields can be is simulated by a Gaussian or Lorentzian function in the fit function by a damping factor characterized by the δ (width) parameter. For the case of a Lorentzian distribution the attenuation function is

$$D(\delta,t) = e^{-\delta\omega_0 t}, \tag{2.7}$$

where ω_0 is the frequency of the fundamental interaction.

In the following chapters where PAC is used, small introductions to the technique are also presented.

2.1.1 Isotopes

The ^{111m}Cd/^{111}Cd and ^{111}In/^{111}Cd are two of the isotopes used in this thesis (section 3.3). Their decay schemes are shown in figure 2.3. The ^{111}probe and intermediate state of the cascades is the $5/2^+$, 245.4 keV, same state. The nuclear moments of the intermediate state are $\mu = -0.766(3)\ \mu_N$ and $Q = 0.77\ b$ (taken from [24]). Since the intermediate state is the same, the measured hyperfine interactions are equal if the local environment is the same, when using both probe isotopes. The properties of the other probe state, ^{77}Br$\rightarrow^{77}$Se, used in the MnAs system, are presented in the respective chapter.

2.1.2 Hyperfine Parameters

The interesting properties from the point of view of solid-state materials physics obtained from the PAC measurements are the Electric Field Gradient tensor (EFG) and the Magnetic Hyperfine Field (MHF). The EFG is measured from the hyperfine interaction between a charge distribution with non-spherical symmetry and the nuclear quadrupole moment Q. The measurement of the quadrupole interaction and the knowledge of the probe's quadrupolar moment

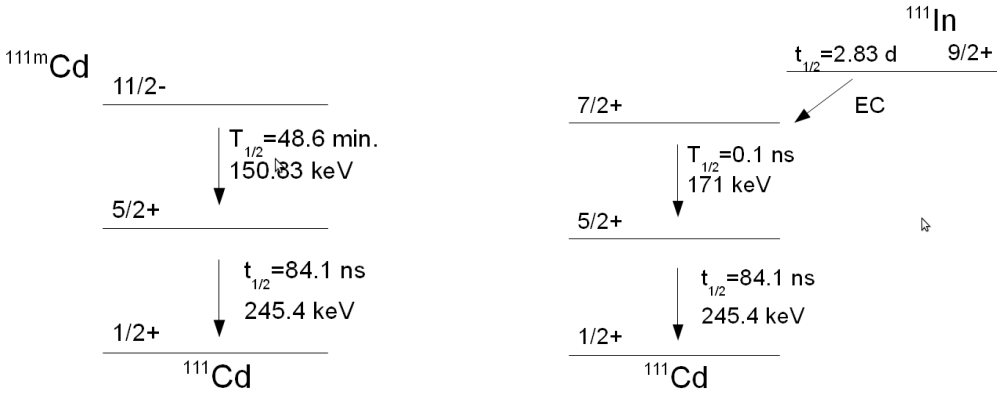

Figure 2.3: ^{111m}Cd (left) and ^{111}In (right) γ-γ decay cascades, showing half-lives and energies of the decays, and the nuclear spins of the involved states.

gives the EFG. The EFG is defined as the second rank tensor, symmetric and traceless, with components taken from the second spatial derivatives of the Coulomb potential at the nucleus site.

Since the EFG is traceless, only two components are needed to define it in its diagonal form. In the analysis of measurements the quantities usually considered are V_{zz} and $\eta = (V_{xx} - V_{yy})/V_{zz}$, called the axial asymmetry parameter. V_{xx}, V_{yy} and V_{zz} are defined according to the convention $|V_{zz}| \geq |V_{yy}| \geq |V_{xx}|$. The tensor in the laboratory frame may not be initially diagonal, but the hyperfine parameters only depend on its symmetry and coupling energy of the interactions, hence the observed frequencies are independent of the reference frame. In the study of single crystals, the charge distribution interacting with the probe nuclei is oriented with respect to the crystalline axis, which is revealed by the different amplitudes of the characteristic frequencies. However, the crystal directions of the EFG cannot be measured in polycrystals, which is the case in the studies presented here.

The observable frequency with PAC depends on the quadrupole nuclear moment and EFG in the following way:

$$\omega_\phi = \frac{2\pi}{4I(2I-1)}\nu_Q k, \text{ with } \nu_Q = \frac{eQV_{zz}}{h}, \text{ for } \eta = 0, \tag{2.8}$$

where I is the nuclear spin and $k = 6$ for half-integer spin. ν_Q is called the "reduced frequency" of the interaction and is independent of η and I.

The magnetic hyperfine field (MHF or B_{hf}), arising from the dipole-dipole interaction between the nuclear magnetic moment and the magnetic moment of the extranuclear electrons, can be expressed by

$$B_{hf} = \frac{\omega_L \hbar}{g\mu_N}, \tag{2.9}$$

where μ_N is the nuclear magneton, g the g-factor and ω_L the observable Larmor frequency.

Interpretation and construction of V_{zz} and B_{hf}

When calculated by the L/APW+lo method (WIEN2K code) the EFG for transition metal nuclei can be separated in different contributions, where usually the contributions from p and d states are the largest. V_{zz}^p and V_{zz}^d have been found to be proportional to the difference of orbital occupancies in both cases [25], with

$$V_{zz}^p \propto \langle \frac{1}{r^3} \rangle_p [\frac{1}{2}(p_x + p_y]) - p_z] \tag{2.10}$$

and

$$V_{zz}^d \propto \langle \frac{1}{r^3} \rangle_d [d_{xy} + d_{x^2-y^2} - \frac{1}{2}(d_{xz} + d_{yz}) - d_{z^2}]. \tag{2.11}$$

For interpretation of the physical origin behind B_{hf}, it is usual to decompose it in four terms:

$$B_{hf} = B_C + B_{orb} + B_{spin} + B_{latt}, \tag{2.12}$$

where B_C is the Fermi contact interaction of the electronic spin density at the nucleus with the nuclear magnetic moment, B_{orb} and B_{dip} are the contributions of the magnetic interaction due to the electronic orbital momentum and electronic spin momentum, respectively, and B_{latt} is a contribution from the other atomic orbitals in the lattice, usually negligible.

The Fermi contact hyperfine interaction B_C is given by

$$B_C = \frac{8\pi}{3}\mu_B m(0), \tag{2.13}$$

where $m(0)$ is the spin density at the nucleus,

$$m(0) = \int^{E_F} d\epsilon [n_+(0,\epsilon) - n_-(0,\epsilon)]. \tag{2.14}$$

In the analogous interaction rederived for the relativistic case [26] the spin density at the nuclear position is replaced by the average magnetization over a region within the Thomson radius, $r_T = \frac{Ze^2}{mc^2}$.

The orbital and dipole interactions are calculated as

$$B_{orb} = 2\mu_B \langle \Phi | \frac{S(r)}{r^3} \overrightarrow{l} | \Phi \rangle \tag{2.15}$$

and

$$B_{dip} = 2\mu_B \langle \Phi | \frac{S(r)}{r^3} [3(\overrightarrow{s}\,\overrightarrow{\hat{r}}\,)\,\overrightarrow{\hat{r}} - \overrightarrow{s}] | \Phi \rangle, \tag{2.16}$$

where Φ is the long range component of the relativistic wave function, $\overrightarrow{l}$ is the orbital moment of an electron localized in the atom in question, and $S(r)$ is the reciprocal of the relativistic mass enhancement of the electron mass, defined by:

$$S(r) = \left[1 + \frac{\epsilon - V(r)}{2mc^2}\right]^{-1} \tag{2.17}$$

2.2 Density Functional Theory Calculations

A brief description will be given of the basic theory behind the first-principles calculations, and the two different implementations used. Solving the Schrödinger equation traditionally involves finding the wave-function. Nowadays, the most common alternative way of solving the quantum-mechanical problem approximately in solids (and, more recently, molecules), is density functional theory (DFT), where the basic variable is the electronic density. The basis for this are the Hohenberg-Kohn theorems [2], where it is shown that the electronic density in a universal functional minimizes an expression for the total energy when the density corresponds to the ground-state electronic density, and that it corresponds uniquely to the ground-state wave function. The practical way to solve for the density is usually solving self-consistently the Kohn-Sham equations [3]:

$$(-\frac{\hbar^2}{2m}\nabla^2 + V_s(\mathbf{r}))\phi_i(\mathbf{r}) = \epsilon_i\phi_i(\mathbf{r}), \tag{2.18}$$

where V_S is the effective potential of a single-particle problem:

$$V_S = V_{ext.} + \int \frac{n(\mathbf{r}')}{\mathbf{r} - \mathbf{r}'}d\mathbf{r}' + V_{xc}(n(\mathbf{r})) \tag{2.19}$$

$V_{ext.}$ is the external potential including the nuclei (since the Born-Oppenheimer approximation is used) or any applied external fields. V_{xc} is called the exchange-correlation potential and includes all the many-body effects which cannot be exactly calculated in this method. Starting with an initial density, the potential V_S is constructed to find the orbitals ϕ_i, which are then used to find a new density using

$$n(\mathbf{r}) = \sum_i^N |\phi_i|^2. \tag{2.20}$$

Iterating this procedure self-consistently the density eventually converges, and even though it uses single-particle potentials, it would correspond exactly to the ground-state density of the many-body system, assuming a complete knowledge of all the functionals used in the equations. However, in practice, V_{xc}, the exchange-correlation potential is unknown and must be approximated. The most basic approximation is the Local Density Approximation (LDA), wherein at each point in space the exchange-correlation potential corresponds to the exchange-correlation potential of an electron gas with uniform density equal to the density at that point (the exchange-correlation of the homogeneous electron gas for various densities has been solved using the quantum Monte-Carlo method). This approximation is, surprisingly, very useful, but for materials where there are localized sudden variations of the density in space it is revealed insufficient. A small improvement to solve this problem consists of making the potential also a function of gradients of the density at that point, resulting in the so called generalized gradient approximation (GGA), the term "generalized" coming from certain rules to which the gradients

must obey. Both the approximations may be generalized to include spin. These schemes usually both fail in the accurate description of strongly correlated systems, but there are presently other functionals that improve the results in such cases such as LSDA+U or hybrid functionals. LSDA+U will be considered in this thesis on the rare-earth manganites.

There are now many codes available with different implementations to solve the Kohn-Sham equations. The main differences between these implementations are in the description of ϕ_i, and in the use (or not) of pseudopotentials. The two methods used in this thesis are the linear augmented plane wave + local orbitals method L/APW+lo (WIEN2K code [17]) and the projector augmented wave PAW, as implemented in the VASP code [16].

2.2.1 L/APW+lo method (WIEN2k) and PAW method (VASP)

The basic idea of wave function description in WIEN2K is in the older augmented plane wave (APW) method. In this method, the unit cell is divided in two kinds of regions: spheres centered at the atomic nuclear positions (so-called muffin tin spheres) and the remainder interstitial space. The basis functions for the Kohn-Sham orbitals are different in the two regions. In the interstitial space, plane waves are used ($e^{iG.r}$), where G is a vector in the reciprocal lattice). Inside the spheres, atomic-like functions are used, of the form $\sum_{lm} A^K_{lm} u_l(r', \epsilon) Y_{lm}(\hat{r}')$, where $Y_l m(\hat{r}')$ are spherical harmonics for orbital quantum number l and magnetic quantum number m, $u_l(r', \epsilon)$ is the solution of the radial Schrödinger equation in a spherical potential for an energy ϵ, where the A^K_{lm} coefficients are chosen to match the functions with the plane waves at the sphere boundary. The L/APW+lo method as implemented in WIEN2K further uses linearization energies and local orbitals to improve the accuracy and efficiency of the calculation (see *e.g.* [27] for details). This method is among the most accurate in DFT.

The other code used in the this work is VASP, with an implementation of the projector augmented-wave (PAW) method [28]. Similarly to the L/AWP+lo method, it also makes use of the full wave-functions (without the approximation of pseudopotentials), it is a so called *all electron* method.

The PAW method has similarities with both the L/APW+lo method (which is a special case), and to the pseudopotential method (which is a well defined approximation) [28].

Figure 2.5 compares the EFG tensor component V_{zz} obtained with the $BaTiO_3$ ferroelectric compound, calculated using WIEN2K and VASP codes. The calculations were done in the following way: considering the tetragonal ferroelectric structure measured, we use the scaling parameter Δ value which represents fractions of the atomic displacements, starting from the undistorted ideal perovskite ($\Delta = 0$), up to $\Delta = 1.2$, where $\Delta = 1$ corresponds to the experimental structure. The lattice parameters are fixed on the experimental tetragonal values ($a = b \neq c$ and $\alpha = \beta = \gamma = 90$). The unit cells for the structures corresponding to $\Delta = 0$ and $\Delta = 1$ are shown in figure 2.4. . The energy variation with both methods is also shown in figure 2.5. The energy differences between the polar and centrosymmetric phases are approximately the same in both methods. V_{zz} as a function of Δ is also shown in fig. 2.5, and we find a reasonable agreement between both methods of calculation, in a sensitive quantity such as V_{zz}.

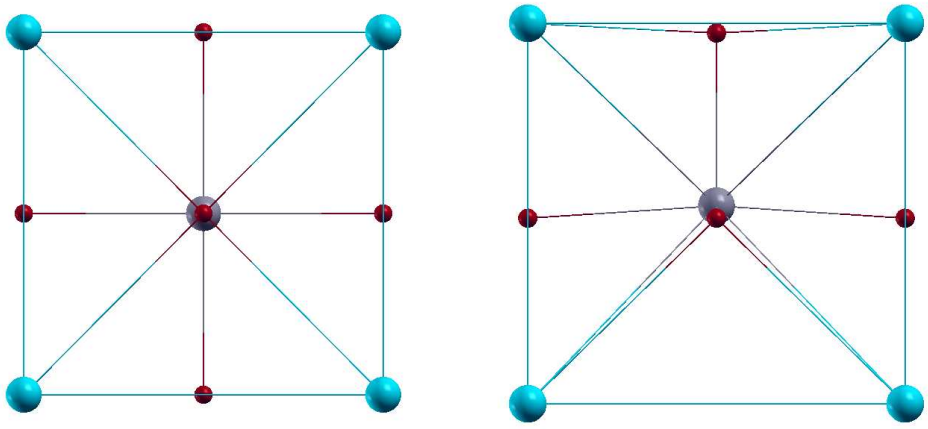

Figure 2.4: a) Tetragonal reference paraelectric structure, with atoms at ideal positions. b) Measured tetragonal ferroelectric structure, with small vertical displacements for the Ti (grey) and O (red) atoms.

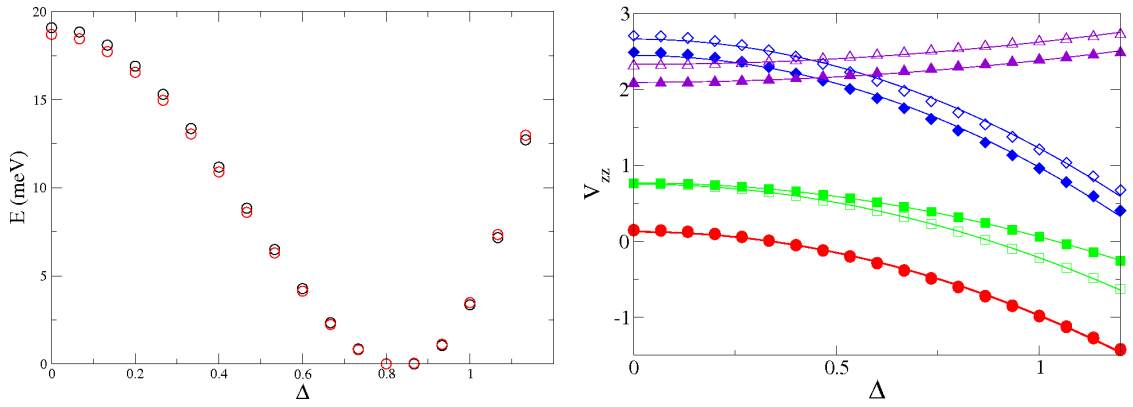

Figure 2.5: *Left*: Total energy as a function of ferroelectric distortion in $BaTiO_3$, as obtained with the L/APW+lo method (WIEN2K code) and PAW method (VASP code), with red and black circles, respectively. The zero of the energy scale was set as the energy minimum for both calculations. *Right*: V_{zz} as a function of ferroelectric distortion in $BaTiO_3$, as obtained with the L/APW+lo method (WIEN2K code) and PAW method (VASP code), corresponding to the closed and open symbols respectively. Different atoms are represented by the different colors and symbols: Ba = red circles; Ti = green squares; apical O = blue diamonds; equatorial O = violet triangles.

Chapter 3

Manganites

3.1 General Introduction

The first part of this chapter is dedicated to the perovskite manganites. This well studied but still intriguing class of materials, was discovered and characterized (structure and magnetism) by Jonker and van Santen in 1950 [29], for manganites with Ca/Sr/Ba and La. In the following early studies, a detailed magnetic characterization of $La_{1-x}Ba_xMnO_3$ was done using neutron diffraction by Wollan and Koehler [30]. The double-exchange model [31, 32] was used to understand their basic properties, where the metallic ferromagnetic state in the mixed-manganites is explained by the hopping of electrons between Mn^{3+} and Mn^{4+} sites. This hopping is favoured for parallel Mn spins, due to the Hund's coupling in the *d*-shells of Mn atoms and indirect exchange between Mn atoms through the O atoms. However, there are ferromagnetic and paramagnetic insulating states, charge and orbital ordered states, that are not explained within this simple model concept, and the model only explains qualitatively the other states.The doped $LaMnO_3$ system is the most investigated, due to the spin, electronic and lattice couplings, resulting in striking phenomena such as colossal-magnetoresistance, the change in resistance of several orders of magnitude observed in $LaMnO_3$ based (doped with Ca or Ba) thin films [33, 34]. In section 3.2, the calculation of the EFGs in the prototypical Ca manganite will be presented, with special emphasis in the consideration of Cd dilluted impurities in the supercell. This choice is due to the extensive use of the ^{111m}Cd/^{111}Cd probe in PAC studies. The experimental value was already determined, and therefore we concentrate in the theoretical study, and show that the DFT calculations with supercells can reproduce the experimental value in good agreement for relatively large Cd concentrations, or small number of atoms. Thus we establish the feasibility of this type of calculations for direct comparison with PAC, which will be used also for the other alkaline-earth manganites (section 3.3). An analysis of the electronic structure is also made.

Using the above results, section 3.3 is dedicated to the other two most studied alkaline earth end compounds, $BaMnO_3$ and $SrMnO_3$. This is also a reproduction of an article, to be submitted, where experimental studies were also conducted. The main part of the experimental results is dedicated to the EFGs obtained with PAC using ^{111m}Cd/^{111}Cd and ^{111}In/^{111}Cd probes. The structures are in this case more complicated, but the computational results are more useful for

the interpretation of the spectra. We can establish the nature the main environments detected in the spectra by comparing with theory.

Section 3.4 is dedicated to another structural form of manganites, stabilized when the manganese oxides are based in small rare-earth atoms. The rare-earths of higher atomic number and Y, Sc have smaller ionic radii, and the perovskite or perovskite-based structures previously studied are not found in usual conditions. Instead, an hexagonal polytype is formed. It is possible, however, to stabilize the corresponding perovskite distorted orthorhombic structures in these compounds, using high-temperature and high-pressure during synthesis. These types are also multiferroics, predicted [35], and subsequently observed [36], and are also of interest due to their magnetoelectric couplings. They are improper magnetic ferroelectrics, because the ferroelectricity is caused by the magnetic structure, and therefore T_C coincides with the establishment of the magnetic order. However, the focus here will be instead in the stable hexagonal forms, $P63/mmc$ high temperature paraelectric and $P63cm$ low temperature ferroelectric (and antiferromagnetic) structures found in small rare-earth manganites, particularly in the cases of $YMnO_3$, $HoMnO_3$, $ErMnO_3$ and $LuMnO_3$. Different order parameters influence the ferroelectricity in these compounds, in comparison to the orthorhombic variants, since they become ferroelectric at much higher temperatures than they order magnetically, in contrast to the strong coupling between magnetic and dielectric orders seen in the orthorhombic variants.Nevertheless, some magnetoelectric coupling has also been found. The main purpose here is the calculation of hyperfine parameters (EFGs and MHFs) in the pure compounds. These are very sensitive parameters, and the influence due to magnetism, structure and electronic correlations on these results is considered in different calculations, especially in the case of Y. A small final appendix presents a few calculations with Cd impurities, for the comparison with PAC experiments.

First principles calculations of hyperfine parameters on the Ca manganite with substitutional Cd-modeling of a PAC experiment

J.N. Gonçalves [a,*], H. Haas [b], A.M.L. Lopes [c], V.S. Amaral [a], J.G. Correia [b,d]

[a] Universidade de Aveiro, Departmento de Física and CICECO, 3810-193 Aveiro, Portugal
[b] CERN EP, CH 1211 Geneva 23, Switzerland
[c] Centro de Física Nuclear da Universidade de Lisboa, 1649-003 Lisboa, Portugal
[d] Instituto Tecnológico e Nuclear, E.N. 10, 2686-953 Sacavém, Portugal

ARTICLE INFO

Available online 30 June 2009

Keywords:
Manganite
DFT
EFG
TDPAC
Hyperfine

ABSTRACT

The APW + lo (augmented plane waves + local orbitals) method of density functional theory, as implemented in the Wien2k code, is applied to calculate the electric field gradient of manganites. We report the first principles calculations on $CaMnO_3$, and modeling of a perturbed angular correlation experiment with implanted ^{111m}Cd isotope. To model the experiment we additionally calculate in $Ca_{1-x}Cd_xMnO_3$, where we substitute Cd at the Ca site. Increasing Cd dilution is done with the use of supercells. We find that the experimental $CaMnO_3$ low-temperature value $V_{zz} \approx 6 \times 10^{-21}$ V/m^2 is reproduced, when optimizing internal parameters. The analysis of the EFG tensor at the Ca atoms, with different electric field gradients at inequivalent positions, reveals that the convergence of the calculations is obtained.

3.2 First principles calculations of hyperfine parameters on the Ca manganite with substitutional Cd - modeling of a PAC experiment

This section is the exact reproduction of a published article [4] (J. N. Gonçalves *et al.* Journal of Magnetism and Magnetic Materials. 2010;322(9-12):1170-1173. Proceedings of the Joint European Magnetic Symposia).

Abstract

The APW+lo (augmented plane waves + local orbitals) method of density functional theory, as implemented in the Wien2k code, is applied to calculate the electric field gradient of manganites. We report the first-principles calculations on $CaMnO_3$, and modeling of a perturbed angular correlation experiment with implanted ^{111m}Cd isotope. To model the experiment we additionally calculate in $Ca_{1-x}Cd_xMnO_3$, where we substitute Cd at the Ca site. Increasing Cd dilution is done with the use of supercells. We find that the experimental $CaMnO_3$ low-temperature value $Vzz \approx 6 \times 10^{-21} V/m^2$ is reproduced, when optimizing internal parameters. The analysis of the EFG tensor at the Ca atoms, with different electric field gradients at inequivalent positions, reveals that the convergence of the calculations is obtained.

3.2.1 Introduction

Manganese based oxides also known as manganites have been extensively researched because of both technological potential and theoretical interest, derived from the complex coupling of magnetic, electric, orbital and structural orders. Although these oxides appear to be quite difficult to describe in analytical frameworks, computational methods have given interesting insight in recent years. We report ab-initio density functional theory calculations (DFT) of the $CaMnO_3$ compound, and its Cd substitutional compounds of the form $Ca_{1-x}Cd_xMnO_3$. Density functional theory has been mostly used with $LaMnO_3$ and related compounds. In the case of the compound $CaMnO_3$, it was used to describe its structural and ground-state properties [37],

and electronic structure [38], for example.

The calculation of hyperfine parameters has been done with success e.g. in metals [39] and high-T_C superconductors [40], but, to our knowledge, there is not a detailed analysis of this property in manganites, using ab-initio methods. The electric field gradient (EFG) of the Ca manganite is analyzed here in detail, comparing the results with a Time-differential Perturbed angular correlation experiment (TDPAC).

The EFG is the symmetric traceless tensor with components taken from the second spatial derivatives of the Coulomb potential at the nuclear position. In the principal axis frame of reference of the EFG tensor, the components of interest are V_{zz} and the asymmetry parameter η, defined as $|V_{zz}| > |V_{yy}| > |V_{xx}|$ and $\eta = (V_{xx} - V_{yy})/V_{zz}$. It is measured from the hyperfine interaction between nuclear charges with non-spherical symmetry and the quadrupole nuclear moment Q. The measurement of the quadrupole interaction gives the EFG, when there is an accurate knowledge of the probe quadrupolar moment. It can be related the frequency of the interaction by $\nu_Q = eQV_{zz}/h$, when $\eta = 0$ (numerical methods are employed when $\eta \neq 0$ and the quadrupole interaction cannot be diagonalized exactly). The EFG is a sensitive quantity, depending mainly on the local (close to the nucleus) charge density. Thus the understanding of results obtained from this quantity provides local atomic scale information. In TDPAC spectroscopy, this property can be measured, provided a suitable isotope, in a wide range of temperatures. This study is relevant not only to the support and interpretation of experimental TDPAC data, which is needed, but also for the theoretical study of cadmium impurities in the Ca manganite. The EFG is obtained directly from the charge density, without arbitrary correction factors, as is the case for the point charge model.

3.2.2 Calculation Details

In this work we use the Wien2k code [17], that implements the augmented plane wave method with local orbitals (APW+lo) approach. This method divides the space into non overlapping spheres, described with spherical harmonics and the interstitial region, described with plane waves. It's an all electron method, thus suitable to calculate hyperfine parameters. The spheres radii used are 2.01, 1.82, 1.62 and 2.13 a.u., for Ca, Mn, O, and Cd respectively. The integration is done in the reciprocal space with the tetrahedron method. An adequate number of k-points that provides converging results is selected. The basis size allows plane-waves with $K_{max} = 4.22$ a.u.$^{-1}$ for one unit cell of 20 atoms, and K_{max}=3.70 a.u.$^{-1}$ with bigger cells. The calculations are all spin-polarized.

$CaMnO_3$ is a nearly cubic distorted perovskite, it forms an orthorhombic structure with the space group 62 ($Pnma$). Its structure is well known experimentally [41]. We also modeled a TDPAC experiment, by introducing a Cd impurity. The Cd is substitutional at the Ca site when implanted and annealed to perform TDPAC experiments [6]. The implanted quantities are very small (of the order ppm) thus requiring a dilution limit study. With the orthorhombic unit cell of pure $CaMnO_3$, which contains 4 formula units, we can substitute one Ca by a Cd atom and get the stoichiometry $(Ca_{0.75}Cd_{0.25})MnO_3$.To increase the dilution we construct supercells by a

periodic repetition of the $CaMnO_3$ unit cell and subsequent Cd substitution at one of the Ca atoms. We have used this approach to calculate increasingly diluted compounds until a low Cd concentration of $x = 0.06125$(x is the Cd concentration in the formula $Ca_{1-x}Cd_xMnO_3$), for a 80 atoms unit cell (2x1x2 of the previous orthorhombic cell).

We have kept the lattice parameters fixed to the low-temperature experimental values of the pure compound [41], but the correct description of the electric field gradient requires at least internal structural relaxation when calculating with impurities, even in highly diluted situations [42], so the internal atomic position parameters were optimized by minimizing calculated atomic forces. With a simpler point charge model it would not be possible to find the correct structure self-consistently.

The experimental TDPAC EFG values [6] for $CaMnO_3$, to be compared with our calculations, are $|V_{zz}| = 5.97\ 10^{21} Vm^{-2}$ (units used throughout this work for V_{zz}), $\eta = 0.60$ at $T = 10$K, $|V_{zz}| = 5.93$, $\eta = 0.64$ at $T = 80$K, and $|V_{zz}| = 5.82$, $\eta = 0.66$ at room temperature, $T \approx 290$K. Using these experimental values we extrapolate $0K$ values to be $V_{zz} = 5.976$ and $\eta = 0.593$. We will compare these extrapolated results with the theoretical results, also at $T = 0$K.

3.2.3 Results and Discussion

Electric Field Gradient

We start by calculating the value at Ca for pure $CaMnO_3$, and we get, using the experimental structure, $V_{zz} = -2.28 \times 10^{21}\ V/m^{-2}$ and $\eta = 0.81$. Optimizing the internal parameters we obtain $V_{zz} = -2.17$ and $\eta = 0.69$. However, there are no experimental hyperfine measurements that can confirm this.

For simplicity, and in order to study the effect of a different magnetic order, we start by neglecting the true experimental G-AF magnetic state of the low temperature compound, using instead Mn atoms with a ferromagnetic spin polarization. We have calculated with the Generalized Gradient Approximation(GGA), with the Perdew-Burke-Ernzerhof(PBE) parameterization of the exchange-correlation functional [43] and also with Wu-Cohen(WC) parametrization [44].

With the PBE-GGA, at both 25% and 12.5% of Cd, the V_{zz} at the Cd is -6.4 respectively, already close to -5.975 [6](value extrapolated from experiment). Since this doesn't correspond to the extremely low concentrations of ^{111m}Cd of ppm in the sample, the agreement with experiments suggests that at 25% of Cd the Cd atoms don't interact enough to change considerably the electronic density of the neighboring Cd. This is consistent with the fact that the chemistry of manganites is mainly due to the Mn-O interactions, while the Ca site is more ionic. This is also in agreement with the local character of the electric field gradient.

The EFG values obtained with WC-GGA are presented in figure 3.2. All the values correspond to structures with optimized internal parameters. At $x = 12.5\%$, using the experimental positions, V_{zz} is -7.35 and it goes to -6.2 only with relaxation, much closer to the experiment. The experimental value is the dashed line and corresponds to the TDPAC value obtained for the $CaMnO_3$ sample, -5.97×10^{-21}V/m^2 [6]. At the $x = 0.5$ concentration two structures were calculated, one in which there is inversion symmetry and another were there is no inversion sym-

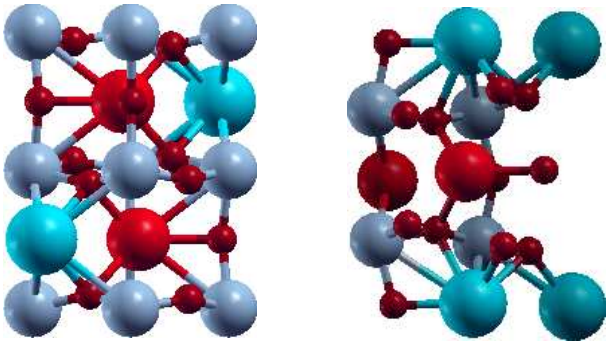

Figure 3.1: From left to right: Optimized structures for x=0.5, with inversion symmetry, and at right without inversion symmetry(color online).

metry (see figure 3.1). The distance between Cd atoms is smaller in the second case. We also used a 2x1x2 supercell to include 1 Cd atom for each 15 Ca atoms (6.125%). This value is even closer to the experimental value (fig. 3.2). Considering that the PAC method and quadrupole moment of ^{111}Cd both have an error associated, a closer value may not be meaningful of more accuracy anyway. In the results that follows, we continue to use the WC parametrization of the GGA.

The asymmetry value extrapolated from experiment, $\eta = 0.593$, is higher than the theoretical value at higher dilution. The theoretical values show an increase with higher dilution of Cd (fig. 3.2) and could approach the experimental value with higher dilution. The different values of the asymmetry vary much with different concentrations, when the V_{zz} are more or less the same, and are more sensitive to small structure variations.

We note that all of the previous calculations have disregarded the true G-AF experimental magnetic order, using ferromagnetic calculations. We repeated the calculation of the greater diluted cell with the G-AF arrangement to find if there were appreciable changes. The resulting EFG values at Cd were $V_{zz} = -6.00$, $\eta = 0.52$, closer to experiment but essentially unchanged. The EFG at Mn and O atoms also don't have high changes with F/A-AF magnetic orders.

There is another way to obtain the EFG, simpler and faster computationally, which is a point charge model. The EFG is calculated by taking the atoms as punctual ions, considering only its nominal charge. The different atoms are differentiated by a Sternheimer antishielding factor [45] γ_∞, which accounts for the inner shell polarization of the probe. The only difference when substituting calcium by cadmium will be in the Sternheimer antishielding factor. Still, it is useful to see to what extent it is accurate. With pure $CaMnO_3$, experimental structure [41] and the APW+lo method the results are $V_{zz} = -2.28$ and $\eta = 0.81$. With PCM, the same structure, the results are $V_{zz} = -2.11$ and $\eta = 0.90$, using the Sternheimer factor $\gamma_\infty = -13.95$ [46]. Although the PCM approximation gives acceptable results in this very simple case, it cannot calculate systems with impurities or relaxations. Even pure $LaMnO_3$ is already a different case due to the extra Mn valence electron that creates effects not accounted for by the PCM.

The average EFG of Ca atoms, for the different concentrations, should tend to the value

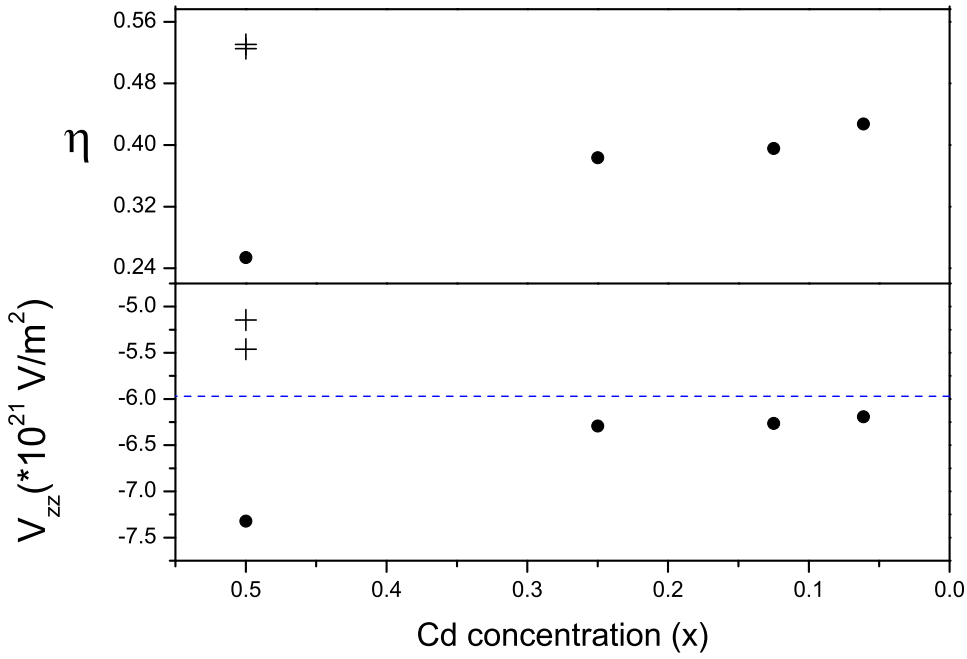

Figure 3.2: V_{zz}(bottom) and η(top) at the Cd sites using different Cd concentrations for the compounds $Ca_{1-x}Cd_xMnO_3$, with the Wu-Cohen GGA. The dashed line corresponds to the value of $CaMnO_3$ at the Cd probe at extrapolated from the TDPAC experiments. The results for the x=0.5 structure with no inversion symmetry are presented with crosses.

of V_{zz} of Ca at $CaMnO_3$ (-2.28 from our calculations) in the limit of lower Cd concentration. This is observed in the figure 3.3 (the cross represents the same structure as before). At a low dilution, with 25% of Cd, the average value is already very close. The individual atoms have different components of V_{zz} due to the different proximity to the Cd impurity, but in this case each Cd has already Ca atoms as nearest neighbors.

Electronic Structure

The densities of states calculated for the ferromagnetic calculations of $Ca_{1-x}Cd_xMnO_3$ with $x = 0$ and $x = 0.125$ are presented, for comparison, for the spin down (blue line) and up (red dashed line) states(fig. 3.4). The main differences are due to the sharp peaks of Cd states (also indicating that the Cd atoms don't interact much), at about $-7eV$, which are isolated in energy, and at the bottom of the valence band around $-6eV$. The Cd d states also hybridize with the valence band between -6 and 0 eV, and contribute to the peak at the bottom of the conduction band. In spite of these differences, the main features of the electronic densities of states with substitutional Cd remain the same.

3.2.4 Conclusion

In summary, we have calculated the hyperfine electric field gradient for the manganite $CaMnO_3$. We have introduced Cd, substitutional at the divalent cation site, in agreement

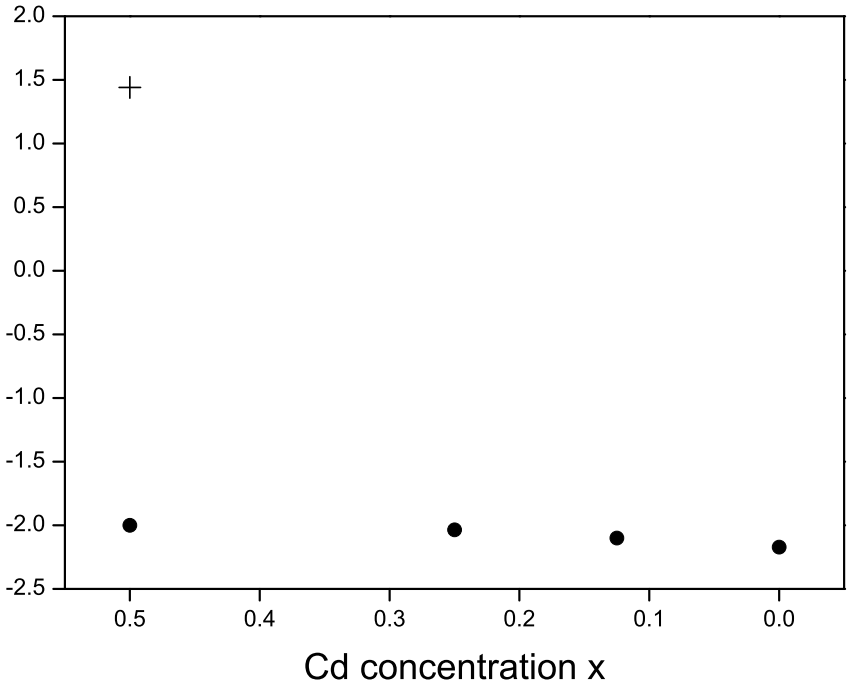

Figure 3.3: V_{zz}(in $Ca_{1-x}Cd_xMnO_3$) of the average Ca atoms electric field gradient tensor

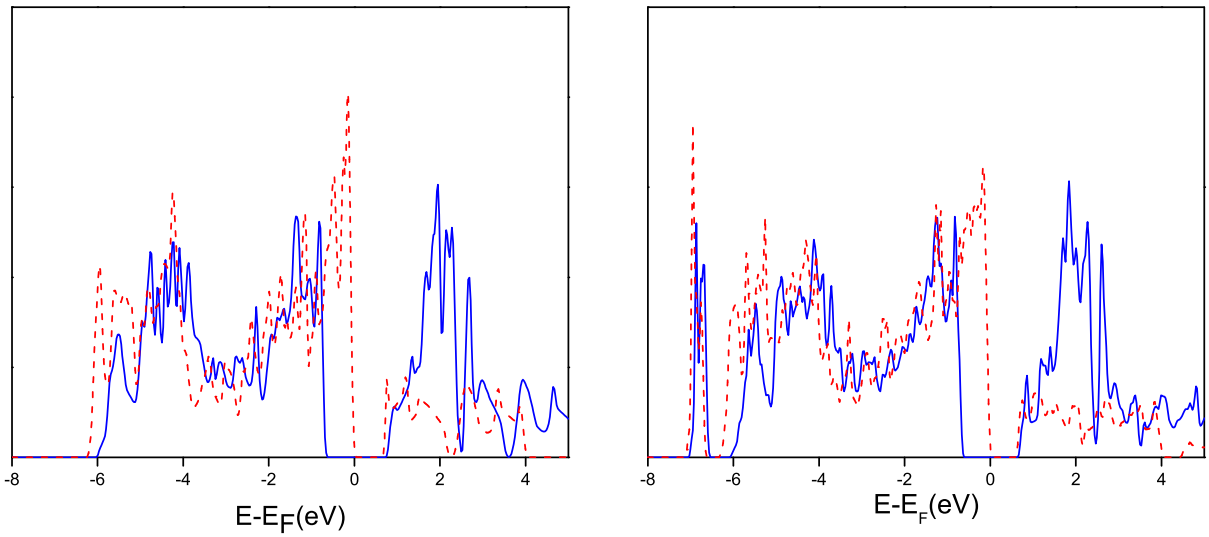

Figure 3.4: Density of states for the down(full line) and up(dashed line) spin states, for $CaMnO_3$(left) and $(Ca_{0.875}Cd_{0.125})MnO_3$(right). $E = 0$ corresponds to the Fermi energy.

with the PAC experiment. Since the EFG is a very sensitive quantity, its correct calculation is also a good test to the accuracy of the theoretical calculations. Considering the error associated with the experimental procedure to determine the hyperfine parameters in PAC, we find good agreement. Several results confirm the convergence of the calculations and the magnetic order does not change the EFG appreciably at the Ca site. Further work will involve calculations with other divalent manganites $SrMnO_3$, $BaMnO_3$, complementing TDPAC experimental studies.

Erratum

On page 18 it is stated: "numerical methods are employed when $\eta \neq 0$ and the quadrupole interaction cannot be diagonalized exactly". What is meant instead of "exactly" is analitically, and this only for high spins.

Hyperfine local probe study of alkaline-earth manganites $BaMnO3_3$ and $SrMnO_3$

J. N. Gonçalves,[1] V. S. Amaral,[1] J. G. Correia,[2] H. Haas,[2] A. M. L. Lopes,[3] J. P. Araújo,[4] and P. B. Tavares[5]

[1]*Departmento de Física and CICECO, Universidade de Aveiro, 3810-193 Aveiro, Portugal*
[2]*CERN EP, CH 1211 Geneva 23, Switzerland and Instituto Tecnológico e Nuclear, Estrada Nacional 10, PT-2686-953 Sacavém, Portugal*
[3]*Centro de Física Nuclear da Universidade de Lisboa, 1649-003 Lisboa, Portugal*
[4]*Departamento de Física and IFIMUP, Universidade do Porto, 4169-007 Porto, Portugal*
[5]*Departamento de Química and CQ-VR, Universidade de Trás-os-Montes e Alto Douro, 1013, 5001-801 Vila Real, Portugal*

We report perturbed angular correlations measurements with ^{111m}Cd/^{111}Cd and ^{111}In/^{111}Cd probes, at the ISOLDE-CERN facility, in the manganite compounds $BaMnO_3$, with the 6H and 15R polymorphs, and $SrMnO_3$, with the 4H polymorph. The electric field gradient is measured, and found approximately constant in a large temperature range. The electric field gradient (EFG) is also calculated from first-principles with the density functional (L)APW+lo method, and compared with the experimental results, by considering diluted substitutional Cd impurities. Based on the results we assign the sites for the ^{111}Cd and ^{111}In probes, as the Ba (for $BaMnO_3$-6H,15R) and Sr ($SrMnO_3$-4H) sites, apart from fractions of undetermined origin in the case of $BaMnO_3$-6H.

PACS numbers: 31.15.E-, 31.30.Gs, 75.47.Lx

3.3 Hyperfine local probe study of alkaline-earth manganites $BaMnO_3$ and $SrMnO_3$

Abstract

We report perturbed angular correlations measurements with ^{111m}Cd/^{111}Cd and ^{111}In/^{111}Cd probes, at the ISOLDE-CERN facility, in the manganite compounds $BaMnO_3$, with the 6H and 15R polymorphs, and $SrMnO_3$, with the 4H polymorph. The electric field gradient (EFG) is measured, and found approximately constant in a large temperature range. The EFG is also calculated from first-principles with the density functional (L)APW+lo method, and compared with the experimental results, by considering diluted substitutional Cd impurities. Based on the results we assign the sites for the ^{111}Cd and ^{111}In probes, as the Ba (for $BaMnO_3$-6H,15R) and Sr ($SrMnO_3$-4H) sites, apart from fractions of undetermined origin in the case of $BaMnO_3$-6H.

3.3.1 Introduction

Manganites have been the subject of renewed interest in the last years, due to the coupling of various order parameters, resulting in effects such as colossal magnetoresistance and multiferroicity.

The divalent alkaline-earth based manganites, of the form $AMnO_3$ (where A is Ca, Sr or Ba) are electronically the simpler cases, since the metal ions can be formally considered as Mn^{4+}, without the Jahn-Teller distortion resulting from partially filled d orbitals. The observed structure in these compounds is related to the ion sizes, since the relation between interatomic distances and structure can be understood by the tolerance factor $t = d_{A\_O}/(\sqrt{2}d_{Mn\_O})$ [47], where d_{A_O} and d_{Mn_O} are the interatomic distances: $t = 1$ corresponds to the ideal perovskite structure; values greater than one are found in hexagonal manganites, where the number of MnO_6 octahedra which share faces instead of vertices (as in the ideal perovskite) is increased; values of t smaller than one are concomitant with an orthorhombic structure. In its ground

state at low temperature, $CaMnO_3$ is orthorhombic, due to the smaller radius (and tolerance factor) of Ca^{2+}, while $BaMnO_3$ and $SrMnO_3$ are hexagonal. In spite of this apparent simplicity, the synthesis of the Sr or Ba systems (Ba in particular) is quite complex. An accurate control of the thermodynamic conditions, temperature and oxygen partial pressure, in the preparation and in the cooling steps (slow cool or quenching) is very important to obtain a given phase. The Ba manganite, for example, can be synthesized in the non-stoichiometric form $BaMnO_{3-x}$ with different values of x (e.g. Adkin and Hayward [48]).

Different polymorphs of hexagonal structures can be formed, corresponding to different one-dimensional strings of face-sharing octahedra, for example: hexagonal two-layer (hex 2L) (ABAB), where strings of face-sharing Mn-O octahedra have infinite length, or hexagonal 6H (ABCACB), hexagonal 4H (ABAC), and rhombohedral 15R, where these strings are periodically broken (see figure 3.5).

There are several experimental measurements of structural and magnetic properties carried on various forms of $BaMnO_3$ [49, 50, 51, 52, 53] and $SrMnO_3$ [50, 54]. The computational methods that enable first-principles calculations have also given a good understanding of these compounds. Density functional theory (DFT) calculations have been performed for the study of these systems, with detailed analysis of the density of states, band gaps, band structures and chemical bonding in the Ca/Ba/Sr manganites [37], of the magnetic and structural properties [55] and heat capacity and lattice dynamics [37] of cubic and hexagonal $SrMnO_3$. Hartree-Fock calculations have also been used for the study of magnetic and electronic properties in $CaMnO_3$ [56]. These works showed the good reliability of the calculations. Recently, DFT studies have predicted ferroelectric instabilities in specific strain conditions for $CaMnO_3$ [57], $SrMnO_3$ [58] and $BaMnO_3$ [59], giving these materials the possibility of being multiferroics. More recently, it was found that the perovskite mixed manganite $Sr_{1-x}Ba_xMnO_3$ is ferroelectric, with large polarization and magnetoelectric effects [60].

In this work, we will use a combined theoretical (DFT calculations) and experimental hyperfine studies (perturbed angular correlation spectroscopy, PAC) approach to study two polymorphs of $BaMnO_3$, and the $SrMnO_3$ compounds. Monophasic samples were synthesized: $BaMnO_3$ in the 6H phase and 15R phases, and $SrMnO_3$ in the 4H phase.

We will direct our first-principles calculations to the electric field gradient (EFG), which is compared directly to the experimental PAC data. A local hyperfine property has several advantages, e.g., it can be related to chemical bonding and structure and can distinguish between different local environments of atoms, such as different lattice sites, and local defects in the probe's neighborhood. Furthermore, these measurements and calculations may be of relevance to an analysis of the possible ferroelectricity in relation to the EFG, as done e.g. in the mixed $Pr_{1-x}Ca_xMnO_3$ manganite [6]. Since the EFG depends sensitively on the electronic density its calculation will also be a good test of the theory in these systems.

The diagonalized EFG tensor is usually characterized by its component of largest magnitude V_{zz} and the asymmetry parameter $\eta = \frac{V_{xx}-V_{yy}}{V_{zz}}$.

In a previous work, we have presented first-principles calculations, on the $CaMnO_3$ system, with the goal of understanding PAC results with a ^{111m}Cd-^{111}Cd probe. This probe has the

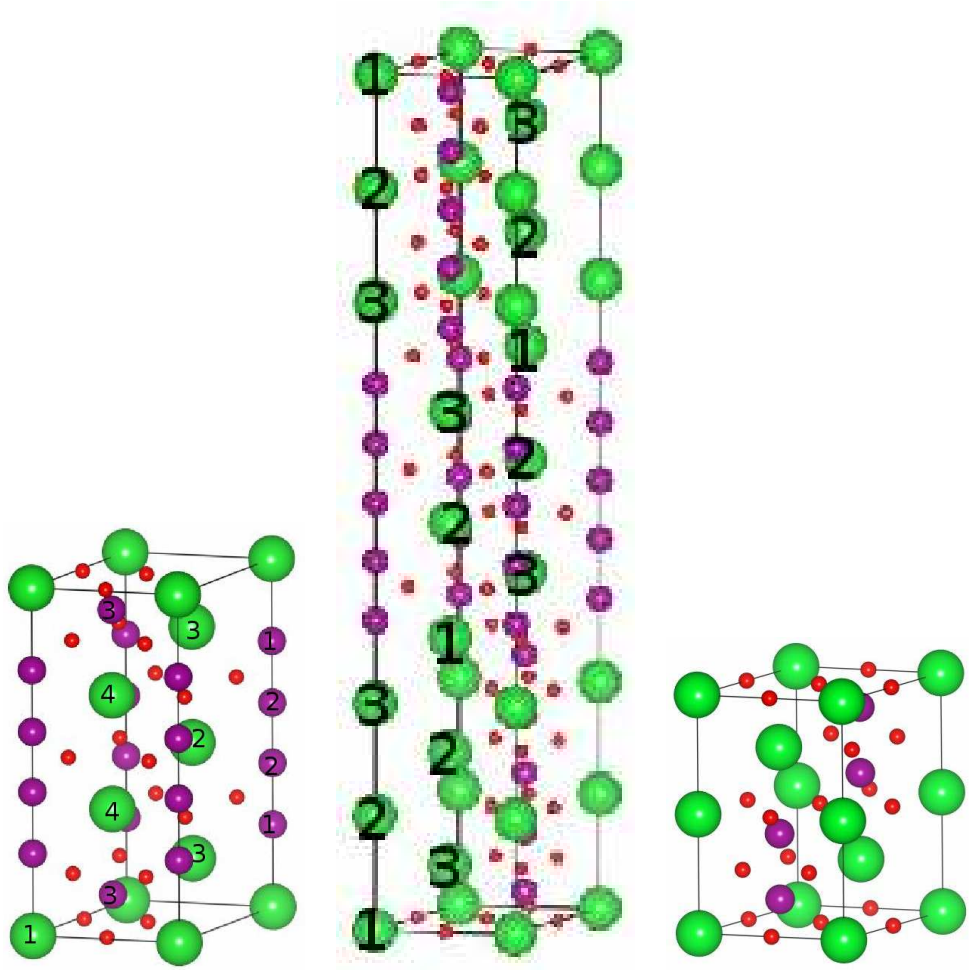

Figure 3.5: Structural representation of the unit cells of $BaMnO_3$-6H (left), $BaMnO_3$-15R (center) and $SrMnO_3$-4H (right). The larger spheres are Ba/Sr atoms, medium spheres are Mn atoms and small spheres are O atoms. The Ba/Mn atoms and Ba atoms in the $BaMnO_3$-6H and -15R structures are marked by the number which will be given in the following results.

particular advantage of keeping the element unchanged during the measurement. We considered the incorporation of a Cd impurity in the manganite matrix, to calculate the properties at the probe location [4]. Here we use the same approach for the first-principles calculations, and expand the perturbed angular correlation study on the other alkaline-earth manganites of Ba and Sr, with the same ^{111m}Cd-^{111}Cd probe and also with the ^{111}In-^{111}Cd probe in one case.

In the next sections we present results of calculations for $SrMnO_3$ and for different polymorphs of $BaMnO_3$, and discuss the results. Direct comparison with the experiments is done by performing the calculations with diluted Cd supercells, for the cases of 4H-$SrMnO_3$ and 6H-$BaMnO_3$. The experimental results are presented in the following section in the same order, with its interpretation in relation to calculations.

3.3.2 First principles calculations

We use the mixed LAPW/APW+lo method, as implemented in the Wien2k package [17]. In this method the space is divided in spheres and the interstitial space. The wave functions inside the spheres are expandend in atomic like functions, with spherical harmonics where $l_{max} = 10$ was used. In the interstitial region the wave functions are expanded in plane waves up to a maximum wave number, and a maximum wave vector $G_{max} = 12$ a.u.$^{-1}$ was used for the expansion of the charge density. Different number of k-points and maximum wave number for the planewaves were tested in the simple cases to obtain a good convergence of total energy and EFG. When calculating larger supercells or different structures the number of k-points was changed accordingly. The GGA functional from Wu and Cohen [44] is used for all the calculations except if noted otherwise. Core states are treated fully-relativistically while valence states are treated in the scalar-relativistic approximation.

$SrMnO_3$

$SrMnO_3$ with the 4H structure has the space group number 194, $P6_3/mmc$. The fractional coordinates and Wyckoff positions of the atoms in this structure are the following: Sr1: 2a; Sr2: 2c; Mn: 4f (1/3,2/3,z_{Mn}); O1: 6g; O2: 6h (-x_O,-2x_O,1/4). With the experimental data of P. D. Battle et al. [54], $z_{Mn} = 0.6122(5)$ and $x_O = 0.1807(2)$, and the lattice parameters are $a = 5.4434(2)$ Å, $c = 9.0704(1)$ Å. We used this structure as a starting point for our calculations. After relaxing the free atomic coordinates to calculated atomic forces less than 4 mRy/au, the atomic coordinates are $z_{Mn} = 0.61341$ and $x_O = 0.18058$. This corresponds to small variations of 0.12% and 0.01% for z_{Mn} and x_O. The small variation of x_O is within the experimental error. The lattice parameters were not optimized, since usually the influence of these parameters in the EFG is small, and they are not so reliable as the experimental ones. In this case we found that a mesh of $6 \times 6 \times 3$ k-points and $R_{mt}K_{max} = 6.5$ is enough for converged results. The EFG values are similar in both experimental and theoretically relaxed structures, when assuming ferromagnetic (F) arrangement of Mn atoms, as should be expected if the calculations are accurate (table 3.1).

We also considered the magnetic state where Mn atoms have the same spin polarization within the same plane of constant z, but neighbor Mn planes in the z direction have opposite spin polarization. This antiferromagnetism, called A-AF [30], is the stable magnetic order at low temperatures. For this case the deviation of the theoretically optimized structure in relation to the initial experimental structure is even smaller, as expected. With the exp. structure, this order is stable in relation to the ferromagnetic state by 1.4 eV according to our calculations. The structural coordinates are not moved more than 0.09% relative to the experimental value in the case of z_{Mn}. Both parameters are equal to the experimental ones within the experimental error. This translates itself in almost exactly equal hyperfine parameters for the theoretical and experimental structures, even more so than in the F case. Nevertheless, the agreement is already good for the F state, in the following calculations when we introduce Cd impurities, calculations are again ferromagnetic, for simplicity, and furthermore, because in the temperature range where

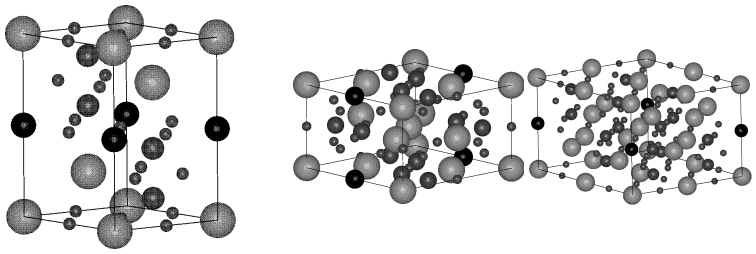

Figure 3.6: Supercells with Cd substitutional at the Sr 1 site. Cd atoms are represented by black spheres. Cd concentrations of 25%, 12.5% and 6.25%.

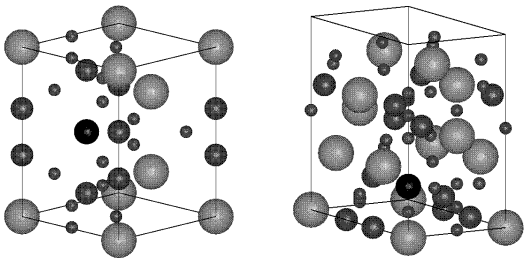

Figure 3.7: Supercells with Cd substitutional at the Sr 2 site. Cd atoms are represented by black spheres. Cd concentrations of 25% and 12.5%.

we will measure and compare with theory $SrMnO_3$ should be paramagnetic [54]. We show that the influence of the different magnetic states in the EFG is small, for all atoms, in table 3.1.

Table 3.1: Calculated $V_{zz}(10^{21}V/m^2)$ of 4H-$SrMnO_3$, with the F and A-AF magnetic configurations, experimental and relaxed structures. The asymmetry η is zero except for the oxygen atoms, where it is also shown (second number).

Atom	(F, exp.)	(F, rel.)	(A-AF,exp.)	(A-AF,rel.)
Sr 1	3.94	4.11	4.01	4.09
Sr 2	1.63	1.39	1.90	1.79
Mn	-0.29	-0.40	-0.45	-0.48
O 1	7.66; 0.07	7.73; 0.06	7.56; 0.21	7.61; 0.21
O 2	-8.17; 0.01	-8.10; 0.02	-7.89; 0.10	-7.84; 0.09
Mn 2 (A-AF)			-0.45	-0.47

In order to reproduce the experimental situations of a highly diluted Cd probe (approx. smaller than 10 ppm), we start by assuming that the Cd occupies the Sr sites substitutionally. This substitution of Cd at the alkaline earth site has been shown to be the case for the Ca manganite, and is usually found experimentally in other manganites [6, 4]. It is also a good assumption based on the ionic picture $Sr^{2+}Mn^{4+}O_3^{2-}$ and considering that Cd has ionic charge 2+. Two cases are possible: Cd occupies the Sr1 site, or the Sr2 site (as defined above). These two situations are considered in independent calculations, and since dilutions of the *ppm* order are not feasible for calculations, we use a series of increasingly larger supercells to calculate different impurity concentrations so that the EFG converges to the high dilution case when Cd concentration is lowered. As mentioned before, for this case we use only the F magnetic arrangement. See figures 3.6 and 3.7 for representations of some supercells. With

one atom of Cd substituting one of the sites in a single unit cell, $Sr_{0.75}Cd_{0.25}MnO_3$ is obtained (25% of Sr sites are substituted). If we double the dimensions in the x direction (2x1x1), we get $Sr_{0.875}Cd_{0.125}MnO_3$, while doubling both x and y directions gives a $Sr_{0.9375}Cd_{0.0625}MnO_3$ composition (6.25%). Finally, for the case of substitution at the Sr 1 site, we also doubled the previous supercell in the z direction, getting a 2x2x2 supercell with 3.125% concentration. The use of high Cd concentrations when compared with experiment is justified by the locality of the EFG, also seen with the convergence of the results.

Table 3.2 shows the calculations for Cd at the Sr1 site, and the values of V_{zz} appear to be approximately converged, around $6 \times 10^{21} V/m^2$ for concentrations of 12.5% and lower. The calculation with higher Cd dilution, with 3% (1/32) of Cd atoms substituted at Sr sites, gives $V_{zz} = 6.22\ 10^{21} V/m^2$. The asymmetry parameter η is zero due to the hexagonal symmetry, except for the 2x1x1 supercell (where $a \neq b$) constructed for $Sr_{0.875}Cd_{0.125}MnO_3$, where $\eta = 0.34$. Table 3.3 contains the same type of calculations for the case where Cd is substitutional at the Sr2 site. In this situation V_{zz} is fairly converged at a value of the order of $1.5 \times 10^{21} V/m^2$ when considering the 2x1x1 supercell ($x = 0.125$).

Comparing the V_{zz} values obtained with Cd and the V_{zz} at the corresponding Sr atom in the pure compound we find that the value remains of the same order at the Sr2 site, but at the Sr1 site the value of V_{zz} with Cd is considerably higher.

We can obtain a crude estimation of the relation between the V_{zz}(Cd) and the V_{zz}(Sr) values in the pure case, by using the Sternheimer factors of a simple point charge model. The relation is: $V_{zz}^{Sr} = V_{zz}^{Cd}(1-\gamma_\infty^{Cd})/(1-\gamma_\infty^{Sr})$, where γ_∞ are the Sternheimer factors, to account for the inner electronic shell polarization of the atoms. Structural relaxations due to Cd substitutions are not considered. Using values found in the literature for γ_∞ we get $V_{zz}^{Sr} = V_{zz}^{Cd} \times a$, with $0.62 < a = (1 - \gamma_\infty^{Cd})/(1 - \gamma_\infty^{Sr}) < 0.93$ (using three different values for γ_∞^{Cd} and two for γ_∞^{Sr}, obtained by different methods [46, 61, 62]). This relation holds when comparing the values obtained by our first principles calculations at Sr and Cd [$V_{zz}(Sr)/V_{zz}(Cd) = 4.09/6.22 = 0.66$ for the Sr1 site, and $1.39/1.48 = 0.94$ for the Sr2 site], suggesting: a) that the structural relaxations are small; b) that the Cd bonds are mainly ionic in nature. Indeed, the first suggestion is confirmed if we compare our relaxed structure obtained with $SrMnO_3$, and the same structure (atomic positions fixed) with $Sr_{0.96875}Cd_{0.03125}MnO_3$, Cd substitutional at Sr2. The calculated atomic forces are very low with just a maximum relatively small force of 10 mRy/au in one of the atoms.

The nearest neighbors for Sr1 in $SrMnO_3$(F,rel.) are six O atoms at a distance of 2.72 Å, six O atoms at 2.84 Å, and six Mn atoms at 3.81 Å. For the relaxed structure with Cd substitutional at that site ($x = 3.125\%$), the Cd local environment has six O atoms at 2.64 Å, six O atoms at 2.85 Å, and six Mn atoms at 3.29 Å. These distances have a difference relative to the pure case of 3%, 0.35% and 13.65% respectively. For Sr2 in $SrMnO_3$ (F,rel.), the local environment is composed of six O atoms at 2.725 Å, six atoms at 2.759 Å, while the same site with Cd has six O atoms at 2.701 Å, and other six at 2.750 Å, corresponding to relative differences of 0.88 % and 0.33% ($x_=$3.125%). These changes are very small in general, considering that a different atom goes to the lattice.The changes are smaller for the positions of atoms in the local vicinity of the Cd atom at the Sr2 site, suggesting it is more favourable for Cd to be in this site. Indeed,

according to the calculations, between both supercells with 12.5 % Cd (at Sr 1 or Sr 2 sites), the one with Cd at the Sr2 site is energetically more stable, by 0.2 eV.

Table 3.2: Calculated electric field gradient of 4H-$SrMnO_3$, for a Cd atom substitutional at the Sr1 site, for various Cd concentrations x, in the formula $Sr_{1-x}Cd_xMnO_3$.

x	$V_{zz}(10^{21}V/m^2)$
0.25	3.85
0.125	6.08
0.0625	6.47
0.03125	6.22

Table 3.3: Calculated electric field gradient of 4H-$SrMnO_3$, for a Cd atom substitutional at the Sr2 site, for various Cd concentrations x, in the formula $Sr_{1-x}Cd_xMnO_3$.

x	$V_{zz}(10^{21}V/m^2)$
0.25	0.36
0.125	1.38
0.03125	1.48

$BaMnO_3$

For the 6H-$BaMnO_3$ compound, 5 k-points in the irreducible Brillouin zone and a maximum wave number with $R_{mt}K_{max}$=7 were used ($R_{mt}K_{max}$=6 gives already converged results, and was used in some calculations with Cd impurities). The starting point for the 6H structure was taken from the work of Adkin et al. [48]. With this structure the calculated atomic forces are generally low (one force at 32 and the rest less than 13 mRy/au). The symmetrically unconstrained atomic parameters were permitted to vary and a theoretically more stable relaxed structure was obtained, when the atomic forces were lower than 2 mRy/au. The atomic coordinates obtained have at most a 0.88% difference with respect to the initial experimental ones.

Ferromagnetism was assumed, which is not a known state of $BaMnO_3$, but this should be reasonable judging by the the similar system $SrMnO_3$-4H (shown previously) where the EFG has very small changes with a different magnetic state.

Results of the EFG for the structure of Adkin et al. and after relaxation of internal parameters are summarized in table 3.4. In order to see if the use of another exchange-correlation potential has any influence in the calculated EFG, we show also the results with the GGA-PBE functional [43]. There are almost no changes in the results with the GGA-PBE, typically of the order or less than $0.1 \times 10^{21}V/\mathrm{m}^2$. The asymmetry parameter is also shown for the sites where symmetry allows it to be different from zero, and it is usually very small. Results for the EFG of the 15R phase and the hexagonal polymorphs 2H (which is the stable phase at low temperatures) and 4H are shown in tables 3.5 and 3.6. The 2H structure is taken from [49] and the 4H structure is taken from our own X-ray diffraction measurements. The 15R experimental structure is from Adkin et al. [48]. The atomic coordinates were also optimized, and remain

qualitatively equal to the experimental structure calculations. The variations in the structure are also small.

These calculations show that the EFG has variations depending on the polymorph particularly in the different atoms of Ba, due to the different packings of Mn-O octahedra. Mn atoms have V_{zz} between -2.6 and 0.2 $\times 10^{21} V/m^2$ for all polymorphs, and O atoms have EFGs approximately between -9 and $9.5 \times 10^{21} V/m^2$, and in absolute value can be located in the range 5.9-9.45. On the other hand Ba has usually one high value between 10 and 13, and for other Ba atoms the EFG can be quite low, depending on the structure.

Table 3.4: Calculated EFG of $BaMnO_3$, in the hexagonal 6H polymorph. The two sets of values obtained with the GGA-PBE (first) and GGA-WC (second) exchange-correlation potentials(V_{zz} in $10^{21}\ Vm^{-2}$).

Atom —	V_{zz} (exp) —	η (exp.) —	V_{zz} (rel) —	η (rel)
Ba 1 —	-0.36; -0.42		0.25; -0.16	
Ba 2—	12.25; 12.46		13.05; 13.62	
Ba 3—	9.65; 9.82		8.62; 9.30	
Ba 4—	5.16 ; 5.22		4.82; 4.97	
Mn 1—	-0.0002;0.04		0.20; 0.23	
Mn 2—	-1.85; -1.78		-1.75; -1.72	
Mn 3—	-0.24; -0.19		-0.26; -0.22	
O 1—	-8.81; -8.87	0.02; 0.02	-8.75; -8.82	0.03; 0.00
O 2—	-5.90; -5.95	0.06; 0.06	-6.08; -6.03	0.01; 0.03
O 3—	8.29; 8.31	0.002; 0.001	8.36; 8.27	0.01; 0.01
O 4—	-7.54; -7.59	0.39; 0.39	-7.61; -7.60	0.35; 0.37

Table 3.5: Calculated EFG of $BaMnO_3$, in the rhombohedral 15R polymorph with GGA-PBE functional, relaxed structure with forces less than 6 mRy/au.

Atom	$V_{zz}(10^{21} V/m^2)$	η
Ba 1	6.76	
Ba 2	11.46	
Ba 3	4.69	
Mn 1	-1.79	
Mn 2	0.15	
Mn 3	-1.83	
O 1	-8.31	0.07
O 2	-7.73	0.35
O 3	-62.2	0.07

We note the following general rule for the V_{zz} of Ba atoms in the different structures. In the 2H form, there is only one type of Ba atom, with the high V_{zz} value reported (table 3.6). The 2H structure consists of infinite chains of face sharing octahedra along the z direction. In other polymorphs, we see that the higher value of V_{zz} at Ba sites is of the same order, and looking at the location of this site in the various structures, and its relation to the Mn-O octahedra, we see that this V_{zz} always corresponds to the Ba atoms with z coordinates in middle of the chains of face sharing octahedra. This can be explained by the fact that the local environment is similar

Table 3.6: Calculated V_{zz} of $BaMnO_3$, in the 4H (left), and 2H (right) (structure from) experimental, and relaxed structures. ($10^{21}V/m^2$).

Atom —	V_{zz} —	η —	V_{zz} —	η
Ba	9.99; 11.93		10.33; 10.22	
Ba	1.64; -0.38			
Mn	0.10; -0.29		-1.92; -1.90	
O	8.58; 8.56	0.07; 0.06	-6.52; -6.58	0.04; 0.06
O	-9.45; -9.10	0.08; 0.05		

at that site to the one of the Ba atom in the 2H structure, whereas the other atoms are closer to corner sharing octahedra separating the different Mn-O octahedra chains.

In order to compare with the PAC experiments with Cd probes, we introduce Cd impurities substitutional at the Ba site. We consider the case of the BMO-6H structure, and note that the structure is already quite complicated without Cd, making large supercells very time consuming. However, already with the unit cell we can substitute one atom of Ba by Cd to get the concentration $x = 1/6$. We calculated with a larger $2 \times 2 \times 1$ supercell (Cd concentration $x = 1/24$ subs. at the Ba1 site), and the V_{zz} were found to change little, not only in Cd but in all atoms. Figure 3.8 shows a comparison of the V_{zz} obtained with the two BMO-6H cells. There are groups of atoms with approximately equal V_{zz} in the supercell, which usually correspond to only one atom in the unit cell with that same V_{zz}. In the supercell the internal structure was not completely optimized, which probably accounts for the difference observed at Cd with relation to the unit cell. Having considered this fact we calculated the other Cd substitutions also for the high concentration $x = 1/6$, in order to reduce computational time, expecting this to be a good approximation to the low impurity concentration limit. We present the V_{zz} obtained at the Cd site substituted in each of the inequivalent Ba sites in the table 3.7. The asymmetry is zero at the Cd sites for all cases due to symmetry.

It is interesting to remark that the comparison of the EFG at Cd with the EFG at the respective Ba sites in the pure compound shows no proportionality, meaning that the Cd probes provoke different changes in the local charge density with the different local environments.

Table 3.7: Calculated EFG of $Ba_{5/6}Cd_{1/6}MnO_3$, in the 6H polymorph, at the Cd site, for independent calculations with Cd substituted at each of the inequivalent 6H sites.

Site with Cd	$V_{zz}(10^{21}V/m^2)$ at Cd
Ba1	-1.59
Ba2	4.83
Ba3	1.61
Ba4	2.37

3.3.3 Experimental results

Monophasic samples of $BaMnO_3$ with the 6H structure, other monophasic samples with the 15R structure, and others of $SrMnO_3$ with the 4H structure were prepared by the urea sol-gel

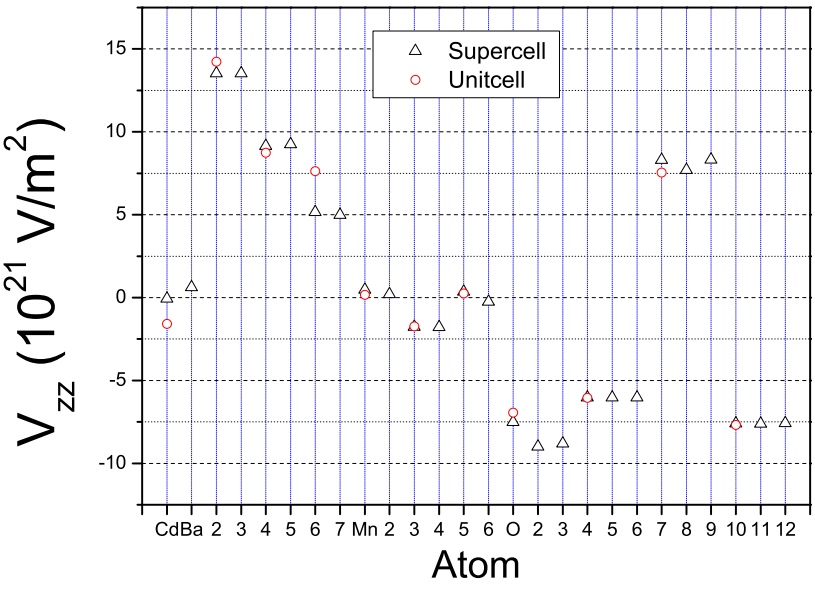

Figure 3.8: V_{zz} obtained for all atoms in a $BaMnO_3$-6H 2x2x1 supercell with one Cd atom substitutional at the Ba1 site; and V_{zz} for a conventional 6H cell with the same substitution.

combustion method [63] or with conventional solid state method, by P. Tavares at the Chemistry department of UTAD.

In the combustion method stoichiometric amounts of $BaNO_3$ and $MnNO_3{\cdot}4H_2O$ (ABCR $> 98\%$) were dissolved in diluted nitric acid. The pH of the solution was adjusted to 5.2 with ammonia solution. The added amount of urea was calculated so that 3 moles of urea were present for each mole of cationic element (Ba+Mn). The solution was stirred and heated to evaporate all water and decompose the urea. At the end of the process (when the temperature reaches 200 °C) the gel auto ignites and a controlled but fast combustion (3 to 5 seconds) yielded a dark powder. This powder was calcinated at 600 °C for 1 hour followed by 700 °C for 5 minutes, grounded with a mortar and a pestle, passed through a 38 μm sieve and pelletized. The pellet was thermal treated at 900 °C for 40 hours regrounded with a mortar and a pestle, repelletized and treated at 1400 °C for 100 hours with quench cooling (less then 1 minute (yielding phase Ba-6H)). For samples prepared by conventional solid state method, $BaCO_3$ (or $SrCO_3$) and MnO_2 were mixed with ethanol and calcinated at 700 °C during 40 hours. Thermal treatments were processed at 900 °C, 1000 °C and 1100 °C during 40 hours with intermediate grindings. Final sintering was performed at 1275 °C for 180 hours with natural cooling, yielding phases Ba -15R and Sr-4H.

The densities of the samples were measured by weighing and volume using a vernier calliper. The x-ray diffraction patterns were obtained in $\theta/2\theta$ mode from 10 to 90° in an XPert Pro diffractometer equipped with a XCelerator detector and a secondary monocromator. The data were analysed using the Powder Cell 2.3 software [64] and structural data from Adkin [48]. SEM was performed using a FEI Quanta 400 equipped with an EDS from EDAX.

These samples were subsequently implanted with the radioactive ^{111m}Cd and ^{111}In probes, with concentrations in the order of ppm. The isotope beams were produced at the ISOLDE-CERN facility, and the implantation was done in high vacuum at room temperature, at 60 keV, with a dose of approximately 1×10^{12} atoms.cm^{-2}.

In the $\gamma - \gamma$ perturbed angular correlation method, the directional correlation of the two gamma decays in a decay cascade of the radioisotope probe is perturbed by the hyperfine interactions, which depend on the nuclear properties of the isotope and on the extranuclear local environment [22].

The ^{111m}Cd probes decay to ^{111}Cd with two consecutive γ decays. The intermediate state has a half life $t_{1/2} = 45\ ns$ while the parent state decays with $t_{1/2} = 48$ minutes. The quadrupole nuclear moment of the intermediate nuclear state relevant for the hyperfine interaction is $Q = +0.77b$ (taken from [24]). The ^{111}In probes decay to the same intermediate state.

All of the relevant experimental information is condensed in the anisotropic ratio function $R(t)$, expressed as $R(t) = \sum A_{kk} G_{kk}(t)$, a function of time, where A_{kk} are called anisotropy coefficients and depend on the spins and multipolarity of the γ decays, and $G_{kk}(t)$ contains the information of the hyperfine parameters, relevant to the system under study. The anisotropy coefficients after detector solid angle corrections are shown in table 3.8.

Table 3.8: Anisotropy coefficients of the $\gamma - \gamma$ cascade from ^{111m}Cd$\rightarrow^{111}$Cd and ^{111}In$\rightarrow^{111}$Cd.

Parent nucleus	A_{22}	A_{24}	A_{42}	A_{44}
^{111m}Cd	0.1258	-0.0956	-0.0006	-0.0004
^{111}In	-0.1121	-0.0716	-0.0003	-0.0004

A numerical fit of the R(t) function with its Fourier analysis, taking appropriate nuclear and transition parameters, yields the hyperfine parameters, EFG and magnetic hyperfine field [23]. The quadrupolar electric interaction gives the electric field gradient, by knowing the quadrupolar moment of the probe nucleus .

Each measurement at different temperatures was done with a different sample, this was required to get good statistics in the life time of the isotope. Preceding each measurement the samples were annealed in vacuum at 700 °C during a period of 20 min, to remove defects from implantation. These conditions were found to be enough in previous studies of other manganites [6, 65, 5, 66, 67].

In our studies the magnetic hyperfine field is not detected. $SrMnO_3$, known to have $T_N = 278$ [54] or 350 K [50], will be paramagnetic at all temperatures measured (150, 300 and 700 °C), except for room temperature, where it may be antiferromagnetic. For $BaMnO_3$, the Néel temperature depends of the polytype. For the phases of interest, 6H and 15R, its values are of the order 250 K [48], so that also on almost all temperatures measured it is paramagnetic.

X-ray powder diffraction was used not only for the structural identification and quality check of the samples, but also to check that the conditions of implantation, annealing and measurement had no observable influence on the initial state of the samples. In these final measurements (at Univerisidade de Aveiro, by R. Soares), the Cu anode was used, with wavelenghts $K\alpha_1 = 5.406$Å,

$K\alpha_2$ = 5.443 Å, and $K\beta$ = 1.39225 Å. The scanning is continuous with a step size of 0.001 degrees, and $15 < 2\theta < 90$. X-ray spectra were taken at various high temperatures, including several hours at a temperature of 900 °C, to check that the annealing of 700 °C, during 20 minutes before the PAC measurement has no influence on the structure. Refinement parameters of representative powder diffraction patterns are shown in table 3.9.

For $BaMnO_3$, the several possibilities of different phases (4H,7H,15R,6H,...) that could appear are not easily distinguishable in the diffraction patterns to exclude that some structural changes occurred with the implantation or annealing.However, this is unlikely, given the consistent PAC results on the several temperatures measured for $BaMnO_3$-6H, as we will show. The $BaMnO_3$ 2H, the most stable low temperature structure, however, is easily eliminated from this set of possible structures on all diffraction patterns.

Table 3.9: Main refinement parameters of XRD (at room temperature) for some of the studied samples, and lattice parameters a and c (Å). $SrMnO_3$-1: 4H structure, PAC measurement at 150 °C. $BaMnO_3$-1: 6H structure, PAC measurement at 400 °C. $BaMnO_3$-21: sample with the 6H structure. $BaMnO_3$-23: The same sample measured at 900 °C. $BaMnO_3$-3: 15R sample, PAC measurement at 400 °C.

Sample —	Phases —	R_P —	R_{wp} —	R_{exp} —	a —	c
$SrMnO_3$-1	4H	12	18	3.15	5.4526	9.0841
$BaMnO_3$-1	6H	6	10	0.52	5.6277	13.9730
$BaMnO_3$-21	6H	39	51	0.54	5.6652	13.9678
$BaMnO_3$-22	6H	34	45	0.51	5.6877	14.0447
$BaMnO_3$-23	6H	32	44	0.45	5.7162	14.0316
$BaMnO_3$-3	15R	3	4	0.65	5.6978	35.3354

Measurements of magnetization temperature dependence were also performed in the studied samples, one for each different phase. A vibrating sample magnetometer was used, with T magnetic field $B = 5$ T for $SrMnO_3$-4H and $BaMnO_3$-15H, and $B = 0.5$ T for $BaMnO_3$-6H. The results are presented in figure 3.9. Small nomalies are detected, signaling magnetic transitions, in $SrMnO_3$, at 280 K (7 °C), in $BaMnO_3$-6H, at 280 K, and in $BaMnO_3$-15R, at 260 K (-16 °C).

PAC - $SrMnO_3$

The $SrMnO_3$ PAC spectra for temperatures of 150, 300 and 700 C are shown in figure 3.10(a).

The spectra can be reasonably fitted with two distinct local environments, fractions of 50 %. V_{zz} are shown for 50/50 fractions and asymmetry fixed to 0 in figure 3.10(b).

However, other values as far as 30/70 % or 70/30 % for the two fractions also provide a reasonable fit, so it is not possible to determine with any certainty the ratio of the two fractions, due to the highly attenuated spectra and statistical error. If we assume the fractions fixed at 50/50 and asymmetry values fixed at zero (also not crucial to the fit with these spectra), the higher, best defined value of V_{zz}, and the lower V_{zz} are found to be almost constant in the temperature range (150-700 C). This is consistent with the similar behavior in the $CaMnO_3$ system [6]. The calculations of the two substitutions of Cd in the two Sr sites, shown earlier,

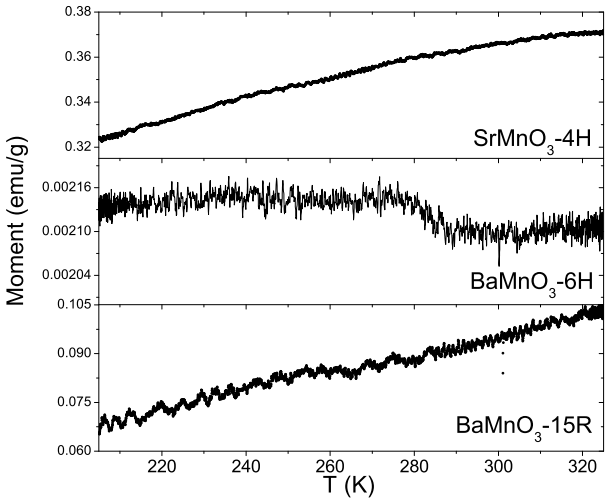

Figure 3.9: Magnetization as a function of temperature for the samples: *Upper figure*: $SrMnO_3$-4H. *Middle figure*: $BaMnO_3$-6H . *Lower figure*: $BaMnO_3$-15R .

give two values of V_{zz} in qualitative agreement, as the values are rather close (figure 3.10(b)). These results suggest that the Cd probe occupies substitutionally both Sr sites, even though calculations predicted Cd substitutional at the Sr 2 site to be slighlty more stable. The V_{zz} of lower magnitude is almost constant as, far as we can tell, since given the limited time window the fit of a low EFG is not very accurate.

PAC - $BaMnO_3$

The spectra for the 6H-$BaMnO_3$ taken between 16 and 700 C do not present appreciable frequency changes, and similarly the obtained EFG are constant, as shown in figures 3.11 and 3.13. In this case the comparison with the first-principles calculations shows that one of the experimental frequencies measured is too high ($\approx 12 \times 10^{21} V/m^2$) to be accounted by any of the values calculated with the Cd probe substitutional in a Ba site. Surprisingly this is also the most well defined fraction of the spectrum, with the smaller line width for the frequencies [figure 3.13], but cannot be assigned to a Ba site. Its fraction is very large (40-50%) and well defined, of a unique local environment. We may speculate that the corresponding Cd probes are favorably located near oxygen vacancies, producing this high EFG, but no calculation exists that confirms this. The lower electric field gradient values of the other fractions may be interpreted as substitutional Cd atoms at the Ba sites since its value is between the different calculated values at the inequivalent Ba sites.

In this case, to get more information and confirm the previous measurements, we have also implanted the probe ^{111}In/^{111}Cd on 6H-$BaMnO_3$ samples. While the initial state of the $\gamma - \gamma$ cascade is different from the ^{111m}Cd and has different anisotropy coefficients, the intermediate state of the γ-γ cascade is the same, and if the ^{111}In probe goes to the same lattice sites when implanted as ^{111m}Cd, we should get the same quadrupole frequencies. The samples were measured with this probe in the temperature range 16-850 C. The spectra are, as expected,

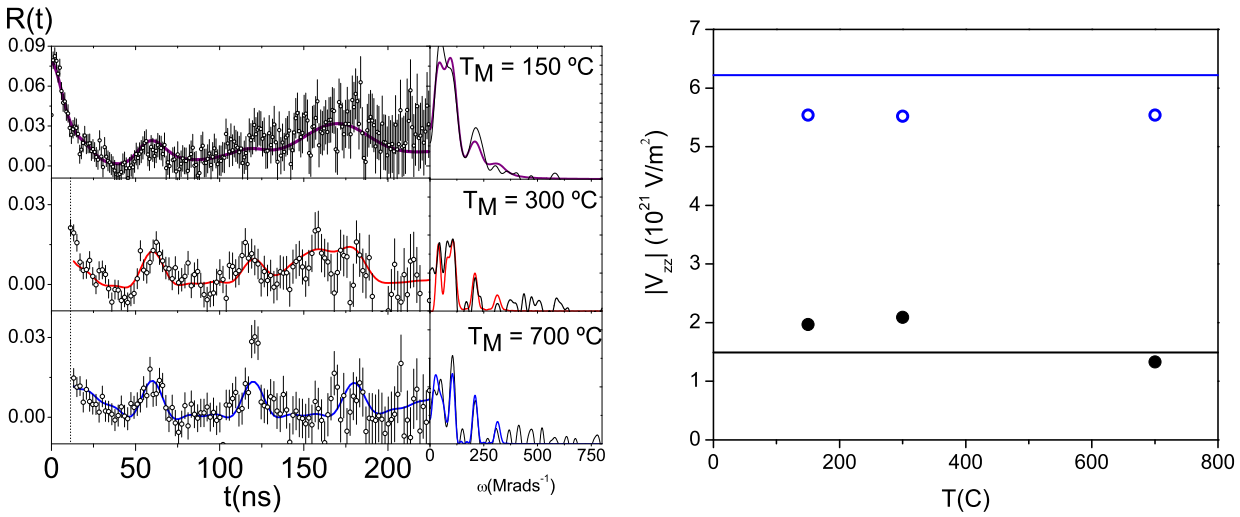

Figure 3.10: *Left figure*: $SrMnO_3$ sample: the lines represent the fits to the spectra of the perturbation functions, at temperatures of 150 (up) , 300 (middle) and 700 C (down). For all three spectra, the frequencies taken from the fits are approximately equal. Right: Fourier transforms. *Right figure*: The circles represent the experimental V_{zz} obtained with two fractions (open and closed circles). The horizontal lines represent the V_{zz} obtained by DFT calculations with highly diluted Cd probes substituting either one of the two inequivalent sites in the structure.

almost constant on this range of temperatures (13, 16, 206, 409, 510, 611, and 848 C). R(t) representative functions and its Fourier transforms are shown in figure 3.12. There is a slight increase of the frequencies of the higher V_{zz} with increasing temperature, as in the ^{111m}Cd probe case. Unlike the Cd probe case, the fit has to be done not with two, but three fractions. There are two fraction in agreement with the ^{111m}Cd case and there is a third fraction, also high in comparison wih the calculations. Therefore also in this case a fraction of the probes ($\approx 40\%$) must be substitutional at the Ba site, with the lower V_{zz}, while for the other environments we cannot assign a specific site. Perhaps the additional fraction is due to defects caused by the implantation of ^{111}In which were not removed with annealing as in ^{111m}Cd implantations.

Figure 3.14 shows measurements in the 15-R polymorph samples. The perturbation functions are quite attenuated and low frequencies are measured at all temperatures 77K ,RT, 300 C and 700C.

At room temperature and above, two different EFG environments clearly give a much better fit than just one EFG. At 77 K, due to the large statistical error, this is not so clear, but in order to be consistent with the room temperature measurement, two EFGs were used in all fits. The fractions of the two environments are approximately 84% and 16% in all the fits (again, for the low temperature there was a large range allowed due to the larger error, but the values were fixed in $f_1 = 84\%$ and $f_2 = 16\%$). The electric field gradient parameters for both fractions are shown in table 3.10. The V_{zz} parameters are interspersed values on the range 1.89 to 3 for fraction f_1 and 3.1 to 5.6 $\times 10^{21} V/m^2$ for fraction f_2. These small variations may exist due to structural variations with temperature or dynamic effects. These values are close to the calculated values at Cd and the lowest experimental Cd V_{zz} in the BMO6H polymorph, indicating also substutional

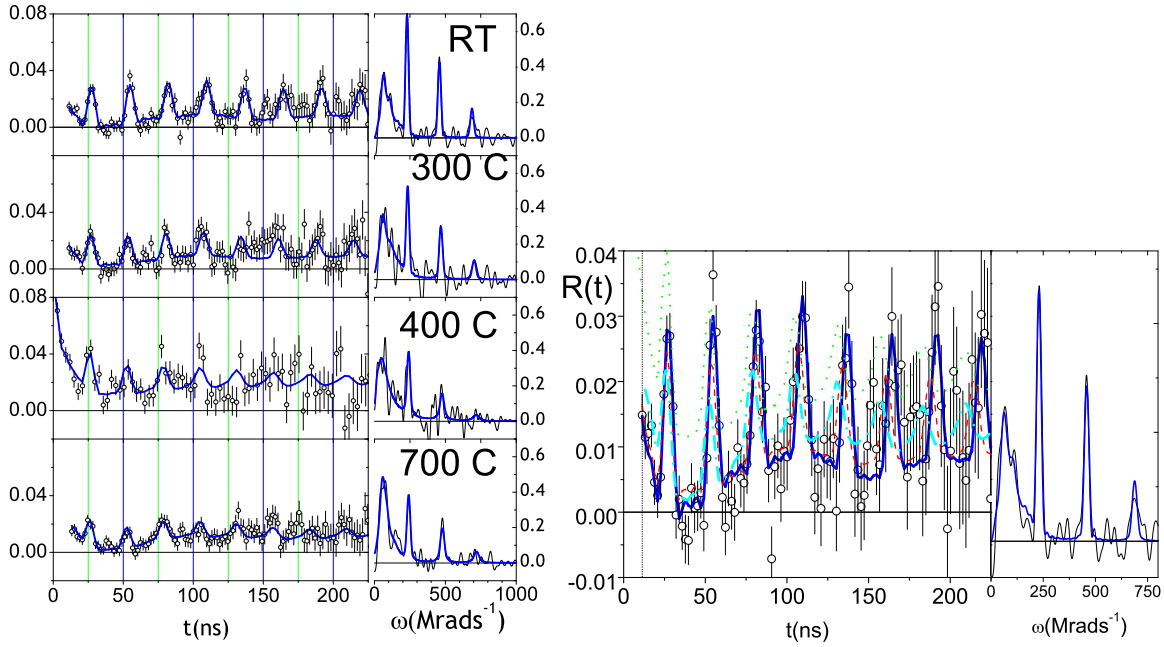

Figure 3.11: *Left*: Experimental ^{111m}Cd/^{111}Cd perturbation spectra for the $BaMnO_3$-6H sample at the measured temperatures and Fourier Transform (RT), showing quadrupolar frequencies approximately constant. This is illustrated in the *right* figure, where all the $R(t)$ graphics are superimposed.

Cd at the Ba sites in this case.

Table 3.10: Electric field gradient (V_{zz}, in $10^{21}V/m^2$) taken from the PAC measurements of $BaMnO_3$, in the rhombohedral 15R polymorph, at four different temperatures. At 30 C the spectrum was fitted with two environments, in that case the V_{zz} of the left column is fitted with a fraction of 84%, and the right column V_{zz} corresponds to 16%.

T	Vzz of f_1	V_{zz} of f_2
77 K	2.58	5.55
30 °C	1.89	3.12
300 °C	2.62	4.66
700 °C	3.00	3.72

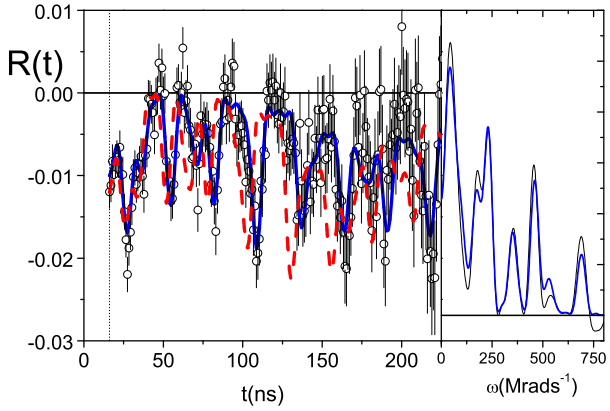

Figure 3.12: Experimental perturbation spectra (left) and Fourier Transforms (Right), for the $BaMnO_3$-6H sample measured at room temperature (full line) and 850 C (dashed line), with the probe $^{111}In/^{111}Cd$. The Fourier transform plot is for room temperature.

3.3.4 Conclusion

The values of the EFG were measured with the ^{111}Cd probe using the PAC method. To our knowledge this is the first characterization at this atomic-like scale in the phases studied. It is found that V_{zz} is roughly constant in a range of temperatures 20-700 C, for both $BaMnO_3$-6H and $SrMnO_3$. First-principles calculations of the EFG with the accurate FLAPW method are reported. The calculated EFG at all atoms is reported, with $SrMnO_3$ in the low temperature structure, and various polytype structures of $BaMnO_3$. The calculations are largely insensitive to the magnetic order or GGA approximation used, and the relaxed structures give consistent results with the experimental structures. For direct comparison with the experiments, we performed calculations with supercells and introducing a Cd impurity substitutional at the alkaline-earth sites. In the case of $SrMnO_3$ there is a good qualitative agreement, which shows that the Cd probe occupies the Sr sites. For the case of $BaMnO_3$-6H, although the calculated values are of the order of one of the measured V_{zz} values, other high values remain incompatible with the divalent alkaline-earth substitution. For $BaMnO_3$-15R, the EFG has values of the order expected if Cd occupies the Ba sites. The main result concerning the temperature dependence of the EFG parameters is that they do not change appreciably in the range studied $T \geq 300$ K.

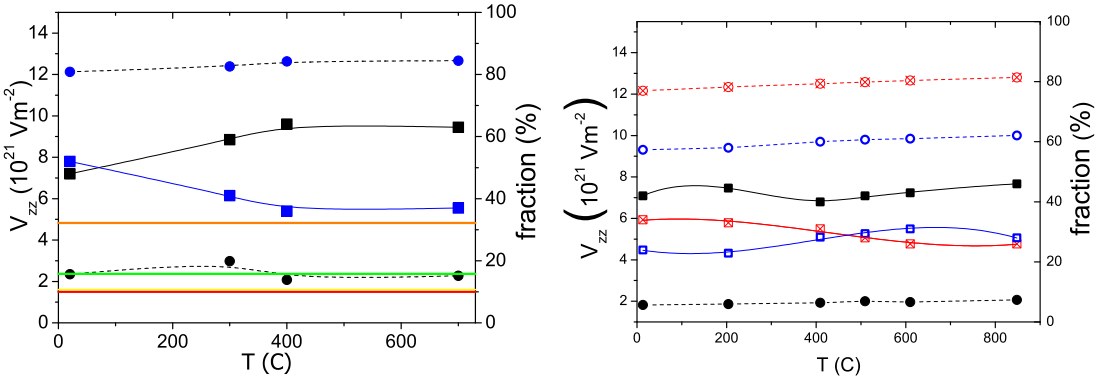

Figure 3.13: *Left*: The circles represent the experimental EFG of $BaMnO_3$-6H implanted with ^{111m}Cd/^{111}Cd. There are two distinct environments measured, about 12 and $2.5 \times 10^{21} V/m^2$, differentiated by empty or full symbols, respectively . The fraction of each environment is represented by the squares, full or empty, according to the corresponding V_{zz}. The four straight horizontal lines are the results of four calculations, considering a Cd probe substitutional at each one of the four inequivalent Ba atoms in the 6H structure. *Right*: The circles represent the experimental EFG of BMO6H implanted with ^{111}In/^{111}Cd. There are three distinct environments measured, about 12, 9.5 and $2 \times 10^{21} V/m^2$, differentiated by the symbols (crossed, empty and full, respectively) in the plot. The fraction of each environment is represented by the corresponding squares.

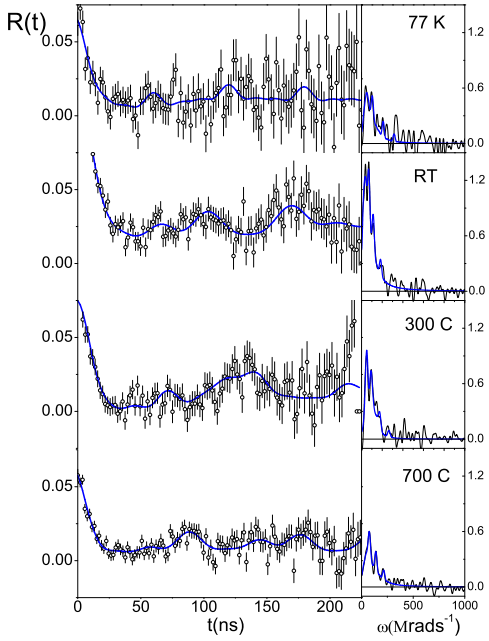

Figure 3.14: Experimental ^{111m}Cd/^{111}Cd perturbation spectra (left) and Fourier Transforms (Right) for the $BaMnO_3$-15R sample, showing that the quadrupolar frequencies are relatively low at all temperatures measured.

Hyperfine parameters from first-principles in rare-earth multiferroic hexagonal manganites $RMnO_3$ (R = Y, Ho, Er, Lu)

J. N. Gonçalves and V. S. Amaral
Departmento de Física and CICECO, Universidade de Aveiro, 3810-193 Aveiro, Portugal

J. G. Correia
CERN EP, CH 1211 Geneva 23, Switzerland and Instituto Tecnológico e Nuclear, Estrada Nacional 10, PT-2686-953 Sacavém, Portugal

3.4 Electric field gradients calculated from first-principles in hexagonal manganites

Abstract

We present density functional theory calculations of the electric field gradients and magnetic hyperfine fields in the hexagonal rare-earth multiferroic manganites $YMnO_3$, $HoMnO_3$, $ErMnO_3$ and $LuMnO_3$, with the L/APW+lo (WIEN2K) method. For $YMnO_3$, we discuss the changes of the hyperfine parameters and electronic structure due to the influence of different magnetic orders, electronic correlations, spin-orbit coupling, and atomic coordinates. The hy-

perfine parameters, compared in all atoms, reveal different sensitivities to the type of calculation for the different atomic sites. The variation of the hyperfine parameters with respect the other compounds is also analysed.

3.4.1 Introduction

The rare-earth hexagonal multiferroic manganites $RMnO_3$ (with R = Y, Ho, Er, Tm, Yb, Lu, rare-earths with small ionic radii) have coexisting ferroelectric and antiferromagnetic orders at low temperatures. The structure is different from the perovskite based structures of other ABO_3 oxides [10, 68]: the Mn atoms form two-dimensional triangular lattices, linked by oxygen atoms and separated by layers of rare-earth and oxygen atoms, forming MnO_5 bipyramids between rare-earth planes. The ferroelectric phase ordering occurs at $T_C \sim 800 - 1200$ K while the magnetic transition occurs at much lower temperatures $T_N \sim 80$ K. The high temperature paralectric phase and the low temperature ferroelectric phase have the space groups $P6_3/mmc$ and $P63cm$, with symmetry loss in the ferroelectric phase associated to a tilting of the MnO_5 bipyramids and a buckling of the rare-earth horizontal planes (A still higher temperature paramagnetic paraelectric phase with space group $P6/mmm$ is predicted, but will not be studied within this work. An intermediate phase between $P6_3/mmc$ and $P63cm$ has also been proposed on the basis of some measurements [69], but it was discarded experimentally [70] and by calculations [71]). In the case of $YMnO_3$ it was argued that the ferroelectricity originates from the electrostatic interactions resulting from the structural changes alone, associated to the Y atoms, without the involvement of hybridization changes [72], in distinction to conventional perovskite ferroelectric oxides [73]. However, more recently other studies have found that that rehybridization is involved, but from the Y d^0-ness instead of from the Mn atoms [74]. For $HoMnO_3$, ab-initio calculations of the Born effective charge tensor [75], local hybridization [76], and local structure measurements in $HoMnO_3$ [75] indicate that the ferroelectric transition is associated to the displacements of Ho atoms, and consequent asymmetric bonding with the apical oxygen atoms.

One source of information which may prove useful to study the competition of different phases in these compounds are measurements of the hyperfine parameters. The hyperfine interactions can be used by such techniques as perturbed angular correlations (PAC), nuclear magnetic resonance (NMR) and Mössbauer spectroscopy to get information sensitive to the atomic environment of the probe nuclei. The interpretation of the data is not always straightforward, but first-principles calculations can help to complement the experiments, using the calculated hyperfine parameters, such as Electric Field Gradient (EFG) and Magnetic Hyperfine Field (MHF). In addition, the hyperfine parameters are usually very sensitive to any changes in the material, thus suitable to study the interplay of various orders present in these compounds, and to test of the accuracy of DFT calculations.

The EFG is the second-rank symmetric traceless tensor of second derivatives of the electric potential relative to spacial coordinates, at the nuclear position. It can be characterized by its diagonal components, defined by their absolute value as $|V_{zz}| > |V_{yy}| > |V_{xx}|$ (usually V_{zz} and a second parameter $\eta = (V_{xx} - V_{yy})/V_{zz}$ are used in the analysis of measurements), and by three

vectors corresponding to the direction of each diagonal component.

The relativistic MHF can be split into three main contributions [77]: the contact field, B_C, is the spin density at the nucleus averaged over the Thomson radius, $r_T = Ze^2/mc^2$; and the relativistic analogous of the spin dipolar and orbital hyperfine fields: $B_{hf} = B_C + B_{dip.} + B_{orb.}$

In this work we will study the EFGs and MHFs in the hexagonal manganites obtained by density functional theory (DFT) calculations. For the case of $YMnO_3$ we study both high and low-temperature phases, along with the influence of several factors: magnetic order, exchange-correlation functional, with/without additional U to account for electronic Coulomb correlations, with/without spin-orbit coupling and relaxation of symmetry unconstrained atomic coordinates. For the other compounds we concentrate on the ferroelectric phases.

Calculation Details

We use the full potential (linearized) augmented plane-wave + local orbitals ((L)APW+lo) ([78] and references therein) method with the WIEN2K code implementation. With this method, the valence electrons are calculated with atomic like functions (product of radial functions and spherical harmonics) inside atomic spheres and plane waves in the interstitial space. The spheres radii used are 2.2, 1.8 and 1.6 *a.u.* for the rare-earths, Mn and O, respectively. In the ferroelectric phase, a grid of 8 **k**-points in the irreducible Brillouin zone was used (4x4x2 grid in the full Brioullin zone) for the integration in reciprocal space, with the tetrahedron method [79]. The calculations for the valence electrons are performed in the scalar-relativistic approximation [80] except if noted otherwise, when spin-orbit coupling is included [81], whereas core electrons are treated fully relativistically. The basis size allows plane waves with $K_{max} = 7.5/1.6 = 4.69\ a.u.^{-1}$.

3.4.2 $YMnO_3$

Paralectric Phase

In the high-temperature paraelectric phase, the unit cell consists of two formula units, made of two Mn centered oxygen bipyramids vertically separated by Y planes, and the Mn atoms are triangular lattices, centered in complementary spaces at the two horizontal planes (see fig. 3.15(a)). The lattice parameters, are $a = 3.61$ and $b = 11.39$ Å [82].

The electronic structure for $YMnO_3$ was already calculated taking into accountn the magnetic order and electronic correlation factors , using the LMTO method with the atomic spheres aproximation [83] or projector augmented wave (PAW) [84]. We also give our results, which use a potentially more accurate method for the calculation of hyperfine parameters.

The calculation without spin-polarization in the local density approximation [85], results in a density of states (DOS) showing a high peak at the Fermi level, suggesting instability in relation to ferromagnetism by the Stoner criterion. Accordingly, the spin-polarized ferromagnetic calculation results in a lower total energy by 3.48 eV, and the DOS now has a small number of states at the Fermi energy in the majority spin channel and an energy gap in the minority spin channel. The DOS for the F magnetic order is shown in fig. 3.16(a).

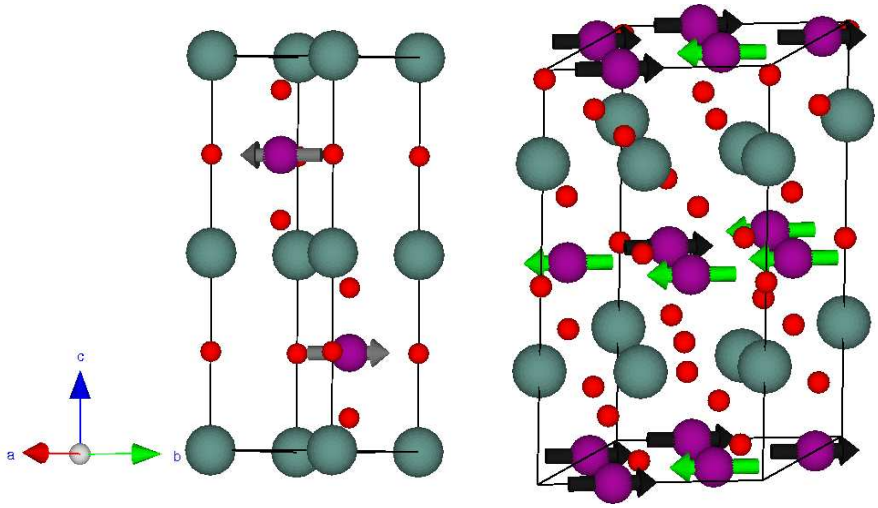

(a) (b)

Figure 3.15: a) Paraelectric and b) Ferroelectric structures of $YMnO_3$, with the A-AF and frustrated magnetic orders of Mn spins considered in the calculations represented by the vectors.

It was found in these previous DFT calculations that both magnetic order and electronic correlations play a role in establishing the insulating gap in $YMnO_3$. In this work, we study the effect of electronic correlations with LSDA + Hubbard U calculations, using an effective parameter $U_{eff.} = U - J$ with the fully localized limit correction from Anisimov et al. [86].

Table 3.11 presents the EFG and MHF calculated with LSDA ($U_{eff.} = 0$) and LSDA+U, with $U_{eff.} = 1.77$, 3.54, 5.31 and 7.07 eV. The last value of $U_{eff.} = 7.07$ eV is similar to $U = 8$, $J = 0.88$ eV obtained from constrained LSDA [83]. Our results show that V_{zz} at the Y atoms is insensitive to the value of $U_{eff.}$, while at the O atoms the values change appreciably but still little with increasing U ($-0.18 \times 10^{21} Vm^{-2}/eV$ at the O1 atoms). The O1 equatorial atoms have three Mn nearest neighbors at 2.08 Å, therefore their sensitivity to the applied correction at Mn is larger than at the O2 apical atoms, with only one Mn nearest-neighbor (albeit closer, at 1.80 Å). Naturally, at the Mn sites, where the orbital-dependent potential is applied, the larger changes are seen. The absolute value of V_{zz} decreases more strongly with the value of $U_{eff.}$ ($0.51 \times 10^{21} Vm^{-2}/eV$). This would suggest that the experimental determination of $EFG(Mn)$ would give an accurate value of the $U_{eff.}$ to take into account in LSDA+U calculations, complementing the band gap measurements normally used for this purpose. However, ferromagnetic order is not the ground state in this compound, and, as will be seen later in the ferroelectric phase,the exact magnetic order also has an influence in the EFG at the Mn site.

The contact MHF is presented and similar sensitivities to the value of $U_{eff.}$ are seen: -0.20 T/eV, -0.96 T/eV, 0.69 T/eV and -0.06 T/eV for Y, Mn, O1 and O2 respectively. The difference in relation to EFGs is that in this case Y also has a small variation, decreasing with the value of U. The contact MHF is dominated by the contribution from the valence electrons in Y and O1, it has small valence/core contributions at O2, and at Mn there is a big core

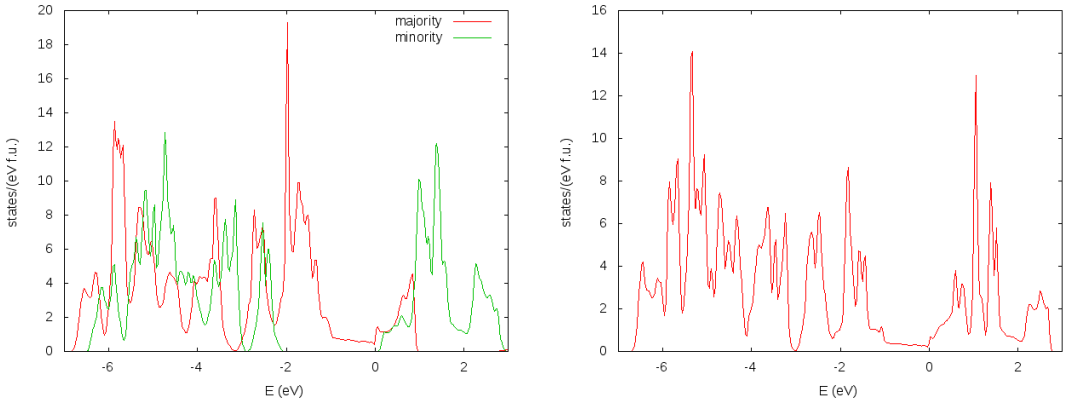

(a) (b)

Figure 3.16: Paraelectric Ferromagnetic (left) and antiferromagnetic A-AF(right) DOS.

contribution ~ -85 T, mainly cancelled by a valence contribution ~ 65 T, yielding the total values ~ -20 T. These core and valence values are anomalously high when comparing with other Mn hyperfine fields (e.g. Mn impurity in Ni [77], or Mn in MnAs [4]), probably due to the fact that the ferromagnetic order is not stable in this triangular lattice. For a more reasonable calculation of the hyperfine fields some kind of antiferromagnetic order should be taken into account. The force obtained at the only free atomic coordinate z at the O2 sites is already small [4.3(-6.5) mRy/a.u. with U=0(7.07)]. In this phase, we do not investigate atomic coordinate relaxations.

Therefore, we now investigate the influence of a different magnetic order. As a first approximation, the A-AF magnetic order is considered - adjacent Mn planes with oppositely directed spins, see fig. 3.15(a). We find that the EFGs and MHFs do *not* change upon change of magnetic ordering from F to A-AF. This reflects the locality of the hyperfine parameters and exchange interactions, consistent with the weak interplane AF coupling found by DFT calculations [84](the Mn interplanar distance is large, 5.70 Å). The DOS for the A-AF case is shown for one or the other spin in fig. 3.16(b) and it is also similar to the F case. Consistently, the F and A-AF states are almost degenerate in energy (F with 0.01 eV lower energy). However, this is till a crude approximation, since the Mn planes are not ordered ferromagnetically but instead have some xy-plane triangular non-collinear order, possibly also with small non-zero z-component. The changes in the hyperfine parameters and electronic structure should only become pronouced upon changing the magnetic order of the Mn atoms in the planes. We will study this influence in the ferroelectric phase.

Subsequently, the spin-orbit interaction was also considered, using the scalar-relativistic basis and the second variational step[81]. While the EFGs and Fermi contact MHFs suffer negligible variations, other contributions for the hyperfine fields are calculated and presented here. The spin dipolar and orbital hyperfine fields, presented in table 3.14, are very significant for Mn and O atoms, which implies the spin-orbit correction should always be included to get accurate MHF values. While the spin-orbit coupling introduced negligible changes in the EFGs for the case of

Table 3.11: V_{zz} (10^{21}V/m^2) and MHF for every atom in the $YMnO_3$ paraelectric structure, considering the experimental structure, with LSDA+U, for different values of $U_{eff.}$ (eV), in the ferromagnetic and A-AF magnetic orders. For the A-AF magnetic order, for each Mn and O atom there exists an inequivalent atom, not shown, with the same EFG, and MHF of opposite sign and the same absolute value.

	Ferromagnetic					A-AF	
	no spin-orbit						spin-orbit
$U_{eff.}$ (eV)	0	1.77.	3.54	5.31	7.07	0	0
Atom	V_{zz} ($10^{21} Vm^{-2}$)						
Y	10.65	10.64	10.65	10.67	10.69	10.64	10.62
Mn	-4.90	-3.90	-2.97	-2.15	-1.26	-4.90	-4.89
O 1	-7.57	-7.27	-6.96	-6.65	-6.29	-7.54	-7.53
O 2	3.38	3.49	3.54	3.53	3.47	3.35	3.34
	B_{hf} (T)						
Y	6.29	5.91	5.55	5.24	4.89	0	0
Mn	-15.03	-16.84	-18.52	-20.02	-21.92	-15.10	-11.21
O 1	11.16	9.88	8.64	7.54	6.23	11.16	6.27
O 2	-0.44	-0.56	-0.66	-0.75	-0.84	-0.71	-8.43

Table 3.12: Decomposition of the total hyperfine fields in contact, orbital and spin contributions, calculated for the A-AF case with inclusion of spin-orbit interactions. For every Mn and O atom, another exists with hyperfine fields of opposite signal (units Tesla).

Atom	B_{hf} (total)	B_{hf} (contact)	B_{hf} (orbital)	B_{hf} (spin)
Y	0	0	0	0
Mn	-11.21	-15.06	13.22	-9.37
O 1	6.37	11.10	-6.10	1.37
O 2	-8.43	-0.50	-5.62	-2.31

$YMnO_3$, with differences of 0.01 V/m^2 in two atoms, it will be shown in the other compounds, with f-shell lanthanides, that the spin-orbit coupling introduces significant changes in the EFG.

The results obtained for the total DOS are in good agreement with previous first-principles electronic structure calculations, with other methods [83, 87, 84].

3.4.3 Ferroelectric Phase

We now investigate the ferroelectric $P63cm$ phase. We used for the starting structure the XRD measurements in $YMnO_3$ single crystal by van Aken et al. [88].

Exchange-correlation potential and atomic coordinates Table 3.13 shows the V_{zz} calculated with the LDA and GGA-PBE functionals, for the ferromagnetic case, but this time also by relaxing the atomic coordinates to the most stable theoretical structure within the $P63cm$ space group. In general the experimental lattice constants give more reliable results than either LDA or GGA optimized lattice constants, which are usually underestimated or overestimated, respectively. Therefore the lattice constants are kept at the experimental values here. We can see that at least qualitatively the EFG remains the same with the atomic coordinates relaxed

Table 3.13: V_{zz} ($10^{21}V/m^2$) in the ferroelectric structure, for $YMnO_3$, with ferromagnetic order, for the experimental and relaxed structures, including three exchange-correlation funcionals: LDA (with/without $U_{eff.} = 7.07$ eV), and GGA (PBE). The last row shows the magnetic moments the Mn AWP spheres, in μ_B units

Atom	LDA	LDA rel.	GGA	GGA rel.	LDA+U	LDA+U rel.
Y 1	0.48	0.42	0.53	0.66	0.43	0.84
Y 2	6.06	5.73	6.14	6.21	6.08	5.97
Mn	-5.18	-5.07	-4.73	-4.06	-1.65	-1.24
O 1	3.37	3.36	3.38	3.55	3.34	3.61
O 2	3.12	3.26	3.14	3.43	3.26	3.58
O 3	-8.12	-8.15	-8.09	-8.19	-6.87	-6.84
O 4	-7.59	-7.69	-7.51	-7.64	-6.22	-6.30
μ_{Mn}	3.30	3.30	3.32	3.33	3.59	3.60

Table 3.14: Decomposition of the total hyperfine fields in contact, orbital and spin contributions for $YMnO_3$, calculated for the frustrated AF case with inclusion of $U_{eff.} = 7.07$ eV and spin-orbit interactions in $YMnO_3$. For every atom, another exists with hyperfine fields of opposite signal and approximately the same absolute value. The average value is presented.

Atom	B_{hf} (total)	B_{hf} (contact)	B_{hf} (orbital)	B_{hf} (spin)
Y 1	-1.01	-0.95	0.01	-0.07
Y 2	0.79	0.77	0.00	0.02
Mn 1	-23.88	-27.44	-2.77	6.33
Mn 2	-27.35	-30.83	-2.86	6.34
O 1	0.46	-0.98	0.18	1.26
O 2	0.47	-0.94	0.18	1.23
O 3	0.54	-0.91	0.18	1.27
O 4	0.58	-0.84	0.19	1.23
O 5	0.03	1.70	-0.04	-1.63
O 6	2.26	1.67	0.08	0.51

in all cases. The calculated magnetic moments at the Mn atoms are presented also in the table, and show almost no change with the relaxation. In average, for the LDA+U case, the V_{zz} and atomic coordinates of the relaxed structure are closer to the case of the experimental structure. This is expected, since it has already been seen that this is approximation, together with an approximated antiferromagnetic order, correctly reproduces the energy gap in this compound [83]. The FM order gives a direct gap much smaller than observed.

As seen before in the paraelectric phase, the Y and O apical atoms are almost insensitive to the inclusion of U, while the O equatorial atoms, have small but discernable changes and the Mn atoms have large changes.

Hyperfine Fields

The Fermi contact hyperfine fields, at all the atoms within the GGA ferromagnetic calculations, using the experimental and relaxed (forces less than 5 $mRy/a.u.$) structures are shown in tab,le 3.15. The hyperfine fields suffer small variations of less than 0.2 T between structures.

Table 3.15: Fermi contact hyperfine field (T) for every atom in the $YMnO_3$ ferroelectric structure, considering the experimental atomic fractional coordinates, and theoretically determined coordinates.

Atom		GGA			GGA rel.	
	total	core	valence	total	core	valence
Y 1	6.11	0.00	6.11	5.98	0.00	5.97
Y 2	6.66	0.00	6.66	6.46	0.00	6.46
Mn	-17.84	-45.09	27.26	-18.04	-45.19	27.15
O 1	-0.37	-0.50	0.13	-0.31	-0.47	0.17
O 2	-0.29	-0.58	0.29	-0.23	-0.54	0.31
O 4	10.66	-0.73	11.39	10.55	-0.73	11.28
O 3	10.85	-0.69	11.55	10.80	-0.70	11.50

The larger value is obtained at the Mn sites, but the Y and oxygen atoms at the Mn planes (3 and 4) also have sizeable hyperfine fields of opposite sign. The separation in core and valence contributions shows that this is a contribution of the valence electrons. In the Mn atoms however there is the core polarization of the inner s electrons by the valence $3d$ electrons, which results also in a large core contribution of opposite sign.

The relative differences in hyperfine fields due to the strucutural relaxations are generally smaller than the ones obtained with the EFGs.

Frustrated magnetism We have also considered, as an approximation to the complex non-collinear spin order, following [83], a collinear calculation with a frustrated magnetism where one Mn atom has an opposite spin to the other two Mn atoms in that plane (see fig. 3.15(b)). The energy is 0.49 eV lower than for the ferromagnetic case. There are 20 different atoms with differents EFGs due to the loss of magnetic symmetry, four Mn atoms, eight apical and four equatorial oxygen atoms. It is found, however, that this loss of symmetry nevertheless leaves pairs of atoms with approximately the same values of V_{zz}. The averages of V_{zz} for the ten pairs of atoms are presented in table 3.16. Comparing the LDA calculation with the ferromagnetic case, the larger change is again seen at the Mn atoms, with an absolute value decrease from 5.18 to 3.70/2.98. Qualitatively V_{zz} for the other atoms stays the same. Further including the spin-orbit coupling does not change Vzz. Finally, including $U_{eff.} = 7.07$ eV further reduces the absolute value of V_{zz} at all sites, but with more relevant change at the Mn sites, down to $\sim 1 \times 10^{21} V/m^2$.

3.4.4 Other hexagonal rare-earth manganites

Table 3.17 shows the calculations of EFG (V_{zz}) in other three hexagonal manganites, $LuMnO_3$, $ErMnO_3$ and $HoMnO_3$ at the GGA level of approximation, with experimental and relaxed structures (For these calculations $RK_{max} = 6$ was used, which already gives relatively good convergence for the EFG). It is seen that the influence of the relaxations is small for the O atoms in all compounds. However it is somewhat larger at the Mn site, and larger still at the rare-earth sites. In $ErMnO_3$ and $HoMnO_3$ the differences obtained with relaxations are larger than those

Table 3.16: V_{zz} (10^{21} V/m^2) calculated for the frustrated antiferromagnetic structure of $YMnO_3$. Pair of inequivalent atoms have very similar V_{zz} and the average value for each of these pair is presented.

Atom	LDA	LDA+spin-orbit	LDA+spin-orbit+U
Y 1	0.66	0.66	0.44
Y 2	6.26	6.27	6.12
Mn 1	-3.70	-3.70	-1.02
Mn 2	-2.98	-2.98	-0.84
O 1	3.53	3.54	3.35
O 2	3.67	3.67	3.33
O 3	3.33	3.33	3.20
O 4	3.50	3.50	3.21
O 5	-7.54	-7.75	-6.54
O 6	-7.20	-7.20	-5.85

Table 3.17: V_{zz} (10^{21}V/m^2) for every atom in the $LuMnO_3$, $ErMnO_3$ and $HoMnO_3$ ferroelectric hexagonal structures considering the experimental atomic fractional coordinates, and relaxed free coordinates, with the GGA-PBE approximation, and inclusion of spin-orbit (so) coupling in the the columns denoted with so.

	$LuMnO_3$			$ErMnO_3$			$HoMnO_3$		
Atom	exp.	rel.	rel.+so	exp.	rel.	rel.+so	exp.	rel.	rel.+so
R 1	-1.94	-0.88	-0.85	-3.74	-0.95	-1.06	3.78	-1.26	3.82
R 2	14.25	13.48	13.52	9.66	11.16	11.35	11.01	14.27	15.62
Mn	-3.59	-3.20	-3.21	-5.71	-5.28	-5.50	-4.40	-3.92	-4.23
O 1	3.15	3.47	3.44	3.41	3.40	3.48	3.40	3.67	3.53
O 2	3.17	3.27	3.25	3.44	3.45	3.53	3.32	3.76	3.50
O 4	-7.41	-7.71	-7.76	-8.66	-8.49	-8.57	-7.54	-5.79	-8.00
O 3	-7.10	-7.17	-7.23	-8.07	-8.06	-8.16	-7.83	-5.71	-7.50

obtained in the $YMnO_3$ and $LuMnO_3$. This is consistent with the added uncertainty in view of the assumed magnetic order in these cases, since the open f-shell of Er and Ho produces additional magnetic interactions which are not accounted for.

We further include spin-orbit interaction at the rare-earth sites, in the relaxed structure determined previously, which is found to give significant differences in the $HoMnO_3$ case.

While in the $YMnO_3$ case it was seen that the effects of structural relaxations were small on the hyperfine parameters in the ferromagnetic case for several calculations, in the cases of $HoMnO_3$ and $ErMnO_3$ the magnetic order is found to have a larger influence, since with the fictitious ferromagnetism in these compounds the forces are high, especially at the Mn atoms, resulting in larger changes with relaxation, but nevertheless with good qualitative agreement.

3.4.5 Conclusions

We performed a series of calculations in the $YMnO_3$ hexagonal compound to determine the influence of different factors in the hyperfine parameters. The hyperfine paraters for Y atoms are insensitive to changes in both magnetic interactions and correlation effects. The calculation

without spin-polarization is unstable in relation to the spin-polarized calculations, with the same structure. Only in this case there are also changes in the EFG at the Y sites, with respect to the ferromagnetic case. The LDA+U approximation, with $U_{eff} = 7eV$, in agreement with previous calculations, gives a good description of this compound, seen here by smaller deviation of the EFG between experimental and theoretical structure. Spin-orbit interaction is found to have no appreciable role in the hyperfine parameters in $YMnO_3$, but a more significant role in the other cases. It is concluded that calculations of hyperfine quantities must be carefully compared with accurate experiments, which would also be a good indicator of the more important physics taken into account by the calculations that correctly describes this compound, and also other rare-earth manganites.

With the other rare-earths there are no qualitative differences between the EFGs at the experimental and relaxed structures, already at the GGA approximation level. However, the calculations with corrections to account for the highly localized Mn-d and rare-earth-f electrons (in Er and Ho) would probably give larger differences.

3.4.6 Calculations for comparison with PAC results

A main motivation for calculations performed in these compounds is the direct comparison with calculations. In the experiments, a usual probe is a highly diluted ^{111m}Cd/^{111}Cd isotope. Therefore, we end this chapter with a presentation of calculations in these compounds with Cd impurities assumed to occupy the rare-earth or manganese cation positions. Some of the factors to take into account in this kind of calculations are also briefly discussed. In order to reproduce the structural changes in the vicinity of the probe, the free atomic coordinates of the $P63cm$ space group (z_{R1} , z_{R2} , x_{Mn} , z_{Mn} , x_{O1} , z_{O1} , x_{O2} , z_{O2} , z_{O3} , z_{O4}) were optimized, while the experimental lattice constants were used.

Table 3.18 presents the calculations with Cd, for the rare-earth manganites considered, substitutional at the rare earth and manganese sites. The calculations assume ferromagnetism. Even though the interplanar Mn order should affect the EFG at manganese as was shown previously, this should not show differences for the EFG at Cd, specially if it is occupying the rare-earth sites. The radius of the Cd sphere is the same of the substituted atom, as defined previously.

For each EFG calculation per crystallographic site (R1, R2 or Mn), Cd was included in the structure by substitution at one of the sites in the unit cell, giving the formula $R_{5/6}Cd_{1/6}MnO_3$ or $RMn_{5/6}Cd_{1/6}MnO_3$. In principle a supercell calculation with a more diluted Cd probe would give a more accurate result. However a test with a larger supercell showed no large differences. Another fact worth considering is that in these materials the use of an on-site Coulomb potential may give more precise results. Using $YMnO_3$ and $HoMnO_3$, as test cases, with a substitutional Cd atom at the rare-earth and manganese sites ($R_{5/6}Cd_{1/6}MnO_3$ or $RCd_{5/6}Mn_{1/6}O_3$), the LDA+U functional was used with an effective Hubbard parameter $U_{eff} = 6$ eV for the Ho $4f$ orbitals. However, also in this case the main changes found for V_{zz} in a test with $U_{eff.}$ at the Mn sites should be at the Mn sites, and a Coulomb potential at the rare-earth f orbitals should

Table 3.18: EFG parameters (V_{zz} (10^{21}V/m^2) and η for Mn site) calculated for some rare-earth manganites $RMnO_3$ (R=Y, Ho, Er, Lu), considering one Cd probe substitutional at the rare-earth and manganese sites, with the measured structure and after atomic structure relaxation.

Sample	V_{zz} (R1)	V_{zz} (R2)	V_{zz} (Mn)	η	V_{zz} (R1)	V_{zz} (R2)	V_{zz} (Mn)	η
$YMnO_3$	0.08	4.10	-18.67	0.06	1.38	6.61	-23.90	0.06
$HoMnO_3$	1.38	3.41	-17.18	0.01	1.31	6.16	-21.17	0.02
$ErMnO_3$	0.16	3.64	-18.01	0.09	1.06	5.56	-23.26	0.02
$LuMnO_3$	-1.09	4.41	-17.47	0.11	0.31	6.54	-19.77	0.05

not change V_{zz} at the Cd site either way. The test with $HoMnO_3$ showed that indeed rare-earth and oxygen sites changes in EFG are small, and at the Cd site a difference of only 5% was found ($0.3\ 10^{21} \times V/m^2$). Therefore, even tough the exact values of the constituent atoms in the rare-earth manganites are sensitive to changes in the magnetic order and on-site corrections, we concluded that for substitutional Cd simple simulations with the GGA-PBE approximation and ferromagnetic order should suffice to give qualitatively correct values.

The EFG at Cd in the two rare-earth sites follows the same trend found in the rare-earth sites for the pure manganites, with V_{zz} at R1 being always lower than V_{zz} at R2. The asymmetry parameter at the rare-earth sites is zero due to the hexagonal structure symmetry, but not at the Mn site (presented in the table). Nevertheless, η(Mn) is small. No particular trend is found for the Cd sites with respect to the atomic numbers or radius of the different manganites. The differences between the values obtained with unrelaxed and relaxed structures are higher than those found in the pure structures, as expected, since the Cd impurity should introduce other changes. The differences are larger at the Mn site. consistent with the fact that Cd has ionic radius about two times larger than the Mn one, which leads to additionals distortion in MnO_5 surrounding bipyramid.

The complementary PAC experimental work has been performed by T.M. Mendonça et al., and initial PAC experimental results, with ^{111m}Cd→^{111}Cd in $YMnO_3$, confirming part of these calculations, are already published [14].

Chapter 4

Manganese pnictides

Introduction

This chapter, except for this introduction and the appendix, is the exact reproduction of a published article [4] on the topic of manganese pnictide systems, the manganese arsenide (MnAs) in particular. Results obtained at low temperatures in MnAs which were not yet published are shown in the appendix.

The MnAs compound is ferromagnetic at low temperatures with a NiAs-type structure. This structure, shown in figure 4.1 (left), with space group $P6_3mmc$ (194) , has Mn and As atoms at coordinates (0,0,0) and (1/3, 2/3, 1/4), respectively, with two formula units per unit cell. On heating, at $\sim$ 40 C, it undergoes a first-order phase transition, with a discontinuous distortion to the orthorhombic MnP-type structure, in the *Pnma* space group, with four formula units per unit cell. This structure is shown in figure 4.1 (right). The orthorhombic distortion continuously disappears when heating until a second-order phase transition back to the NiAs-type structure at $\sim$ 125 C.

The low temperature hexagonal phase is ferromagnetic, while the high-temperatures is a Curie-Weiss paramagnetic. The intermediate phase, however, considered paramagnetic, does not follow a Curie-Weiss law. The magnetization and inverse magnetic susceptibility are shown schematically in figure 4.2.

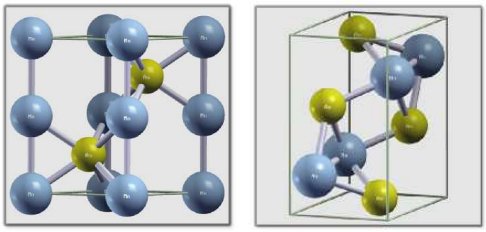

Figure 4.1: Left: Hexagonal NiAs-type structure of MnAs. Right: Orthorombic MnP-type structure of MnAs. The blue and yellow spheres represent Mn and As atoms, respectively.

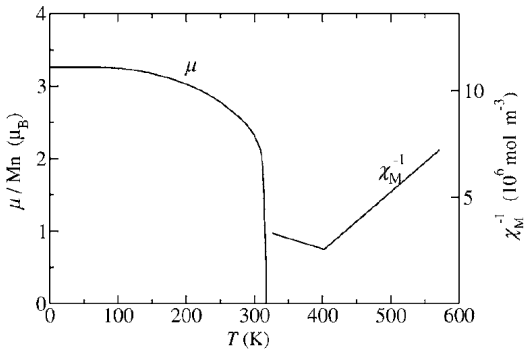

Figure 4.2: Left: Magnetization and inverse susceptibility in MnAs as a function of temperature (taken from [89]).

Abstract

The MnAs compound shows a first-order transition at $T_C \approx 42$ C, and a second-order transition at $T_t \approx 120$ C. The first-order transition, with structural (hexagonal-orthorhombic), magnetic (FM-PM) and electrical conductivity changes, is associated to magnetocaloric, magnetoelastic, and magnetoresistance effects. We report a study in a large temperature range from -196 up to 140 C, using the $\gamma - \gamma$ perturbed angular correlations method with the radioactive probe ^{77}Br$\rightarrow^{77}$Se, produced at the ISOLDE-CERN facility. The electric field gradients and magnetic hyperfine fields are determined across the first- and second-order phase transitions encompassing the pure and mixed phase regimes in cooling and heating cycles. The temperature irreversibility of the 1st order phase transition is seen locally, at the nanoscopic scale sensitivity of the hyperfine field, by its hysteresis, detailing and complementing information obtained with macroscopic measurements (magnetization and X-ray powder diffraction). To interpret the results, hyperfine parameters were obtained with first-principles spin-polarized density functional calculations using the generalized gradient approximation with the full potential (L)APW+lo method (WIEN2K code) by considering the Se probe at both Mn and As sites. A clear assignment of the probe location at the As site is made and complemented with the calculated densities of states and local magnetic moments. We model electronic and magnetic properties of the chemically similar MnSb and MnBi compounds, complementing previous calculations.

Hyperfine interactions in MnAs studied by perturbed angular correlations of γ-rays using the probe $Br^{77} \rightarrow Se^{77}$ and first-principles calculations for MnAs and other Mn pnictides

J. N. Gonçalves* and V. S. Amaral
Departmento de Física and CICECO, Universidade de Aveiro, P-3810-193 Aveiro, Portugal

J. G. Correia
Instituto Tecnológico e Nuclear, UFA, P-2686-953 Sacavém, Portugal

A. M. L. Lopes
Centro de Física Nuclear da Universidade de Lisboa, P-1649-003 Lisboa, Portugal
(Received 19 August 2010; revised manuscript received 22 November 2010; published 29 March 2011)

The MnAs compound shows a first-order transition at $T_C \approx 42\,^{\circ}$C, and a second-order transition at $T_t \approx 120\,^{\circ}$C. The first-order transition, with structural (hexagonal-orthorhombic), magnetic (FM-PM), and electrical conductivity changes is associated to magnetocaloric, magnetoelastic, and magnetoresistance effects. We report a study in a large temperature range from $-196\,^{\circ}$ up to $140\,^{\circ}$C, using the γ-γ perturbed angular correlations method with the radioactive probe ^{77}Br $\rightarrow$ ^{77}Se, produced at the On-Line Isotope Mass Separator (ISOLDE)-CERN facility. The electric field gradients and magnetic hyperfine fields are determined across the first- and second-order phase transitions encompassing the pure and mixed phase regimes in cooling and heating cycles. The temperature irreversibility of the first-order phase transition is seen locally at the nanoscopic scale sensitivity of the hyperfine field, by its hysteresis, detailing and complementing information obtained with macroscopic measurements (magnetization and X-ray powder diffraction). To interpret the results hyperfine parameters were obtained with first-principles spin-polarized density functional calculations using the generalized gradient approximation with the full potential (linear) augmented plane wave plus local orbitals method (WIEN2K code) by considering the Se probe at both Mn and As sites. A clear assignment of the probe location at the As site is made and complemented with the calculated densities of states and local magnetic moments. We model electronic and magnetic properties of the chemically similar MnSb and MnBi compounds, complementing previous calculations.

DOI: 10.1103/PhysRevB.83.104421 PACS number(s): 31.30.Gs, 71.15.Mb, 75.50.Cc, 76.80.+y

4.1 Introduction

The magnetic compound MnAs has been intensively studied, since it exhibits a magnetocaloric effect [90], under hydrostatic pressure [91], as well as when doped with metals [90, 92], making it an interesting material for magnetic refrigeration applications. Moreover, it can be grown as epitaxial films on Si and GaAs substrates [93], where applications such as a source for spin injection make it of promising use for spintronics [94].

In parallel, it is a material with theoretical challenges. In this front some first-principles studies are directed to this compound, e. g. see refs. [95, 89, 96, 97, 98]. The orthorhombic phase is usually considered paramagnetic, however it does not follow a Curie-Weiss law and it has also been considered to be antiferromagnetic [96]. Also of interest is the existing magnetoresistance effect which is attempted to be related to the CMR found in the perovskite manganites [99], and a remarkable spin-phonon coupling found crucial to the magnetostructural transition [98]. Its particular coupling of magnetism and structure has been the origin of macroscopic models [100] for magneto-volume effects.

At low temperatures, MnAs is ferromagnetic and it has a NiAs-type structure. This structure, with space group $P6_3mmc$ (194), has Mn and As atoms at coordinates (0,0,0) and (1/3, 2/3, 1/4), respectively, with two formula units per unit cell. On heating, at about 40 C, it undergoes a first-order phase transition, with a discontinuous distortion to the orthorhombic MnP-type structure, with a parallel discontinuous change of volume, loss of ferromagnetism, and a metal-insulator transition. The orthorhombic distortion continuously disappears when heating until about 125 C where it undergoes a second-order phase transition to the NiAs-type structure with a paramagnetic state, now following a Curie-Weiss law.

Thermal hysteresis is measured in this transition: on heating, the hexagonal→orthorhombic phase transformation occurs at temperatures $T_{C,i} \approx 40.5-42.5$ C, while on cooling this transformation occurs at $T_{C,d} \approx 33.9-37.9$ C [101, 102, 103, 104, 105] (variations in different studies are probably resulting from small differences in the stoichiometry of samples). Phase coexistence in a temperature interval of approximately 2 C is reported by neutron and X-ray diffraction measurements [99, 106]. The orthorhombic $B31$ structure, with the space group $Pnma(62)$, has coordinates for Mn and As atoms of (0.995, 1/4, 0.223) and (0.275, 1/4, 0.918), respectively [103].

The lattice constants of the hexagonal phase at room temperature are $a = 3.722$, $c = 5.702$ Å, and changes to $a = 5.72$, $b = 3.676$ and $c = 6.379$ Å in the orthorhombic phase (with four f. u. per unit cell) at the first-order transition correspond to a volume loss of 2%.

We report a study in this compound using $\gamma-\gamma$ time differential Perturbed Angular Correlation (PAC) spectroscopy (see e. g. [22] for details), to our knowledge the first use of this nuclear technique in the compound. Since PAC measures the combined hyperfine interactions - magnetic hyperfine field (MHF), and electric field gradient (EFG), the sensitivity of its atomic-scale measurements allows the study of the atomic environments as a function of temperature.

Other hyperfine interactions techniques have been used for the study of MnAs and related compounds in previous studies. Using Mössbauer spectroscopy with the ^{57}Fe probe at 0.25 at% concentration, Kirchschlager et al. [107] detect a quadrupole splitting, which they interpret on the basis of motion of the probe atoms, but they do not measure magnetic hyperfine field. Also using ^{57}Fe impurities as probes, in the related $MnAs_{1-x}Fe_x$ compound [108], with $x = 0.01$, 0.03, and 0.15, Abdelgadir et al. reported measurements involving the first-order transition at $T_{C,d} = 2$ C (for $x = 0.01$), where they also detect an unusual dependence of the magnetic hyperfine field. NMR spectroscopy has also been performed at 4K [109], and in the range from -190 up to 38 C, with double signals from both Mn and As atoms, where a resonance anomaly was observed at ≈ -50 C as due from atoms at the domain walls [110].

Our work studies a temperature range from 13 to 140 C and liquid nitrogen temperature (-196 C). Measurements are made in the first-order phase-transition region and above, passing the second-order phase transition (section 4.2.2). The temperature range near the first-order transition is studied in more detail (section 4.2.3). X-Raw powder diffraction and magnetization measurements are also performed and its results are compared with PAC results.

The experimental results are complemented with density functional theory calculations of the hyperfine parameters, using the full potential mixed (linear) augmented plane wave plus local orbitals (L)APW+lo method. In order to improve and complement other first-principles studies, we also show calculations of other properties, and for the chemically similar manganese pnictides MnSb and MnBi.

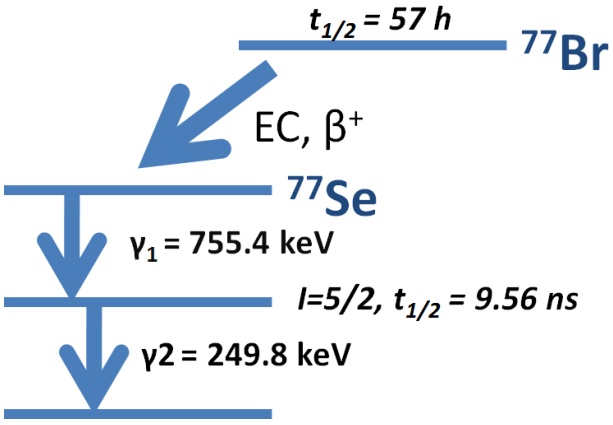

Figure 4.3: Diagram of the $\gamma - \gamma$ decay cascade of ^{77}Se, with the properties of the relevant intermediate isotope, and of the decay from the parent isotope ^{77}Br by processes of electron capture and positron emission.

4.2 Experiments

4.2.1 Experimental details and sample preparation

A mixture of radioactive isobars of mass 77, ^{77}Kr, ^{77}Br and ^{77}Se were produced at the ISOLDE isotope separator online facility at CERN, and implanted at 30 keV to a dose of approximately 10^{16} atoms/m^2 in MnAs samples at room temperature. After waiting for the decay of ^{77}Kr ($t_{1/2} \approx 74$ min) for 12 h, the PAC experiments have started on the decay of ^{77}Br to ^{77}Se, after annealing, as described.

One test sample was measured as implanted, but the resulting spectrum was highly attenuated due to implantation defects. Subsequently, a first annealing step at 600 C for 200 s was done in vacuum (5×10^{-4} mbar), followed by a fast quench to room temperature for both samples, after which the spectra substantially improved.

The $\gamma - \gamma$ cascade of ^{77}Br$\rightarrow^{77}$Se is shown in figure 4.3. The hyperfine interaction is measured in the 9.56 ns, 249.8 keV, $I = 5/2$ intermediate state of the cascade, with quadrupole moment $Q = 1.1(5)b$, and magnetic moment $\mu = 1.12(3)\mu_N$ [24].

The directional correlation of the decays is perturbed by the hyperfine interactions and the experimental anisotropy ratio function $R(t)$, which contains all of the relevant information, is expressed as a function of time, t. $R(t) = \sum A_{kk} G_{kk}(t)$, where A_{kk} are the anisotropy coefficients, depending on the spin and multipolarity of the γ decays, and $G_{kk}(t)$ contains the information of the hyperfine parameters. Due to the solid angle attenuation of the detection system the anisotropy is reduced, and the effective experimental anisotropy was found to be $A_{22} \approx -0.13(1)$. The long half-life of the parent isotope ^{77}Br, 57 h, and the relatively short half-life of the intermediate state, allowed us to perform several measurements with a very good true to chance coincidence ratio from a single implantation shot.

The PAC-spectrometer, a high efficiency setup of six BaF_2 detectors, provides 30 coincidence spectra (6 from 180° and 24 from 90° between detectors [20]).

4.2.2 1st set of PAC experiments

The obtained PAC experimental functions $R(t)$ and the respective Fourier analysis are shown in figures 4.4 and 4.5.

The spectra were fitted using a numerical algorithm that calculates the hamiltonian of the interaction to obtain the magnetic B_{hf} and quadrupole EFG parameters [23]. Figs. 4.4 and 4.5 also show the Fourier analysis of the $R(t)$ functions for all temperatures measured.

Table 4.1 shows all fit parameters obtained at the different temperatures, in the chronological order of measurements. Between the last two measurements, the sample was heated to 100 C, so the 35 C measurement is made on cooling.

The fit procedure can consider several fractions of ^{77}Se nuclei interacting with different hyperfine fields due to different local environments. For the ferromagnetic case the fits mainly reveal nuclei interacting with a magnetic field. Additionally for all phases, a fraction must be considered of ^{77}Se nuclei interacting with a strong (EFG_3) distribution, that we attribute to nuclei on defect regions of MnAs which could not be annealed. This fraction was firstly allowed to vary, but the quality of the fit is not very sensitive to its value. In the final fits we constrained this value to the average of all previously found values, $f_3 = 22\%$.

Upon the transition the magnetic interaction vanishes and a slow frequency, due to the orthorhombic phase EFG is revealed. The limited time window and low quadrupole moment makes it difficult to measure the EFG_2 parameters of the orthorhombic phase with high precision. Even in the most accurate measurements it can be fitted reasonably in a large range. On the other hand, the stronger EFG_3 of $f_3 = 22\%$ has a large damping which also makes its accurate determination difficult. Therefore, in the present experiments, the asymmetry parameters η_2, η_3 were set to zero, since large variations produce small changes in the results. On the other hand, this procedure agrees with the fact that the hexagonal and weakly distorted orthorhombic symmetries produce very small axial asymmetry parameters. The frequency ω_{02} was also fixed in an average value.

The magnetic phase, characterized by a well defined magnetic hyperfine field, could be characterized also by a very small EFG. The fit program properly handles this problem by resolving the Hamiltonian for the combined interaction. In the results we present only a pure magnetic interaction, since with a combined interaction the EFG (V_{zz}) would have to be very small in this phase and cannot be properly disentangled within the short analysis time of 45 ns. We estimate a majorant for $V_{zz} \lesssim 1 \times 10^{21} V/\mathrm{m}^2$, above which the quality of the fit would significantly degrade.

The obtained V_{zz} attributed to the orthorhombic phase is less than $1.1 \times 10^{21} V/\mathrm{m}^2$ at all temperatures measured.

The frequencies ω and Lorentzian widths σ are similar for the whole temperature range in this phase. However, we point that before the experiment performed at 141 C during six hours, EFG_2 shows a relevant attenuation of $\sigma_2 \approx 300$ Mrads^{-1}. After this measurement the attenuation was considerably reduced and the characteristic EFG_3 parameters attributed to Se interacting with defects of MnAs have considerably changed. Both modifications compare

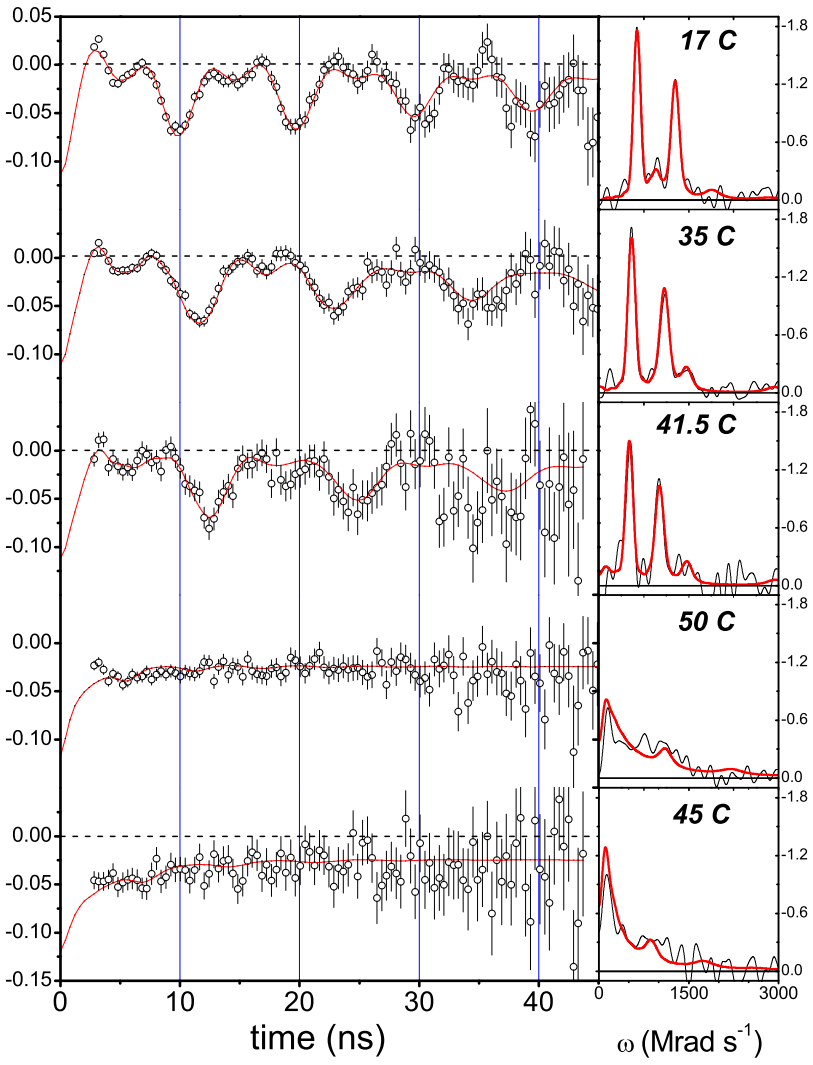

Figure 4.4: (Color online) PAC spectra and Fourier Transforms of the first five measurents, in chronological order. The fits are represented by the red lines.

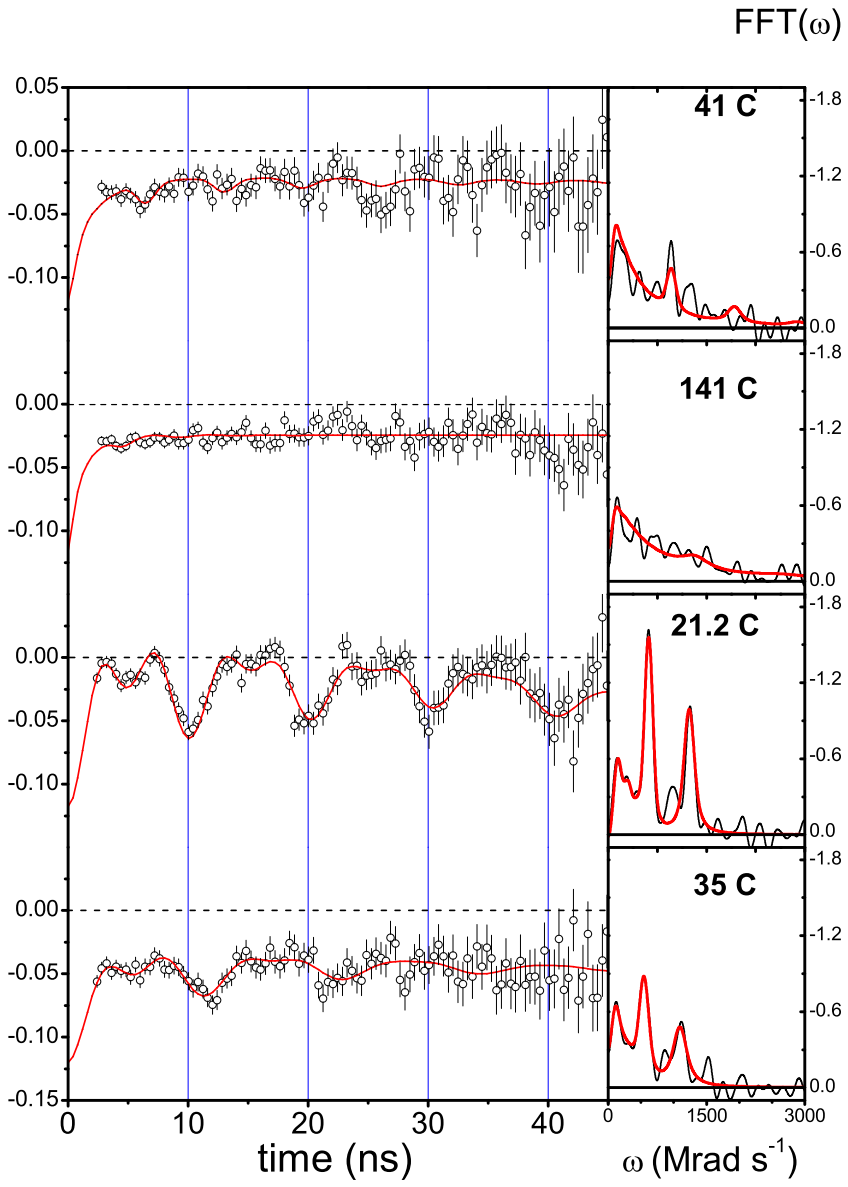

Figure 4.5: (Color online) PAC spectra and Fourier Transforms of the last five measurents, in chronological order. Between 21.2 and 35 C the sample was heated to 100 C, so that the 35 C measurement is made on cooling. The fits are represented by the red lines.

Table 4.1: Fit parameters, from measurements when heating and cooling the 1st sample, in chronological order. Fraction (%) of the measured interactions, quadrupolar frequency (ω_0) (Mrad.s^{-1}), Larmor frequency ω_L (Mrad.s^{-1}) and width of Lorentzian function used in the fitting procedure (σ) (Mrad.s^{-1}). The magnetic frequencies have an estimated upper limit for the error of 15 Mrad.s^{-1}. The fraction f_3 and the frequency of the orthorhombic phase were kept fixed at an average value. H = hexagonal ferromagnetic, O = orthorhombic, H* = hexagonal paramagnetic.

T(°C)	f_1	ω_{L1}	σ_1	f_2	ω_{02}	σ_2	f_3	ω_{03}	σ_3	Phase
17	78	637	21	-	-	-	22	945	69	
35	78	547	28	-	-	-	22	1466	69	H
41.5	78	506	33	-	-	-	22	1484	55	
50	-	-	-	78	29	290	22	1108	10	
45	-	-	-	78	29	330	22	874	96	O
41	-	-	-	78	29	290	22	963	46	
141	-	-	-	78	29	435	22	1324	17	H*
21.2	78	618	33	-	-	-	22	176	40	H
35	60	546	65	18	28	31	22	176	43	H+O

well with what is observed in the second set of PAC experiments immediately after the 600 C annealing step. We think this is evidence for an incomplete annealing that was compensated during the lenghty six hours measurement at 141 C.

The EFG parameters measured at 141 C, above the second-order phase transition, shows a very low V_{zz} as expected from the NiAs-type structure, and there is no hyperfine field since the sample should be paramagnetic, following a Curie-Weiss law at this temperature.

The measurement at 35 C shows a lower amplitude of the R(t) function due to the coexistence of hexagonal and orthorhombic phases. Still, there is a stronger attenuation of the magnetic field that can correlate with the dynamics of the phase coexistence.

The first-order transition reported in the literature when heating is clearly seen in the PAC spectra at approximately 42 C with the disappearing magnetic hyperfine field when measuring at 50 C.

The fact that the spectrum measured at 41.5 C (when raising T, fig. 4.4) and the spectrum measured at 41 C (when lowering T, fig. 4.5) are markedly different, shows that the hysteretic behavior of the macroscopic magnetization usually measured is also present at the microscopic-local like hyperfine field.

4.2.3 2nd set of PAC experiments - First-Order Transition

A detailed study of the first-order transition has been done according the following order, on a second sample: 21.1, 40.8, 41.3,, 43.5, 124.5 (raising temperature); 41.4, 39.5, 37.5, 36.6, 33.3, 32.5, 29.9, 13.3, -196 C (lowering temperature).

The first five PAC measurements, done when heating the sample, from room temperature, to above the first-order transition, are shown in figure 4.6.

The five measurements, done when cooling the sample, from 36.6 to 13.3 C, also passing the

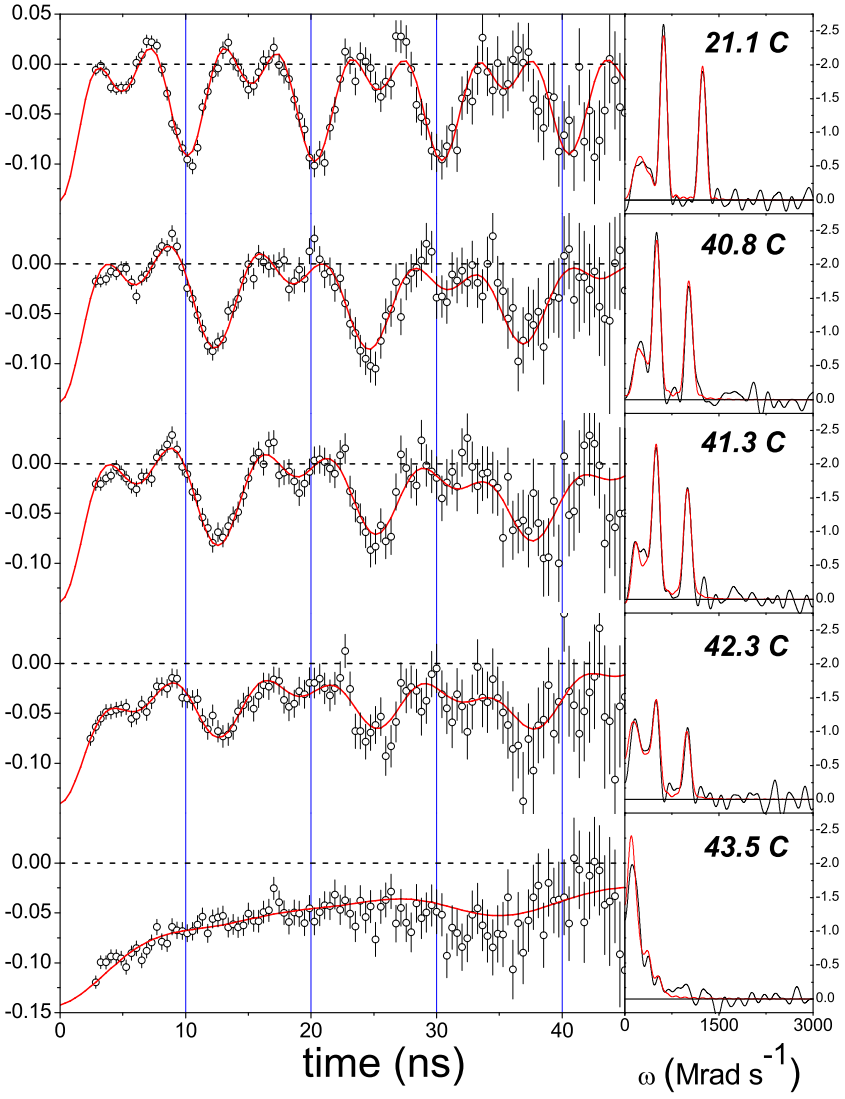

Figure 4.6: (Color online) PAC spectra and Fourier Transforms. Measurements made when heating the sample. The fits are represented by the red lines.

transition, are shown in figure 4.7.

The measurements done when cooling the sample above the phase transition (41.1, 39.5, 37.5, 36.5 C), coming from a high temperature (124.5 C), are not included, since those spectra are similar to the first spectrum in figure 4.7, at 36.6 C.

A last measurement performed with the sample at liquid nitrogen temperature is shown in figure 4.8.

In a similar way to the preceding section, the fits were done considering a magnetic hyperfine field and low EFG, which are characteristic of each phase. For the reasons already detailed the asymmetry parameter is set to zero for all EFGs, and the fraction attributed to defect and orthorhombic frequencies are fixed in average values. Also, an additional EFG characterized by a quadrupole interaction of $\omega_0 \approx 176$ Mrad.s^{-1}, $V_{zz} \approx 6.4 \times 10^{21}$ V/m^2, is found that accounts for 30% of the probe nuclei in perturbed environments of the sample, still remaining

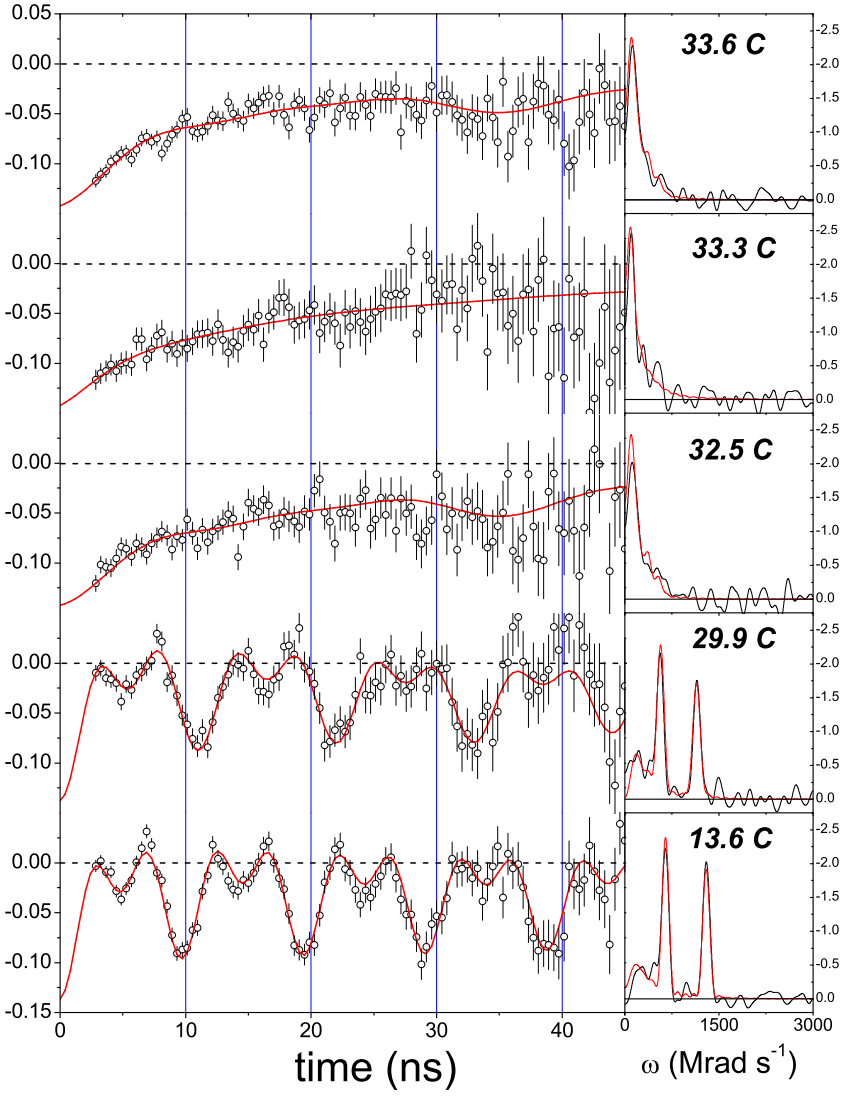

Figure 4.7: (Color online) PAC spectra and Fourier Transforms. Measurements made when cooling the sample. The fits are represented by the red lines.

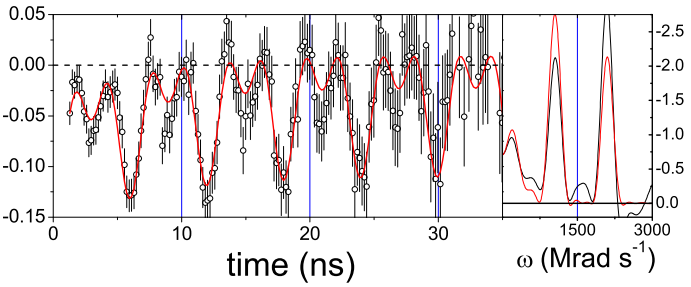

Figure 4.8: (Color online) PAC spectra and Fourier Transforms at -196 C. The fits are represented by the red lines.

Table 4.2: Fit parameters, with temperatures in chronological order, for the 2nd sample. Fraction (%) of the measured interactions, quadrupolar frequency ω_0 (Mrad.s^{-1}), Larmor frequency ω_L (Mrad.s^{-1}), and width of Lorentzian function used in the fitting procedure σ (Mrad.s^{-1}). The magnetic frequencies have an estimated upper limit for the error of 15 Mrad.s^{-1}. f_3 and corresponding frequency were fixed at an average value, as was ω_{02}. H = hexagonal ferromagnetic, O = orthorhombic.

T(°C)	f_1	ω_{L1}	σ_1	f_2	ω_{02}	σ_2	f_3	ω_{03}	σ_3	
21.1	70	619	3	-	-	-	30	176	23	
40.8	70	510	9	-	-	-	30	176	22	H
41.3	70	499	12	-	-	-	30	176	18	
42.3	40	495	10	30	28	20	30	176	10	H+O
43.5	-	-	-	70	28	24	30	176	9	
124.5	-	-	-	70	28	26	30	176	27	
41.4	-	-	-	70	28	36	30	176	17	
39.5	-	-	-	70	28	46	30	176	24	O
37.5	-	-	-	70	28	47	30	176	22	
34.5	-	-	-	70	28	29	30	176	14	
33.3	-	-	-	70	28	197	30	176	73	
32.5	-	-	-	70	28	20	30	176	11	
29.9	70	571	9	-	-	-	30	176	48	
13.6	70	648	4	-	-	-	30	176	98	H
-196	70	1050	0	-	-	-	30	57	29	

after annealing.

The values of all fitted parameters can be found in table 4.2.

As can be seen by the changes in the spectra, the transformations occur near $T_{C,i} \approx 42.3 - 43.5C$ and $T_{C,d} = 30 - 32.6$ C. Therefore we estimate the thermal irreversibility to be between 10-13.5 C. This hysteresis is somewhat larger than that reported in other works by X-ray and magnetization measurements (10 C) [101, 102, 103, 104, 105].

Figure 4.9 shows magnetization measurements on the same samples with a vibrating sample magnetometer with $B = 0.01$ T, showing $T_{C,i} = 45$ C and $T_{C,d} = 30.7$ C. The abrupt change over 2 C, at ≈ 44 C, when heating (see fig. 4.9), is in agreement with the hyperfine field changes measured above 43.5 C.

As in the first set of PAC measurements, there is a hyperfine field of 24 T just before the transition. Then the magnetic phase disappears in a small temperature interval, as shown in the spectra of figure 4.6 at 42.3 and 43.5 C. This shows no continuous decrease of the hyperfine field to zero before the transition. Note that this conclusion cannot be learned from macroscopic magnetization measurements only (see figure 4.9), where the magnetization can be seen to decrease to zero, since just before the ferromagnetic to paramagnetic phase transition and within the temperature difference of 1 C, only a very small variation of the hyperfine field is observed. This clearly shows that the magnetization changes are mainly the result of changes in phase fractions, instead of thermal disorder.

Figure 4.10 shows the hyperfine fields obtained, where the agreement for both experiments can clearly be seen.

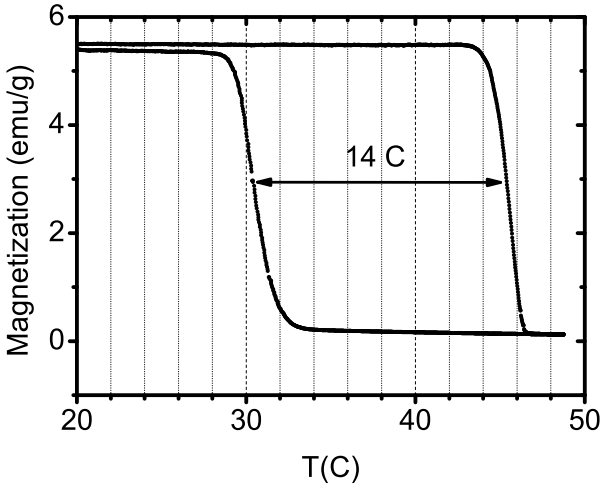

Figure 4.9: Temperature dependence of the magnetization, measured at $B = 0.01$ T, signalling the strong thermal hysteresis at the 1st order transition.

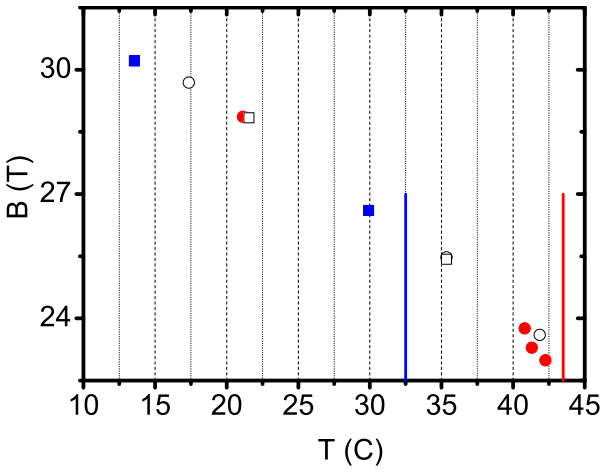

Figure 4.10: (Color online) Hyperfine field of the main fraction vs. temperatures, excluding the value at -196 C. Circles for measurements when heating, squares for cooling. The open symbols show the results of the first experiment, for comparison. The lines are the first (when heating) and last (when cooling) measurements at the orthorhombic phase.

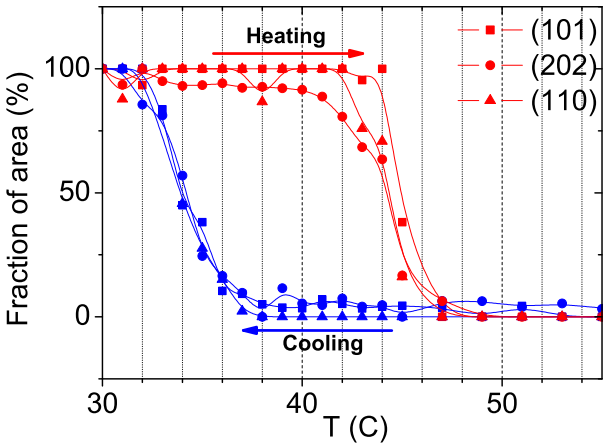

Figure 4.11: (Color online) XRD Fractions of the total area corresponding to the peaks of the hexagonal phase, at three 2θ intervals.

Notice that the attenuation of the hyperfine fields in the ferromagnetic phase increases towards the phase transition temperature. When cooling from high temperature the same behavior is observed and at liquid nitrogen temperature (- 196 C), no attenuation is observed. These observations hint at dynamic processes due to spin fluctuations.

At 42 C the amplitude of the magnetic part of the R(t) functions is smaller than at lower temperatures, showing a reduced fraction of the ferromagnetic phase still present. A fraction of 60% for the ^{77}Se atoms at the ferromagnetic phase while other 10% show a small quadrupole frequency. This third fraction has $V_{zz} = 1.08$ (η was fixed to zero), corresponding to the value found for the other fits in the orthorhombic phase. We can say that the phase coexistence only occurs in a width of 2.2 C or less, since the measurement below and at (41.3 C) and above and at (43.5 C) show only the ferromagnetic and paramagnetic phases, respectively. This width is in agreement with previous measurements of approximately 2 C [99, 106].

The 1st order structure transformation was also probed with temperature dependent X-ray powder diffraction studies in a Philips diffractometer. We performed detailed measurements as a function of temperature, in three selected diffraction angle regions, were changes in the transition are easily seen. Three 2θ intervals were selected, 31.4-32.6, 41.8-43.1, and 48.6-50 degrees, where one peak characteristic of the hexagonal phase disappears in the transition with the appearence of peaks characteristic of the orthorhombic phase. In the 31.4-32.6 2θ interval the (101) peak disappears with the appeareance of (102) and (111) peaks almost at the same angle. The same situations occur when the (102) peak disappears and (202), (211) peaks appears in the orthorhombic phase for 41.8-43.1 degrees. For 48.6-50 degrees, the (110) hexagonal peak transforms into (013), (020), (212) and (301) peaks in the orthorhombic phase. The fit of the peaks was done simply with gaussian functions, one gaussian for the hexagonal peak and another gaussian for the two or more highly overlapped orthorhombic peaks. The areas of each peak should correspond approximately to the fraction of each phase.

Figure 4.11 shows the fraction of the hexagonal phase obtained this way for the 3 angular intervals. The hysteresis produces here a difference of approximately 12 C. Magnetization

measurements show a somewhat higher thermal hysteresis difference at half height, 14 C, which might indicate that the magnetic coupling is disturbed before the hysteresis is completed. The thermal hysteresis interval obtained from PAC has a large uncertainty (10-13.5 C) but is in agreement with both measurements.

4.3 First-principles calculations

Knowing the lattice location of the PAC probe is of fundamental importance to understand the values obtained. After the decay of ^{77}Br, it is expected that the ^{77}Se PAC probe may be substitutional at the As site, since As has a similar atomic radius and a neighbor atomic number. In order to check this assumption and to see the differences in the hyperfine parameters actually measured at the probe site, we have used ab-initio density functional calculations.

Despite the existence of some published works reporting ab-initio simulations in this system, the hyperfine parameters are usually not reported. The work of Ravindran et al. [97], presents the calculation of the hyperfine parameters and magneto-optical properties, using density functional calculations, of three manganese pnictides MnX (with X=As, Sb and Bi). Their calculations used the FLAPW method and the electric field gradient and magnetic hyperfine field were presented. However, as suggested by A. Svane [111], the calculated structures of [97] are incorrect, since the positions of Mn and the pnictide were exchanged with respect to the the stable NiAs-type structure. Recently, calculations of the hyperfine parameters in bulk and surfaces of MnAs were also reported, and the correct values were obtained [112].

Here we also calculate the hyperfine parameters with the similar full potential (L)APW+lo method, as implemented in the WIEN2K code [17]. In this method the space is divided in spheres, centered at the atoms, where the valence states are described by atomic-like functions, and the interstitial space, where plane waves are used.

The Mn and As atomic spheres used have both a radius of 2.5 a.u. . We checked convergency of the hyperfine parameters and total energy as a function of the number of k-points used for integration in the Brillouin zone and the number of plane waves in the basis. The calculations are spin-polarized and consider a ferromagnetic arrangement of Mn moments. For the calculations of hyperfine parameters, spin-orbit coupling is included, for the other properties no spin-orbit coupling is included, with a scalar-relativistic basis for the valence electrons, while for the core electrons the treatment is always fully-relativistic. For Mn core states are 1s, 2s, 2p, and 3s, and valence states are 3p, 3d, and 4s, while for As 1s, 2s, 2p, 3s, and 3p are core states and 3d, 4s, and 4p are valence states. The PBE Generalized Gradient Approximation [43] exchange-correlation functional is used, since the LSDA is known to give poor results in this compound [113].

The calculated EFG of the MnAs sites in the hexagonal phase is shown in the table 4.3. Due to the hexagonal symmetry η is zero, and the direction of the principal axis of the EFG tensor is parallel to the c-axis. The EFG inside the spheres, which is almost equal to the total EFG, can be separated in different contributions, since the the states are described in combinations of spherical harmonics, with different angular momentum components. In this case the p-p and d-d contributions of the density are the dominant terms, with $V_{zz}^{pp} \propto \langle 1/r^3 \rangle_p [1/2(p_x + p_y) - p_z]$

Table 4.3: Calculated electric field gradient of MnAs, at the hexagonal phase, with room temperature lattice constants: a=3.722 Å, c=5.702 Å.

Atom	$V_{zz}(10^{21}V/m^2)$	η	V_{zz} dir.
Mn	-3.63	0	(0,0,1)
As	1.53	0	(0,0,1)

Table 4.4: Calculated hyperfine Fields of MnAs (T): room temperature lattice constants: a=3.722 Å, c=5.702 Å, hexagonal phase.

Atom	B_C	core	valence	B_{orb}	B_{dip}
Mn	-6.5	-39.3	32.8	0.5	-3.0
As	25.0	0.4	24.5	-0.1	-0.2

and $V_{zz}^{dd} \propto \langle 1/r^3 \rangle_d [(d_{xy} + d_{x^2-y^2}) - 1/2(d_{xz} + d_{yz}) - d_{z^2}]$. For Mn, $V_{zz}^{pp} = -1.45$ and $V_{zz}^{dd} = -1.70$ $\times 10^{21} V/m^2$, states with both p and d character contribute to the total EFG. For the As atoms, the states of p character are the dominant contribution with $V_{zz}^{pp} = 1.27$ and $V_{zz}^{dd} = 0.06 \times 10^{21}$ V/m^2. Cutting the $3d^{10}$ states out of the density calculation the V_{zz} at As remains almost the same, confirming that the contribution from the As filled d electrons is negligible.

In order to improve the results of the previously mentioned work, we also calculated the EFG at MnSb and MnBi. We discuss them in section 4, along with other quantities.

The Fermi contact hyperfine field at the nucleus is calculated, with the electron density averaged at a sphere with the Thomson radius, $r_T = Ze^2/mc^2$, according to the formulation of Blügel et al. [26] in which $\overrightarrow{B}_C = \frac{8\pi}{3}\mu_B \overrightarrow{m}_{av}$, i. e. the contact hyperfine field is parallel to the average spin density. The contributions of the contact hyperfine field due to core and valence electron density contributions are discriminated in the tables. We remark the fact that while in As the hyperfine field is determined almost exclusively by its valence contribution, caused by the polarization by Mn atoms, the core and valence contributions of Mn cancel in a large amount. This is due to the core polarization mechanism [26], where the core hyperfine field in Mn has a negative sign due to the polarization of core s electrons by the d shell: the majority electrons are attracted to the polarizing d electrons while the minority electrons are repelled, resulting in an excess minority charge at the nucleus. The on-site orbital and spin dipolar contributions are also calculated. These contributions are small when compared with the contact hyperfine field. In order to see the change due to different lattice parameters in the hyperfine fields, we calculated also with the low temperature lattice constants [114] and the obtained values are almost equal (tables 4.4 and 4.5). This simply shows that the collinear spin density functional theory calculations cannot reproduce temperature related changes based only on the lattice constants.

The previously obtained hyperfine parameters are in reasonable agreement with the GGA calculations of Jamal et al. [112]. Some differences are expected, since while their calculations consider the full theoretical lattice optimization, we only minimized the atomic forces keeping the lattice parameters fixed at the experimental values. Relative to their results, for the V_{zz} at Mn and As, small differences of 5% (1.53 against 1.46) and 4% (-3.63 against -3.78) are obtained,

Table 4.5: Calculated contact hyperfine field of MnAs (T): low temperature lattice constants: a=3.732 Å, c=5.678 Å, hexagonal phase.

Atom	B_C	core	valence
Mn	-6.1	-38.7	32.5
As	25.5	0.4	35.1

Se at As site					
$V_{zz}(10^{21}V/m^2)$	η	V_{zz} dir.			
-0.27	0	(0,0,1)			
B_C	core	valence	B_{orb}	B_{dip}	——B_{hf} total (T)
56.6	0.4	56.2	-2.1	-0.2	54.3
Se at Mn site					
$V_{zz}(10^{21}V/m^2)$	η	V_{zz} dir.			
17.80	0	(0,0,1)			
B_C	core	valence	B_{orb}	B_{dip}	—— B_{hf} total (T)
-23.1	-22.9	-0.2	3.4	-1.8	-21.5

Table 4.6: Hyperfine parameters with Se probe substitutional at the As or Mn sites in MnAs.

respectively. For the hyperfine fields the differences are -9 (present work) compared with 1 T at the As site (small absolute difference) , and 24.7 (present work) compared with 31.8 T at the Mn and As sites.

To compare with the PAC results using the implanted probe, the presence of a highly diluted (ppm) Se probe must be accounted for in supercell calculations. The EFG and hyperfine field were calculated for hypothetical situations where the Se is substituted at As and at Mn sites using $Mn_{15/16}Se_{1/16}As$ and $MnSe_{1/16}As_{15/16}$) supercells.

The results for supercells with Se concentration of 1/16 are shown in the table 4.6. The atomic forces were not high, and were minimized by moving the free atomic coordinates. The small changes in this type of system due to the lattice constants (tables 4.4 and 4.5) motivated us to keep using the MnAs room temperature lattice constants. The hyperfine field calculated with the Se atom substitutional at the As or Mn sites would be exact only at 0K (disregarding zero-point effects, which should be small [115]). Our closest measured value is at liquid nitrogen.

There is a good agreement of the measured 49 T at 77K when compared with the calculated 54.3 T at the As site. In contrast, for the case in which Se is substitutional at the Mn site, $|B_{hf}|$ is too low when compared to the experiment, even near the transition, and the very high $V_{zz} = 17.4 \times 10^{21}$ V/m^2 immediately discards the possibility that the probe is located there, whereas the EFG is very small for As-site substitutional Se, in agreement with experiment. The calculation of the formation energies ΔH_f for the two substitutions also indicates this assignment,

$$\Delta H_f = E_{imp}^{sup} - 8 \times E^{MnAs} - \mu_{Se} + \mu_{As/Mn} \tag{4.1}$$

where E_{imp}^{sup} is the total energy of the $2 \times 2 \times 2$ supercell with a Se impurity, E^{MnAs} is the energy calculated for the pure compound, and μ_{Se} is taken as the total energy of nonmagnetic *hcp* Se.

Table 4.7: Electric field gradient of MnAs, MnSb and MnBi, p-p and d-d contributions in the atomic spheres.

Compound	Atom	$V_{zz}(10^{21}V/m^2)$	V_{zz}^{p-p}	V_{zz}^{d-d}
MnAs	Mn	-3.63	-1.45	-1.70
	As	1.53	1.27	0.06
MnSb	Mn	-3.92	-1.40	-1.97
	Sb	4.67	3.97	0.10
MnBi	Mn	-4.43	-1.91	-2.49
	Bi	9.46	9.44	0.21

The chemical potential of As or Mn (according to the substituted site) is set as the energies of fcc antiferromagnetic Mn and nonmagnetic rhombohedral As. The formation energy obtained for substitution at the As site is 0.03 eV, while for the Mn substitution it has a higher value of 2.84 eV, confirming the hyperfine calculation. However, since Br is the implanted atom , if there is no time for relocation between the Br→Se decay and the PAC measurement, the formation energy of Br should be a better indication. Therefore, we also calculate these formation energies, using the energies of supercells of the same size for the same substitutions, with Br, and the energy of nonmagnetic solid Br_2 as μ_{Br}, instead of μ_{Se}, in the previous formula. The obtained results are 0.94 eV for the Br at As substitution, and 3.95 eV at the Mn site, again confirming the As substitution.

4.4 Manganese Pnictides

Full potential calculations of the hyperfine parameters and other properties of manganese pnictides were performed by Ravindran et al. [97], but with the anti-NiAs structure. Here we report the same properties as calculated with the FLAPW method, i. e. the spin magnetic moments, the density of states and the hyperfine parameters, with the NiAs-type structure.

The hyperfine parameters are especially sensitive to the type of structure. For the atoms of Mn and As, in the true structure $V_{zz} = -3.7$ and $1.4 \times 10^{21}V/m^2$, respectively, while in the anti-MnAs structure $V_{zz} = 0.4$ and $11.8 \times 10^{21}V/m^2$.

Table 4.7 shows the EFG of the three manganese pnictides. The asymmetry parameter and V_{zz} direction are omitted, since they are always 0 and (0,0,1). The EFG of the pnictide site increases with increasing atomic number (As, Sb, Bi), which coincidentally also happens in the work of Ravindran et al. [97]. For the EFG of Mn the situation is reversed, in our calculations its absolute value increases, while their results with the inverted structure have a slight decrease ascribed to volume effects, which cannot be true now.

The spin moments for each atom, calculated inside the LAPW spheres, are presented in table 4.8. Experimental values and values obtained from other band-structure calculations are also presented. With our calculation, the values obtained, in μ_N per formula unit, are now in a better agreement with experiment. Similar calculations (references in table 4.8), which have used the NiAs-structure, get values which are in accordance to our results, consistently lower

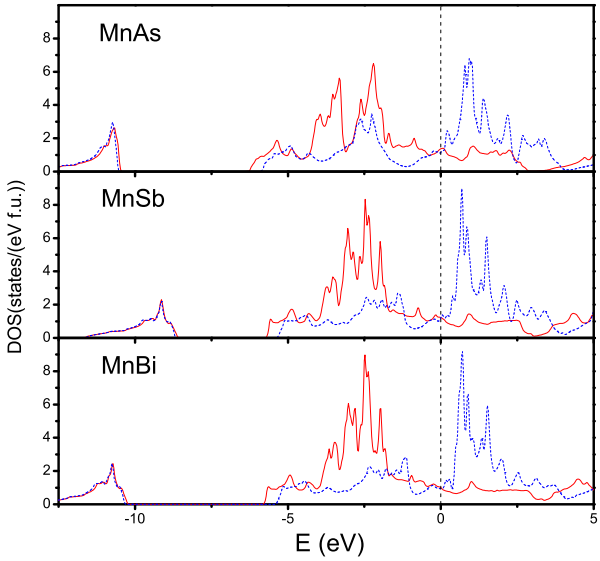

Figure 4.12: (Color online) Total density of states for MnAs, MnSb, and MnBi in units of $states/(eVf.\ u.)$. The up states are represented by the red full line and the down states by the blue dashed line. Energy is in eV, relative to the Fermi energy (dashed line).

than experiment.

The spin projected density of states (DOS) for the three manganese pnictides is shown in figure 4.12, with energy reference equal to the Fermi energy. The band structure has been obtained before for these compounds by several authors. Although the DOS obtained by [97] is different, coincidentally most of the qualitative features apply also. Mainly Mn d and pnictide p states hybridize decreasing the free value $5\mu_B$. In both our study and theirs there are large peaks at the up states, below the Fermi energy, largely due to Mn d states, at approximately -2.5 eV. The Mn d-states for the down spin are shifted to the conduction band. This can be seen in figure 4.13, where the important states of each atom are discriminated in their s, p and d character. The As s states are nearly isolated between 13 and 10.5 eV below the Fermi energy. The total number of states at the Fermi level is 2.51 for MnAs, 2.22 for MnSb, and 1.95 for MnBi. In comparison, with the anti structure the values are higher, respectively 3.46, 2.78, 2.05 [97], which suggests that the structure is not so stable, as expected . The experimental value of 2.4 ± 0.4 states for MnSb estimated from specific heat measurements [116] is also in agreement.

The magnetic hyperfine field increases greatly from MnSb to MnBi, due to the larger polarization from the s electrons at the nuclear position, which largely increases due to the additional s-orbitals of higher principal atomic number, and the fact that Mn in MnBi has the larger magnetic moment, so that it polarizes the Bi valence electrons. The magnetic moment of the pnictogen site is very small, so that the core contribution of the hyperfine field is also small. For MnSb, previous NMR measurements have determined a frequency of 260 MHz at low temperatures, attributed to domain wall edge resonances [129], correspondig to a hyperfine field $B_{hf} = 3.93$ T, equal to our calculated value for the bulk. The hyperfine field has been measured in MnBi, at the Bi atoms by nuclear orientation [130], $B_{hf} = 94$ T, comparing reasonably with

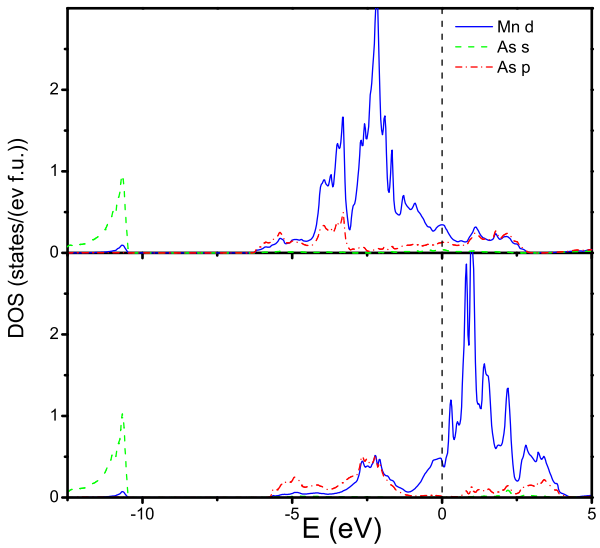

Figure 4.13: (Color online) Density of states of MnAs in the hexagonal phase divided in the most important contributions for the majority (upper figure) and minority (lower figure) states.

Table 4.8: Total magnetic moment for MnX (X=P, As, Sb, Bi) in the cell and magnetic moments inside the Mn and X LAPW spheres, in units of μ_B/formula unit. Previous experiments and calculations are compared with our results.

10^{21}V/m^2 Compound	Mn_s	X_s	MnX_t
MnAs(present work)	3.29	-0.14	3.17
MnAs(exp.)		-0.23 [117]	3.40 [117]
MnAs(theory)			3.10 [118]
	3.14	-0.08	3.06 [119]
	3.18	-0.13	3.14 [112]
MnSb(present work)	3.44	-0.14	3.34
MnSb(exp.)		-0.30 [117]	3.55 [120]; 3.50 [121]
MnSb(theory)	3.34	-0.07	3.27 [118]
	3.35	-0.032	3.32 [122]
	3.30	-0.06	3.24 [123]
	3.5	-0.17	3.31 [124]
MnBi(present work)	3.49	-0.11	3.42
MnBi(exp.)			3.82 [125]; 3.84 [126]; 3.9 [127]
MnBi(theory)	3.71	-0.10	3.61 [119]
	3.50	-0.02	3.56 [128]

Table 4.9: Fermi contact hyperfine Fields of MnAs, MnSb, and MnBi, core and valence contributions, orbital and dipolar hyperfine fields (T).

Atom	B_C	core	valence	B_{orb}	B_{dip}
Mn	-6.5	-39.3	32.8	0.5	-3.0
As	25.0	0.4	24.6	-0.1	-0.2
Mn	-8.5	-41.5	33.0	1.2	-2.8
Sb	30.6	-2.0	30.8	0.1	-0.5
Mn	-5.8	-42.1	36.3	3.6	-2.8
Bi	82.6	-1.2	83.8	0.2	-1.0

our value of 81.8 T.

4.5 Conclusion

We have measured the hyperfine parameters with the perturbed angular correlation method in MnAs. The hysteresis at the hexagonal-orthorhombic 1st order phase transition is clearly seen from a microscopic point of view, complementing the X-ray and magnetization measurements. The hyperfine magnetic field is the same at a given temperature, irrespective of cooling or heating the sample even in the phase coexistence region. This local probe study shows that the magnetization changes observed are mostly due to a change of phase fractions, which can be related to XRD studies. We provide a clear demonstration of the nature of the first-order phase transition, by microscopic observation of phase separation at the hyperfine interactions range (sentitive to approximately less than 10 Å), much shorter than the range of diffraction techniques. We measured phase coexistence in a small interval of temperature (2 C), comparable with previous measurements. In contrast, in other cases, PAC measurements were able to find very small coexistent regions of two competing phases, in a much broader temperature range than that given by x-ray diffraction [65].

Ab-initio calculations are used to complement the experiment. Realistic simulations of the diluted probe with supercell calculations show that the ^{77}Se probe, if substitutional, is located at the As site. This information is taken from the comparison of calculated and measured hyperfine parameters, and it is verified by the calculated formation energies. Our results reproduce the hyperfine field at low temperature with good quantitative agreement.

It may be interesting to try an experiment with a probe of high quadrupole moment, since in this case the EFG is very small and has an overlying high amplitude magnetic hyperfine field, which makes its accurate determination difficult. Improved results for the compounds MnSb and MnBi, of hyperfine parameters, magnetic moments and density of states were also presented and discussed.

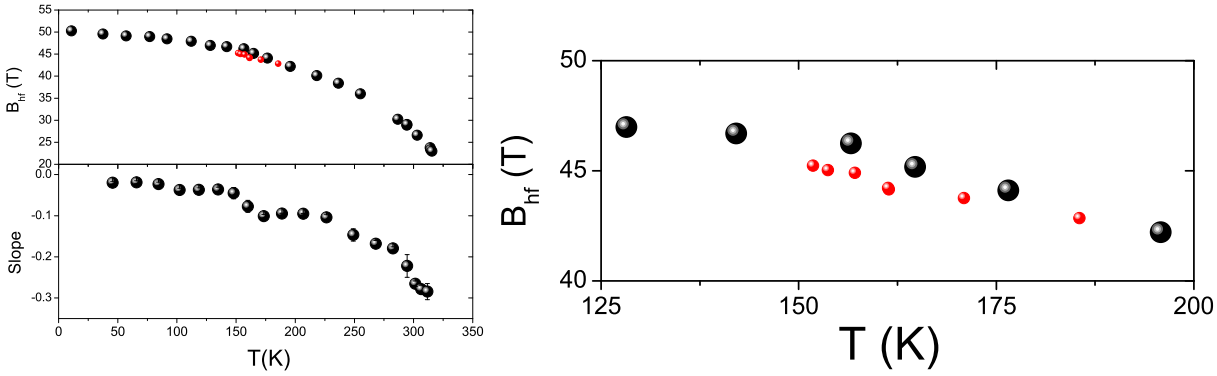

Figure 4.14: Hyperfine field at ^{77}Se in MnAs, in the FM phase. The measurement was made from low temperature and heating. The last measurements are noted by the small points. The hyperfine field was firstly measured from low temperatures up to room temperature, and then the temperature was lowered to the region where the discontinuity in the derivative was seen (left, lower figure). The right figure is a zoom of the last measurements.

4.6 Appendix

4.6.1 Low temperature PAC results

In this section, we show still unpublished additional PAC results obtained in MnAs at low temperatures. In a new experiment using a cryostat device, still with the ^{77}Br→ ^{77}Se probe, we measured the MHF at various temperatures, from 10 K up to room temperature. As discussed before the EFG is very small and cannot be properly measured in this phase. The resulting hyperfine fields are shown in the upper part of figure 4.14.

In the paper previously presented, these results were not yet discussed, and the comparison with the calculations was made with the 77 K measurement. With the present results, at the lowest temperature of 10.8 K, the comparison is more meaningful. The agreement between theory and experiments is now improved, the calculated value 54.3 T agrees well the measured value at 10.8 K, which is 50.3 T.

The most interesting feature found at low temperature is the anomaly at 150 K. The fact that there is an anomaly is shown by two features. An approximation of the derivative of the hyperfine field with respect to temperature is shown in the lower part of figure 4.14, and an irregularity is seen at this temperature, where the slope changes abruptly. The MHF was measured regularly, starting from low temperatures and heating until room temperature, and after that the sample was cooled again to this region to measure this anomaly in more detail (shown in the plot by red points). The measurements on heating were not replicated. The hysteresis and anomaly at this temperature are probably related to the pressure-temperature phase diagram, shown in figure 4.15. In it, an hysteresis region involving the hexagonal and orthorhombic phases starts precisely at 150 K, at zero pressure.

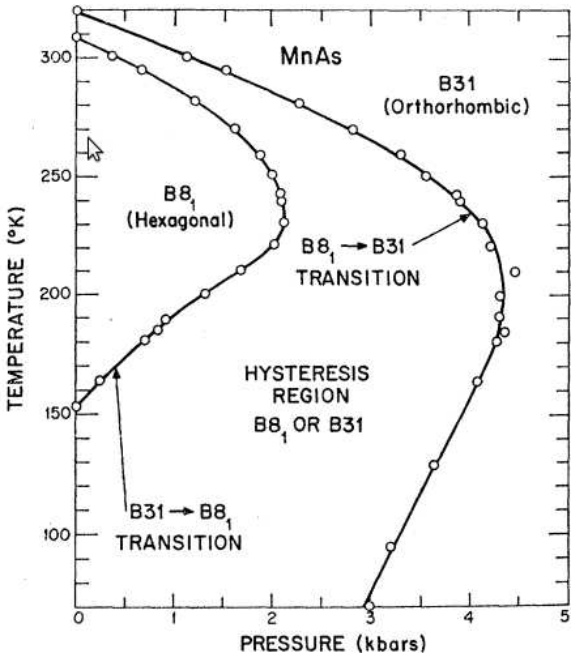

Figure 4.15: MnAs pressure-temperature phase diagram (taken from [131]).

4.6.2 NMR results

For reference, figure 4.16 presents the NMR resonance frequencies obtained at low temperatures by Pinjare and Rama Rao [110] and Amako [109].

Erratum

On page 58, it is stated: "On the other hand, this procedure agrees with the fact that the hexagonal and weakly distorted orthorhombic symmetries produce very small axial asymmetry parameters. ". This is a generalization which does not always hold, since the local symmetry of the site may give high asymmetry parameters in weakly distorted orthorhombic phases. One example is seen earlier, with $CaMnO_3$.

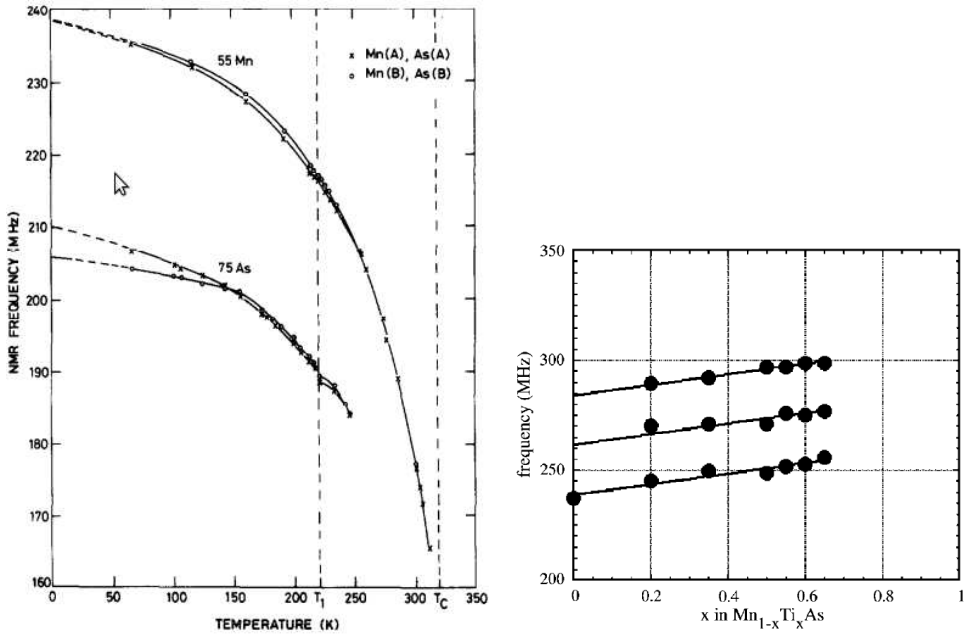

Figure 4.16: *Left*: Temperature of the NMR resonance frequencies measured with ^{55}Mn and ^{75}As in MnAs (taken from [110]). *Right*: Ti concentration dependence of the ^{55}Mn NMR frequency in $MnAs_{1-x}Ti_x$, at 4 K (taken from [109]).

Chapter 5

Ferroelectricity and Electric Field Gradients: an ab-initio study

The first experiences using hyperfine interactions applied to ferroelectric materials brought out some interesting results. It was found, in different materials, a quadratic [132] ($BaTiO_3$) or linear [133] (Rochelle salts) relationship of the EFG with respect to the spontaneous polarization. Figures 5.1(a) and 5.1(b) show these cases.

Yeshurun et al. [135] studied the electric field gradients (EFG) in perovskites, and predicted the relationship of local fluctuating EFGs in the lattice with the electric susceptibility. Their model assumes a cubic paraelectric structure, and considers the average displacement $z_0(T)$ from the high symmetry paralectric phase at a given temperature, plus the time-dependent part $\Delta z(T,t)$. Therefore, the time dependence of the displacement is $z(t,T) = z_0(T) + \Delta z(T,t)$. The instantaneous local EFG can be given by (considering here only the V_{zz} component) by $V_{zz} = V_{zz}(z=0) + \frac{dV_{zz}}{dz}z + \frac{1}{2}\frac{d^2V_{zz}}{dz^2}z^2 + ...$ The first term is zero by definition, from the cubic symmetry of the paraelectric phase, the second term vanishes also by symmetry but the third term remains. Therefore, $V_{zz} \propto z^2 = z_0^2 + 2z_0\Delta z + (\Delta z)^2$. The connection between the local instantaneous EFG and the EFG actually measured depends on the experimental technique

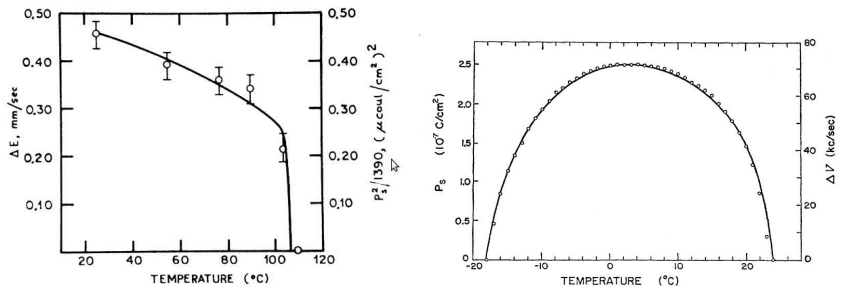

Figure 5.1: a) Quadrupole splitting measure by ^{57}Fe Mössbauer spectroscopy in $BaTiO_3$, with the spontaneous polarization squared (P_s^2) on a matching scale. b) The polarization and sattelite line separations in NMR (quadrupole coupling constant) varying with temperature (taken from [134]).

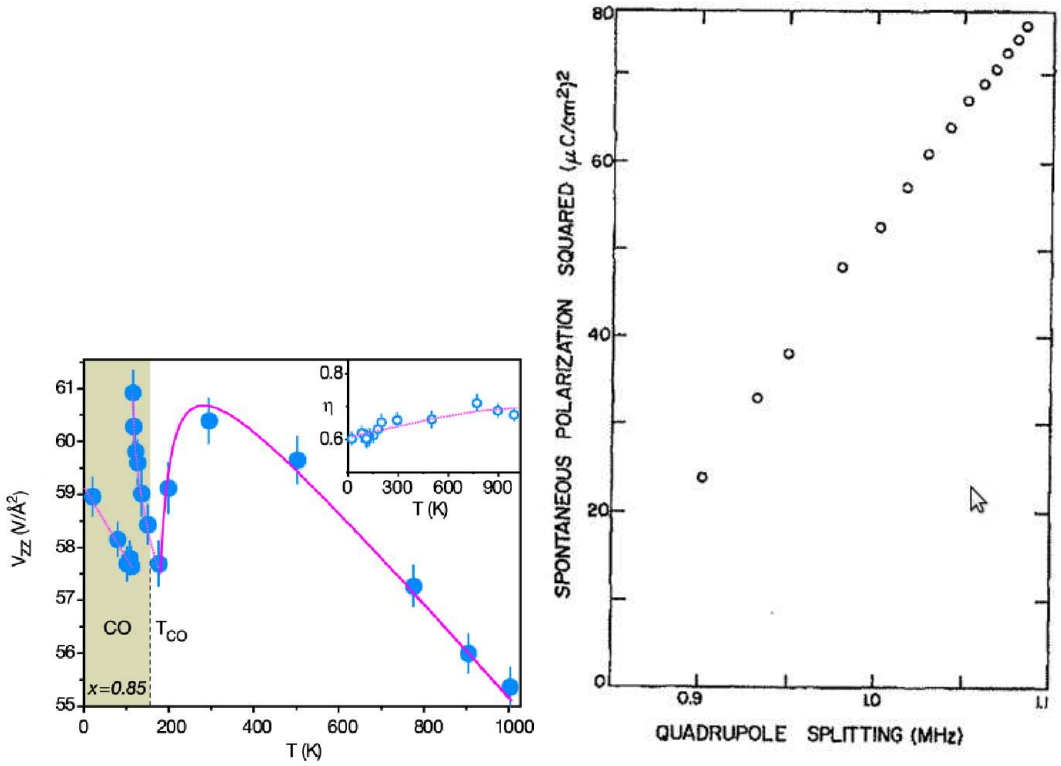

Figure 5.2: Left: Vzz $(V/\text{Å}^2)$ as a function of temperature, in the $Pr_{0.15}Ca_{0.85}MnO_3$ sample (η in the inset). Right: Plot of measurements in $NaNO_2$, of the square of the spontaneous polarization quadrupole splitting as a funtion of the quadrupole splitting, with temperature as an implicit parameter (taken from [134]).

used. The authors then extended the analysis to the case of the perturbed angular correlation (PAC) technique. They considered the fast and slow frequency regimes and conclude that in both cases V_{zz} should be proportional to the electric susceptibility. The derivation in both cases uses the fluctuation dissipation theorem, whereby the mean square of the fluctations $(\overline{\Delta z})^2$ is proportional to the sum over all q vectors of the electric susceptibility $(\overline{\Delta z})^2 \propto T \sum_q \chi_q$. Therefore, the EFG should have a critical behavior at the paraelectric-ferroelectric transition. This was successfully used as a supporting argument for the study of a novel phase transition in $Pr_{1-x}Ca_xMnO_3$ [6]. This brought a strong motivatios for a theoretical study of the relation between the EFG and ferroelectric properties. The measurement of the EFG with temperature variation as measured in one $Pr_{1-x}Ca_xMnO_3$ sample is shown in figure 5.2(a).

Concerning the static time-independent part of the EFG, Yeshurun et al. claim that V_{zz} should be proportional to P^2 in perovskites. Dening [134] also discusses this and argues that if the site has inversion symmetry in the paraelectric structure then the EFG is proportional to P^2, otherwise it is proportional to P. They use previous experimental results in $NaNO_2$ to validate the quadratic relation, presented in figure 5.2(b).

In spite of these previous models and experimental studies, a theoretical study from first-principles which relates these properties has not yet been attempted. Until recently, the po-

larization was not accurately calculated because the proper concept of polarization was only developed in the 1990s [18, 19], with the modern theory. In this conception the polarization is a bulk property, defined by the adiabatic flow of current as the crystal is modified. It is related to the Berry phase of the Bloch wavefunctions, or equivalently to the changes in the Wannier charge centers constructed from the same wave functions. Polarization is only defined *modulo* a "quantum of polarization", $e\mathbf{R}/\Omega$, where $\mathbf{R} = \sum_j m_j \mathbf{R}_j$ is a lattice vector and Ω is the unit cell volume. Therefore, it is a multivalued quantity, a lattice of vectors. In practice, by computing the polarization along many intermediate points in a path, the values can be chosen in a single branch, eliminating the uncertainty $\mod e\mathbf{R}/\Omega$.

In this chapter, to investigate the previously found relationship in perovskites, we study the variation of the EFG with respect to polarization, having static displacements as an implicit parameter, with the use of first-principles calculations of both quantities. The presentation of the main results in an article format, to be submitted. The final appendix presents supplementary materials related to the subject, for a better visualization of the results.

Ferroelectricity and Electric Field Gradients: an ab-initio study

J. N. Gonçalves,[1,*] A. Stroppa,[2] J. G. Correia,[3] T. Butz,[4] S. Picozzi,[2] and V. S. Amaral[1]

[1] *Departmento de Física and CICECO, Universidade de Aveiro, 3810-193 Aveiro, Portugal*

[2] *CNR-SPIN L'Aquila, Italy*

[3] *Instituto Tecnológico e Nuclear, UFA, 2686-953 Sacavém, Portugal*

[4] *Fakultät für Physik und Geowissenschaften, Institut für Experimentelle Physik II, Universität Leipzig, Linnéstrasse 5, 04103 Leipzig, Germany*

(Dated: January 6, 2012)

The hyperfine interaction between the quadrupole moment of atomic nuclei and the electric field gradient (EFG) provides information on the electronic charge distribution at a given atomic site. In ferroelectric materials, the loss of inversion symmetry of the electronic charge distribution is necessary for the appearance of the electric polarization. We present first-principles density functional theory calculations of ferroelectric materials such as $BaTiO_3$, $KNbO_3$, $PbTiO_3$ and other oxides with perovskite structures, by focussing on both the EFG tensors and the ferrolectric polarization. We analyzed the EFG tensor properties such as orientation and correlation between components and their link with electric polarization. Our work supports previous studies of ferroelectric materials where a relation between the EFG tensors and the polarization was observed.

Abstract

The hyperfine interaction between the quadrupole moment of atomic nuclei and the electric field gradient (EFG) provides information on the electronic charge distribution close to a given lattice site. In ferroelectric materials, the main property is the macroscopic polarization, which also depends on the electronic charge distribution due to the loss of the inversion symmetry. We present first-principles density functional theory calculations of ferroelectric materials such as $BaTiO_3$, $KNbO_3$, $PbTiO_3$ and other oxides with perovskite structures, by focussing on both the EFG tensors and the ferrolectric polarization. We analysized the EFG tensor properties such as orientation and correlation between components and their link with electric polarization. This study aims to support previous studies of ferroelectric materials where a relation between the EFG tensors and the polarization was observed, that we confirm now, by establishing this relationship on a solid ground of first-principles methods. Hopefully, when this relation is well understood, a new door is open to disentangle ferroelectric ordering in materials where standard techniques to study polarization are not easily applied.

5.1 Introduction

There is great interest in ferroelectric/multiferroic materials nowadays due to their potential application in a panoply of subjects, ranging from high density memories to magnetoelectric sensors [8, 9]. The complexity of electronic phenomena at the nanoscale makes them a research hot topic and a fertile ground for new experimental techniques which are able to probe point-like, atomic-scale properties. To this aim, the use of local probes such as in hyperfine interactions techniques, like Mössbauer effect spectroscopy, perturbed angular correlation (PAC) spectroscopy, nuclear magnetic resonance (NMR), and nuclear quadrupole resonance (NQR), give access to atomic scale information of the electronic charge density [22] through the measure of the the electric field gradients (EFGs), thus probing the phenomenology of materials at the

nanoscale.

From a theoretical point of view, advances in modern density functional theory have made the calculation of the spontaneous electric polarization (P) a routine calculation on ab-initio framework [136, 18, 19]. Recently, the calculation of EFGs, which are quantities directly accessible to experiments, have become also possible from first-principles [137, 138, 39, 139, 140, 141, 142]. However, to the best of our knowledge, a theoretical study on the framework of *ab-initio* density functional mehods aiming to investigate both the P and EFGs in a ferroelectric material is still missing in the current literature despite the fact that it was shown a long time ago a linear correlation[133, 143, 144] between P and EFG values at a given site. This "correlation" would suggest that informations obtained through the measurements of EFG tensors can provide indirect access to the polarization as well. If true, one could study a macroscopic property of the crystal, such as P by using local probes. In this work, we want to explore such a possibility.

A nucleus with nuclear spin $I \geq 1$ has a non-spherical nuclear charge distribution, i.e. a non-zero quadrupole moment. The hyperfine techniques previously mentioned can measure the quadrupole coupling constant, which is the interaction between the nuclear quadrupole moment and the EFG. The EFG, in turn, arises due to the Coulomb potential at the nucleus, and is a sensitive measurement of the surrounding electronic charge density. More precisely, it is defined as the symmetric traceless second-rank tensor of second derivatives of the Coulomb potential with respect to to the spatial coordinates, $V_{ij} = \partial^2 V/(\partial x_i \partial x_j)$, at the nuclear position. In the principal axis coordinate system, the tensor is diagonal and its elements are ordered by the convention $|V_{zz}| \geq |V_{yy}| \geq |V_{xx}|$. Usually V_{zz} and the axial asymmetry parameter $\eta = (V_{xx} - V_{yy})/V_{zz}$ are used in the analysis of measurements. We recall that the EFG is lattice site dependent, and its principal axes ($\tilde{x}$,$\tilde{y}$,$\tilde{z}$) may not be the same at every site, although they are usually along symmetry axes of the crystal.

Previous studies have shown that in some ferroelectric materials, P follows a temperature dependence which can be related to the EFG at specific atomic sites. For instance, Nuclear magnetic resonance (NMR) using ^{23}Na in Rochelle salts [NaK(tartrate)$\cdot 4H_2O$] showed P and EFG are linearly related [133, 143, 144]. In 1978 Yeshurun suggested [135] that the EFG due to static displacements should be proportional to P^2 in perovskite crystals using an empirical model for interpreting previous ^{57}Fe Mössbauer measurements in $BaTiO_3$ [132]. Dynamical aspects were also considered by relating the EFG to the electric susceptibility, and it was found that the EFG should have a critical behavior when approaching T_C [135]. This peculiar feature was recently used in the identification of ferroelectricity with EFG measurements [6]. In this work, the $Pr_{1-x}Ca_xMnO_3$ was studied with the measurement of the EFG at ^{111m}Cd probes implanted into the sample. An abrupt change was found in a short temperature interval. This was associated to the onset of ferroelectricity, since the EFG should be dominated by a contribution proportional to the electrical susceptibility at the transition, *i.e.* with its critical behavior [135]. In the same work, [6] it was also suggested that the temperature dependence study of EFG tensor can give information on the onset of the charge or orbital ordering (CO or OO). phase. In Ref. [134] it was shown the static part of V_{zz} should have the following behaviour with respect to P: either it is proportional to P^2 in sites which have inversion symmetry in the paraelectric

structure, or P is proportional to the EFG, like in Rochelle salts. The quadratic relation was supported by experiments in $NaNO_2$ [134], and in $PbHfO_3$, not too close to T_C (where critical behaviour is found), by perturbed angular correlation (PAC) measurements [145][1]. It is therefore clear from the current literature that P and EFG tensor are closely related quantities. Our study aims to explore this direction, by calculating both P and EFG for simple ferroelectric materials and studying a possible correlation between these quantities.

This work is organized as follows. In Sect. 5.2 we discuss the computational details. In Sect. 5.3.1 we present the results and discuss the relationship between P and V_{zz} for simple tetragonal or more orthorhombic systems 5.3.2. Finally, we analyze the possible linear correlations between EFG tensor components in Sect. 5.3.3. Finally, in Sect. 5.4 we draw our conclusions. A study of the variation of $V_{zz}(P)$ with the atomic numbers of different materials is shown in the Appendix 5.5.

5.2 Technical details

We have considered a series of simple ABX_3 type perovskite compounds. [146] For $BaTiO_3$, $PbTiO_3$ and $KNbO_3$ we have considered the tetragonal experimental structures. We also considered other perovskite-related compounds, such as $BaZrO_3$, $CaTiO_3$, $PbZrO_3$, $SrTiO_3$, $NaNbO_3$ and $LiNbO_3$ by considering a pseudo-cubic phase at the experimental lattice constants of the cubic paraelectric phase. The ferroelectric distortion was mimicked by a polar displacement of the atoms.

The experimental displacements in tetragonal $BaTiO_3$ are $z_{Ti} = 0.0203$, $z_{O1} = -0.0258$, and $z_{O2} = -0.0123$, in fractional coordinates. We calculate the EFG as a function of Δ_z, which represents the fraction of the displacements (z_{Ti}, z_{O1}, z_{O2}) mentioned above. Therefore, $\Delta_z = 1$ corresponds to the equilibrium (experimental) structure. Values of $0 \leq \Delta_z \leq 1.2$ are used.

For the compounds where the cubic structure is used, a ferroelectric state is considered using the same fractional distortions as in $BaTiO_3$. Although these states may not be observed in normal conditions, this allows us to study the possible correlation of polarization and EFG in different systems or as a function of strain.

The density functional theory calculations use the PAW method [28], as implemented in the *Vienna ab-initio simulation package* (VASP) [28], with the GGA-PBE functional [43]. We used a gamma-centered Monkhorst-Pack 7×7×7 k-points grid, and an energy cutoff of 400 eV. The polarization is calculated with the Berry phase approach [18, 19]. The EFG is calculated at the atomic sites (A, B, and apical O(1), equatorial O(2) sites).

[1] This technique measures the precession of nuclear spins, by the angular correlation of a γ-γ decay cascade, emmited by probe isotopes introduced in the sample. It works by measuring the coincidence rate of a γ-γ decay cascade, the first decay selecting only those isotopes with a preferred orientation (and associated anisotropic radiation pattern), and the measuring the correlation of the second decay in relation to the first. The resulting anisotropy correlation function has a perturbation during the lifetime of the intermediate state which is due to the hyperfine interactions.

Table 5.1: Lattice constants (in Å) and fractional atomic distortions in the c direction used in the calculations of the perovskite compounds. (a) Cubic lattices, experimental values [146]. (b) Theoretical lattice parameter, found by the volume optimization in the cubic phase, with atoms at the ideal positions.

Compound	a	c	δ_A	δ_B	δ_{O1}	δ_{O2}
$BaTiO_3$ [147]	4.00	4.03		0.02	-0.03	-0.01
$KNbO_3$ [148, 149]	4.00	4.06	0.02		0.04	0.04
$PbTiO_3$ [150, 151]	3.90	4.16		0.04	0.11	0.12
$BaZrO_3$ (a)	4.19					
$CaTiO_3$ (a)	3.83					
$NaNbO_3$ (a)	3.94					
$PbZrO_3$ (a)	4.13					
$SrTiO_3$ (a)	3.91					
$LiNbO_3$ (b)	4					

5.3 Results

5.3.1 Relation between EFGs and P

We start by discussing the case of $BaTiO_3$. The variation of the total energy with the distortion is shown in figure 5.3(a). The curve shows the expected double well profile and the theoretical distortion (corresponding to the energy minimum) is close (85%) of the experimental distortion, with a 20 meV energy difference between the undistorted and theoretical structures [2]. The calculated P value is 28.6 μCcm^{-2} while the experimental is 27 μCcm^{-2}. In all results the vertical dashed and point lines correspond to the calculated energy minimum (at the experimental lattice constant) and experimental distortion respectively.

Figure 5.3(b) presents P as a function of the ferroelectric distortion [3]. One can see that P is approximately a linear function of the distortion. This appears to be the general case in perovskite ferroelectrics, as found in previous calculations [152].

Figure 5.3(c) shows the EFG component V_{zz} as a function of distortion for all sites.

Figure 5.3(d) shows the V_{zz} EFG component as a function of P^2. The lines are linear regressions to the data, and the good agreement shows that V_{zz} at each site varies linearly with P^2.

The results obtained for $KNbO_3$ are similar and a linear relation is also seen in figure 5.4(a).

At the A, B, and apical O1 atoms, the relation found in almost all the compounds considered here is $\begin{pmatrix} \Delta V_{xx} & 0 & 0 \\ 0 & \Delta V_{yy} & 0 \\ 0 & 0 & \Delta V_{zz} \end{pmatrix} = \Delta P^2 \times \begin{pmatrix} a_{xx} & 0 & 0 \\ 0 & a_{yy} & 0 \\ 0 & 0 & a_{zz} \end{pmatrix}$. However, since these sites have $\eta = 0$, the tensor is defined by only one independent parameter. $V_{xx} = V_{yy} = -1/2V_{zz}$, and the quadratic coefficients also follow the same symmetry $a_{xx} = a_{yy} = -1/2a_{zz}$. The equatorial oxygen sites

[2] For $KNbO_3$, $PbTiO_3$ the same shape of energy curve is obtained with energy differences of 30, 20 meV and theoretical distortions at 85, 94%. For the other compounds the energy minimum is the undistorted phase, as expected, except for $LiNbO_3$ which has a minimum at small values of distortion.

[3] For BaTiO3 and $KNbO_3$ we considered the displacements also opposite directions, with P taking negative and positive values. In other cases the distortion is taken only for the direction of positive P along the polar axis.

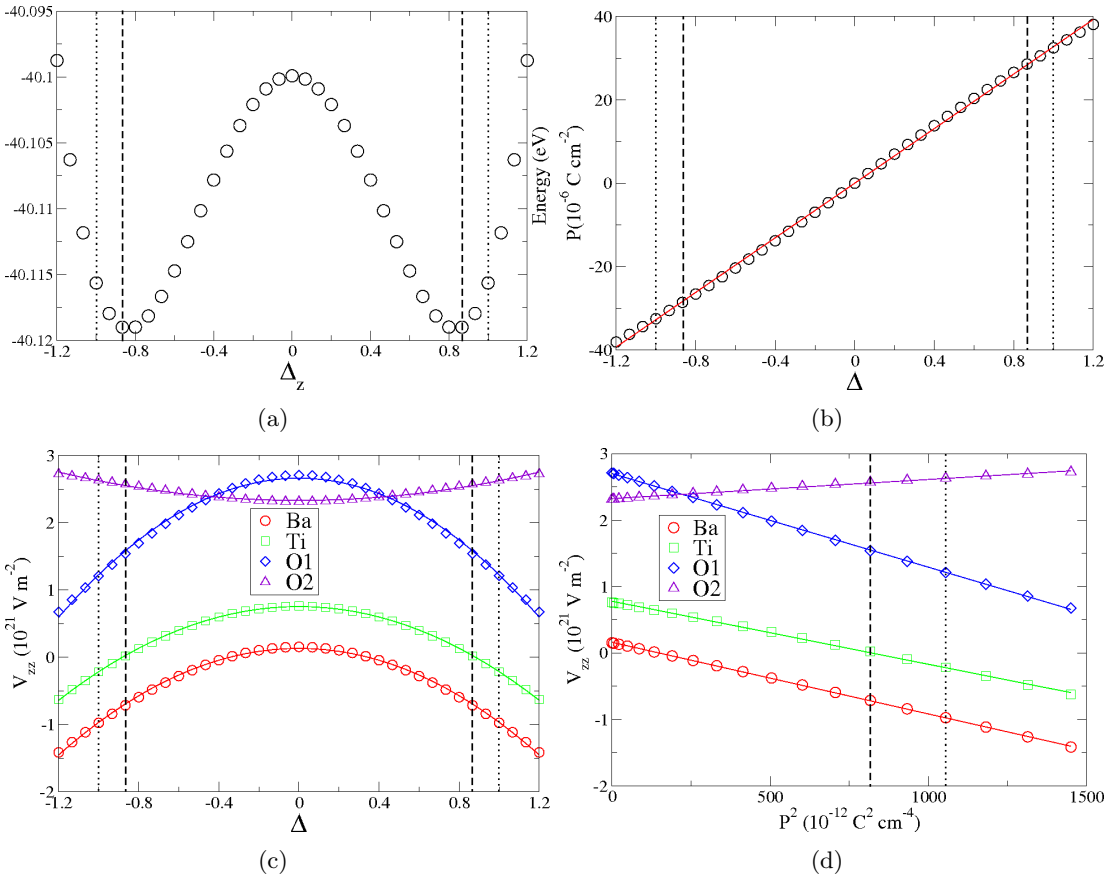

Figure 5.3: $BaTiO_3$ in the tetragonal phase. (a) Energy (eV) as a function of distortion. The distortion of Ti and O atoms is varied in equal intervals from 0 to 1.2. (b) Polarization ($\mu C/cm^2$) as a function of distortion. The vertical dashed line corresponds to the calculation of minimum energy. The vertical point line corresponds to the experimental distortion. (c) V_{zz} (10^{21} V/m^2) at each site, as a function of distortion . d) V_{zz} at each site as a function of P^2 (pC^2cm^{-4}). The lines are quadratic fits to the data.

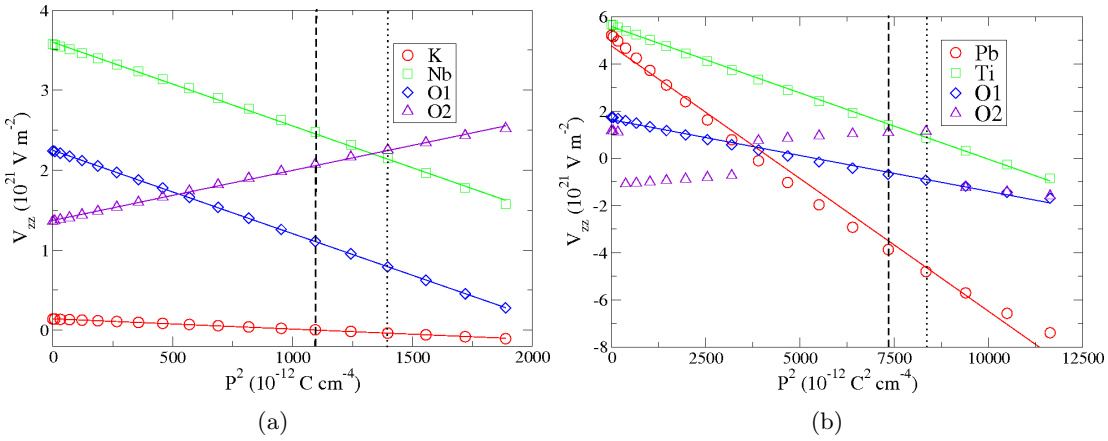

Figure 5.4: V_{zz} at each site as a function of P^2 (pC^2cm^{-4}). The lines are quadratic fits to the data.(a) $KNbO_3$, (b) $PbTiO_3$, in the tetragonal phases.

Table 5.2: Fit coefficients for the O2 atoms. V(P)=V(0)+$a\times$P^2. V(0) in units of 10^{21} V/m^2, a in units of 10^{22}Vm^{-2}C^{-2}.

Compound	EFG component	V(0)	a
$BaTiO_3$	V_1	1.310	-0.0192
	V_2	1.030	0.2965
	V_3	-2.341	-0.2773

(O2) sites [at (0.5,0,0.5) and (0,0.5,0.5) in the reference structure] do not have an n-fold rotation axis like $n \geq 3$. This implies that the axial symmetry parameter is not zero. In this case the variation of the EFG tensor as a function of P does not show such a simple relation.

The V_{zz} component follows a quadratic variation for all the atoms in all the compounds studied, with only two exceptions, $PbTiO_3$ and $CaTiO_3$. At the Pb site of $PbTiO_3$ a small cubic term in the polarization is found necessary for a good fit (not shown). At the O2 sites of $BaTiO_3$, $PbTiO_3$ and $CaTiO_3$ there are interchanges of components, which will be explained next.

The variation of the EFG with displacements can be understood by considering a Taylor series expansion.

$$V_{zz} = V_{zz}^0 + \sum_i \frac{\partial V_{zz}}{\partial r_i}\delta r_i + \sum_i \frac{\partial^2 V_{zz}}{\partial r_i^2}\delta r_i^2 + ...$$

where δr_i are small deviation with respect to the atomic positions in the paraelectric structure. When the transition involves small displacements and for atoms where the EFG does not undergo large changes in the transition this expansion should converge rapidly. For sites without inversion symmetry the linear term should be dominant, whereas for sites with inversion symmetry the linear term vanishes and the quadratic term in the expansion becomes relevant [134].

The coefficients obtained are shown in table 5.3, for all the constituent atoms.

EFG tensor directions and component interchanges

In the paraelectric structure of $BaTiO_3$ the principal component of the tensor V_{zz} for the Ba and Ti atoms is aligned along the z axis. For the O atoms, the EFG tensor is also aligned with the tetragonal crystalline axes, and V_{zz} is directed to the neighbouring Ti atoms. For $BaTiO_3$, with increasing ferroelectric distortion (P), in all distortions calculated, the direction of V_{zz} remains the same for all atoms. The V_{xx} and V_{yy} components also mantain their directions in this path, for the Ba, Ti and O1 atoms, along the x and y axes respectively. For the O2 atoms, however, the V_{xx} and V_{yy} do not always correspond to the same orientations. The three components of the EFG tensor for O(2) site in $BaTiO_3$ are shown in figure 5.5(a). At a given distortion, due to the convention $|V_{yy}| \geq |V_{xx}|$ the regular curves followed by these components are interchanged. For distortion $\Delta \leq 0.9$ the directions for V_{xx}, V_{yy} are z and x for O2 at (0.5,0,0.5); z and y for O2 at (0,0.5,0.5). For higher Δ these directions are interchanged. Nevertheless, the quadratic behavior of EFG(P) is maintained here and this interchange is ignored.

Table 5.2 shows the coefficients of the quadratic terms for the variation of the EFG tensor

Table 5.3: Coefficients a for the fits of the expression $V_{zz}(P) = V_{zz}(0) + a \times P^2$. $V_{zz}(0)$ in units of 10^{21} Vm^{-2}, a in units of $10^{22} V\ m^{-2}C^{-2}$, for the compounds in tetragonal and cubic perovskite type structures.

	$BaTiO_3$		$KNbO_3$		$BaZrO_3$		$CaTiO_3$		$PbZrO_3$	
	$V_{zz}(0)$	a	$V_{zz}(0)$	a	$V_{zz}(0)$	a	$V_{zz}(0)$	a	$V_{zz}(0)$	a
A	0.16	-1.080	0.14	-0.128	0.00	-0.945	0.00	-0.186	-0.01	-1.911
B	0.78	-0.949	3.60	-1.042	0.00	-0.759	0.01	-0.724	-0.02	-0.985
O1	2.70	-1.410	2.25	-1.041	-1.43	-1.124	-0.114	1.025	-3.61	1.009
O2	2.32	0.288	1.37	0.625	-1.41	0.300s	–	–	-3.59	0.232

	$SrTiO_3$		$NaNbO_3$		$LiNbO_3$		$PbTiO_3$	
	0.00	-0.551	0.00	-0.077	0.00	-0.012	5.28	-1.787
	0.01	-0.834	-0.00	-0.164	0.00	-0.311	5.58	-0.562
	1.08	-1.193	0.30	-0.882	0.67	-0.940	1.63	-0.303
	1.11	0.253	0.32	0.389	0.69	0.363	–	–

components at each crystalline axis direction. For $BaZrO_3$, $PbZrO_3$, $NaNbO_3$, $LiNbO_3$ and $SrTiO_3$ there are no interchanges between tensor components, while for $CaTiO_3$ and $PbTiO_3$ there are exchanges between the 3 components. For the sake of clarity, we show only here the O2 EFG tensor components for $PbTiO_3$ (figure 5.5(b)), where there are as many as 6 interchanges of one tensor component in the range of distortions considered. In particular, there is an interchange near the experimental distortion of which one should be aware in EFG measurements, since a kink measured in a V_{zz} dependence could be a consequence of the convention that V_{zz} is the largest EFG component in magnitude, instead of a phase transition.

Moreover, as already mentioned, to obtain a satisfactory fit to $V_{zz}(P)$ at the Pb site a small cubic term should also be considered (fig. 5.4(b)), $V_{zz}(P)$ follows approximately a linear behavior for larger values of P^2, and at the O2 site two of the curves of components with constant direction also need cubic terms for a good fit (fig. 5.5(b)). The much larger displacements in this compound would indeed indicate that the $V_{zz}(\delta r)$ expansion does not converge so fast as in other cases.

5.3.2 Orthorhombic structure

$BaTiO_3$ exhibits monoclinic, rombohedral, and orthorhombic phases at different temperatures. In order to see what are the differences in the EFG and P with a change of structure, we have made a series of calculations in the orthorhombic phase. We also took one experimental measurement [147] of the orthorhombic structure as the reference distortion ($\Delta = 1$) and calculated from $\Delta = 0$ to $\Delta = 1.2$ of this distortion keeping the lattice parameters (a, c) constant. The theoretical distortion of minimum energy is once again found to be close to 85% the experimental distortion.

The resolved components of the EFG tensors at the four inequivalent atoms against P^2 are displayed in figure 5.6, and the coefficients resulting from the fits are in table 5.4. In this structure there is not a single site with axial symmetry, and the relationship between EFG and P will never be as simple as discussed above. There are also discontinuities in V_{zz} at Ba and

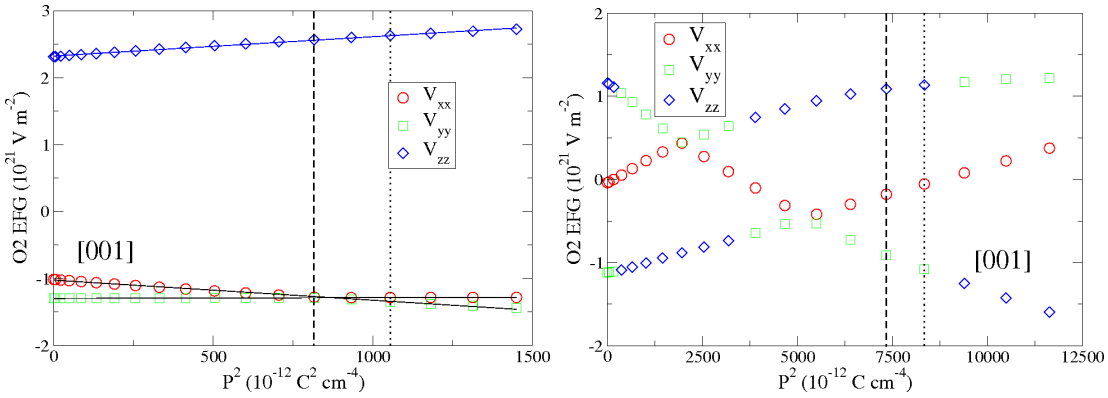

Figure 5.5: (a) $BaTiO_3$ in the tetragonal phase: V_{zz}, V_{yy}, and V_{xx} components of the EFG tensor for the O2 atoms as a function of P^2. The lines are fits to the components of constant direction. (b) $PbTiO_3$ in the tetragonal phase: V_{zz}, V_{yy}, and V_{xx} components of the EFG for the O2 atoms as a function of P^2. The [001] direction are also indicated. Depending on the specific atom, two of the curves correspond to either the [100] or [010] directions.

Table 5.4: Coefficients a for the fits of the expression $V(P) = V(0) + a \times P^2$ for $BaTiO_3$ in the orthorhombic phase, where $V_{1,2,3}$ is a component of the tensor with regular variation. $V_{1,2,3}$ in units of $10^{21} V\ m^{-2}$, $a_{1,2,3}$ in units of 10^{22}V m^{-2}C^{-2}.

	Ba	Ti	O1	O2
$V_1(0)$	-0.17	-0.80	2.17	-1.13
a_1	0.563	0.498	0.318	0.193
$V_2(0)$	-0.11	0.48	-1.07	-1.45
a_2	-0.256	-0.829	-0.174	0.411
$V_3(0)$	0.27	0.32	-1.09	2.58
a_3	-0.307	0.331	-0.144	-0.605

Ti sites due to the interchange of components. Nevertheless, ignoring these interchanges, the relation for each direction is purely quadratic in all cases. These results, like the previous ones, show that there is no physical meaning in the change of the principal axis definition (as xx, yy, or zz), and that the conventional assignment may obscure a simpler relation with crystal axes.

5.3.3 Correlations between EFG tensor components

For the cases studied with tetragonal and cubic lattice parameters, $\eta \neq 0$ only in the O2 atoms. For $\eta = 0$ the components of the EFG are trivially related, but when $\eta \neq 0$, the possible correlation between tensor parameters should be studied. Any correlations between the components of the tensors can be interpreted in a plot of one component against the other and not in the usual parametrization of V_{zz} and η.

However, just plotting V_{zz} against V_{xx} results in a distorted cobweb plot, where continuous EFG tensor trajectories are not correctly connected through the line $\eta = 1$. Czjzej proposed a

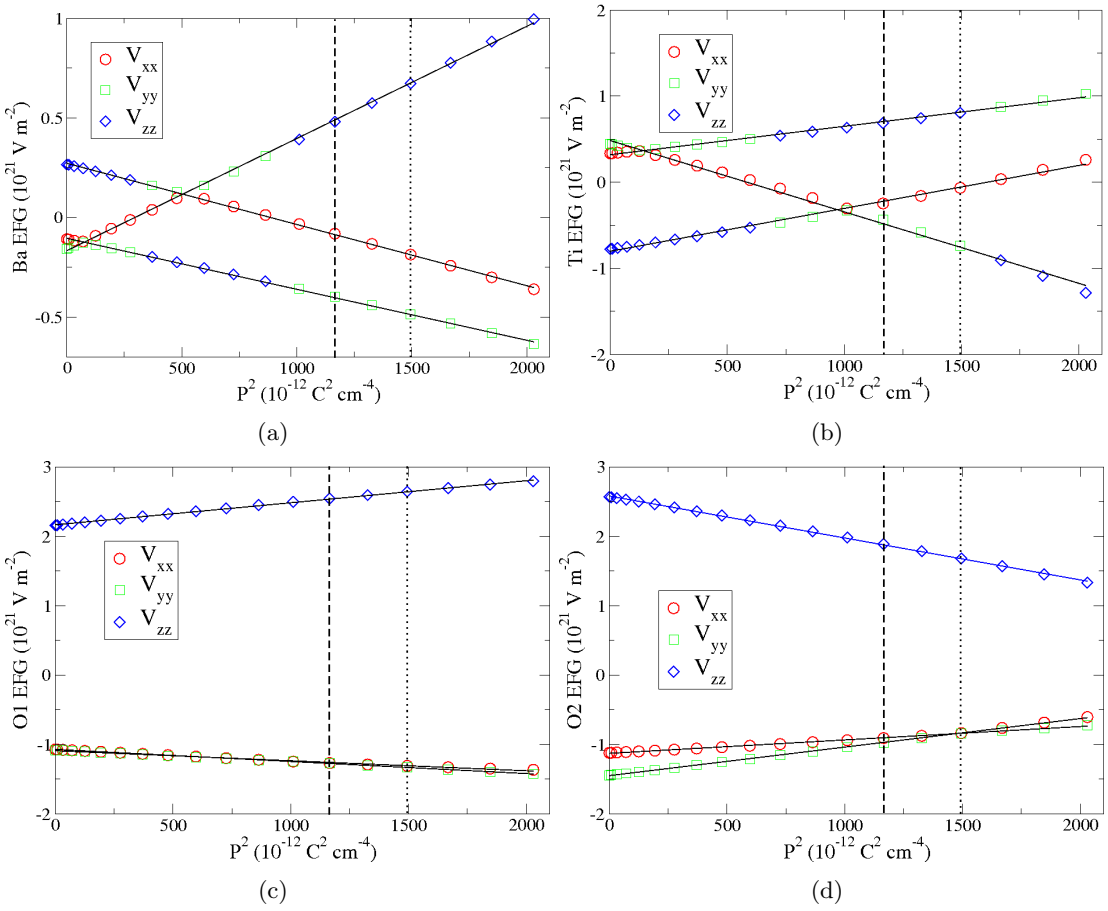

Figure 5.6: EFG tensor components in the principal coordinate system, of (a) Ba, (b) Ti, (c) O1 and (d) O2, as a function of P^2 for orthorhombic $BaTiO_3$. The lines are fits to the tensor components of constant directions.

different system to erase these problems [153], initially to deal with the analysis in amorphous systems. However it is also suited to investigate the correlations between the tensor components [154, 155]. This plot, with $-2V_{xx}$ as a function of $|2(2V_{zz}+V_{xx})/\sqrt{3}|$ is especially useful for this. With these linear combinations of tensor components, the tractories are connected, and straight if there is a linear dependence of V_{zz} on V_{xx}. In this plot, the lines of constant η are the diagonal lines: the boundary lines correspond to $\eta = 0$ and the horizontal line corresponds to $\eta = 1$. The herringbone lines correspond to constant V_{zz}. The upper (lower) wedge is for positive (negative) V_{zz}.

Reflections at the boundary of the plots, seen for example in $BaTiO_3$ and $KNbO_3$ are associated with the interchange of V_{xx} and V_{yy} components previously shown, and the passing of the trajectory by the line $\eta = 1$ corresponds to change in sign and orientation of V_{zz}, which shows that interchanges may only appear with changing η. The trajectories in the Czjzek plot of all the cases except for the orthorhombic structure are shown in figure 5.7.

If the trajectories in this plot are straight lines, this shows that the EFG tensor components are linearly related. This is usually the case, except for $LiNbO_3$ and $NaNbO_3$, where the trajectory is approximately straight for low values of P, but becomes curved for higher values. This means that the whole tensor, when considering the distortions that give rise to ferroelectric polarization, can be described by a *single* parameter. This might have important implications on the way experimental data should be analyzed, since the components are not independent, and the combination of all information will be more useful than each of them taken separately. The study of the EFG dependence on temperature (or on other variables) usually done by separating V_{zz} and η, can be performed by identifying the global single parameter.

5.4 Conclusions

In summary, our calculations provide a theoretical ab-initio support for previous observations of a quadratic dependence of V_{zz} versus P in ferroelectric materials with the perovskite structure and other distorted structures. Exceptions to this rule are seen in $CaTiO_3$ and $PbTiO_3$ where exchange of directions of the tensor orientation and a cubic (additional term) dependence are observed. However, for most cases the local symmetry of the atom means that the EFG tensor is axially symmetric and all the components are trivially related to each other. For the equatorial oxygen atoms this is not the case. Nevertheless, the components of the EFG tensor are quadratically related to P and linearly correlated to each other for most cases.

We hope this work will stimulate more EFG studies. If only a static contribution to the EFG is involved, which should be the case far from the transition, this study shows that measurements of EFG variations can be directly related to polarization variations for most ions of perovskite compounds. One could in principle get accurate values for the variations of polarization from EFG experiments, using the ab-initio values of EFG and P as calibrations.

The EFG, working as a local analogue of P, has the added advantage of higher spatial resolution and short time scales, which allows local probing of nanoscale phenomena at specific lattice sites. The different types of lattice sites, including defects, can be discriminated by

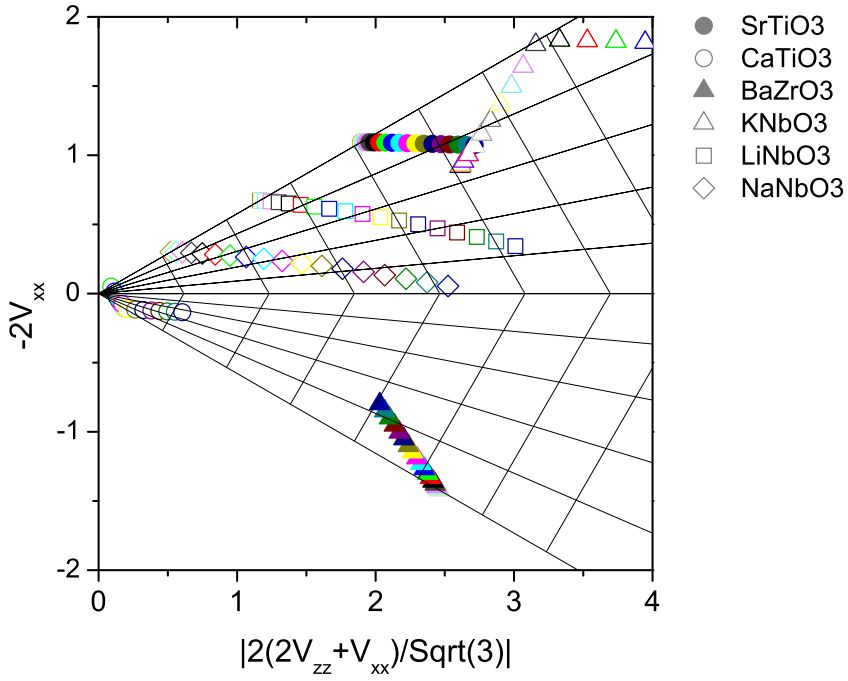

(a)

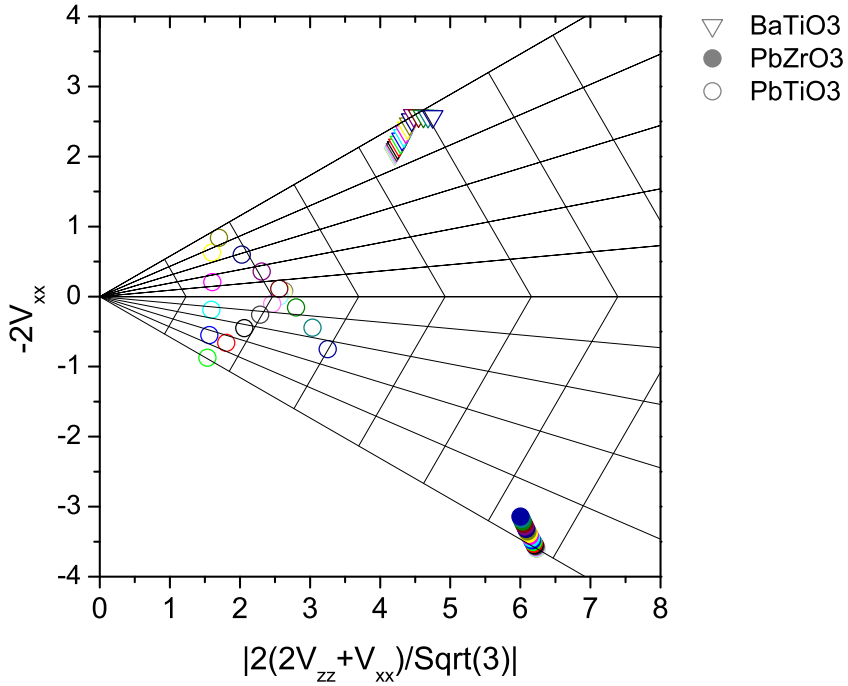

(b)

Figure 5.7: Cjzjek plots for trajectories with P (or distortion), as implicit parameters in the perovskite materials studied, at the equatorial oxygen (O2) sites.

their different EFGs. Its critical behavior in phase transitions may be analyzed, and the order of the transitions can be established with a high degree of detail. In hysteresis loops, it can act as a static measurement of the electric polarization in individual domains, not limited by depolarization effects much more sensitive to polarization reversal. It is also suited to probe phase coexistence or inhomogeneous polarization states with atomic selectivity, well beyond the reach of conventional polarization measurements. Moreover, piezoelectric force microscopy is usually restricted to studies near the surface of samples, while EFG studies can be performed in bulk or at the surface of materials, by using diffusion, evaporation or implantation techniques to add the probe atoms in the environments to study.

5.5 Appendix : Supplementary information

This section presents some complementary results from the calculations described in this chapter: the visualization of the electron densities corresponding to the ferroelectric and paraelectric states of a few cases, the graphics of the polarization dependence of the EFG in the other perovskite structures considered ($BaZrO_3$, $CaTiO_3$, $LiNbO_3$, $NaNbO_3$, $PbZrO_3$, $SrTiO_3$), and the plot of the energy as a function of distortion for the classic ferroelectric materials studied, $KNbO_3$ and $PbTiO_3$. $BaTiO_3$ was already presented in the main text, figure 5.3(a). Finally we analyze a trend found for the $V_{zz}(P)$ function in the different compounds studied.

Electron densities Figure 5.8 shows the electron densities of the valence electrons in $BaTiO_3$, in the xz TiO_2 plane, in for the paraelectric (ideal positions) and experimental ferroelectric tetragonal structures. The asymmetry in the c direction responsible for the polarization is clearly seen in the second plot, with an increase in electron density between the Mn and O (upper) atoms, relative to the paraelectric case.

Fig. 5.9 shows the electron density for $PbTiO_3$. In this case the changes are much more pronounced than in $BaTiO_3$, as expected from the larger atomic displacements. These plots were obtained with the L/APW+lo method (WIEN2K code), with the GGA-PBE functional.

$V_{zz}(P)$ for the pseudocubic perovskites Figure 5.10 shows V_{zz} as a function P^2 of for the cases presented in table 5.3, except for $BaTiO_3$, $KNbO_3$ and $PbTiO_3$, which are shown in the previous sections. P^2 correspond to the structures with distortion from 0 up to $\Delta = 1.2$, where $\Delta = 1$ is the experimental value of the distortion, keeping the lattice parameters fixed to the experimental values in all the calculations. The perfect agreement with the linear regression fits shows the quadratic dependence of $V_{zz}(P)$.

Energy Figure 5.11 shows the calculated energy as a function the ferroelectric distortion Δ_z for $KNbO_3$ and $PbTiO_3$, calculated with the PAW method (VASP), with the GGA-PBE functional. The distortion corresponding to the experimental measurement is close to the distortion of the energy minimum, as expected. For $KNbO_3$ distortions corresponding to positive and negative P were calculated, while for $PbTiO_3$ the distortion is taken only in the path $0 \rightarrow +P$.

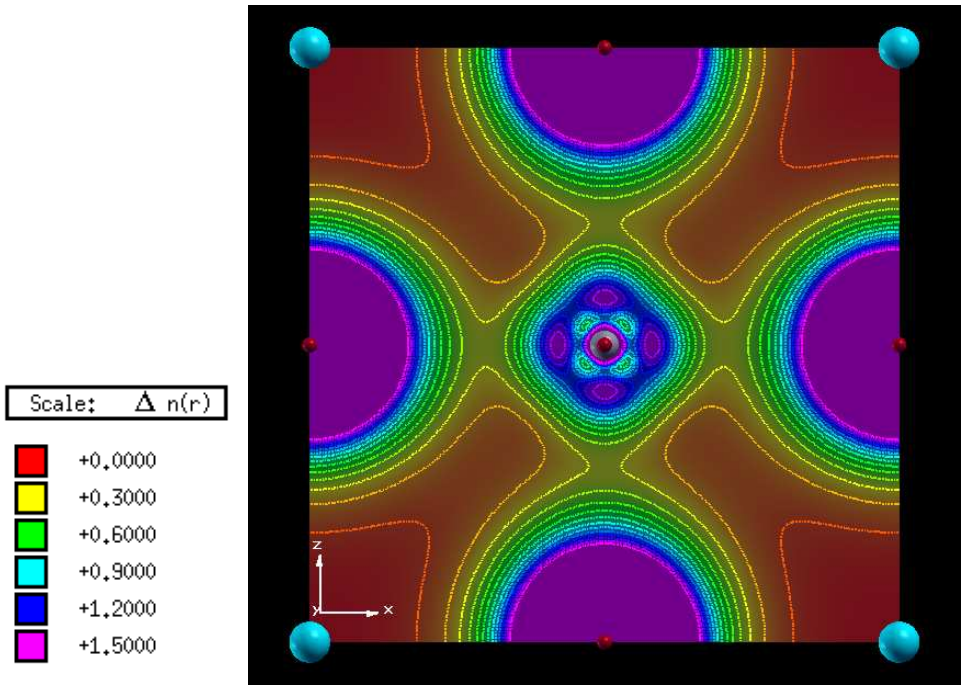

(a) (b)

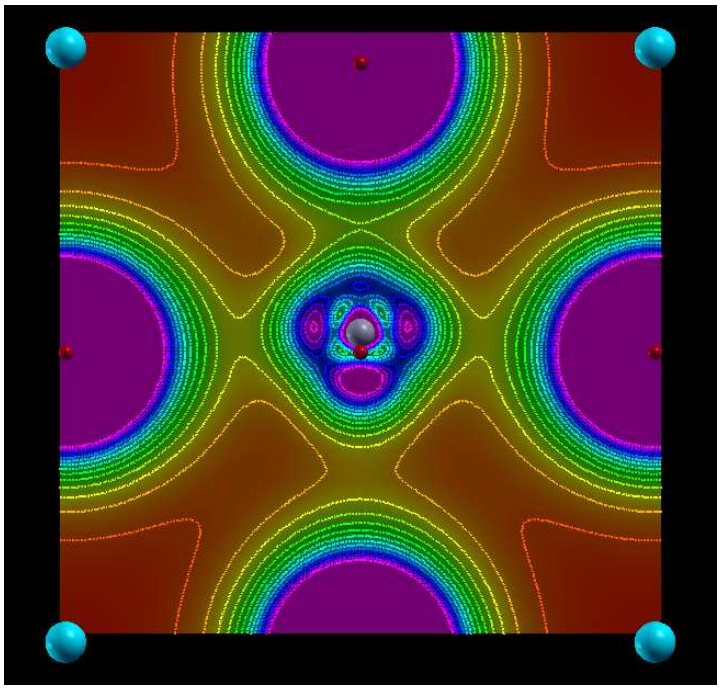

(c)

Figure 5.8: Electronic density of $BaTiO_3$ in the xz TiO_2 plane, for b) paraelectric and c) ferroelectric structures. The isolines are in units of $e/\text{Å}^3$ [scale in a)].

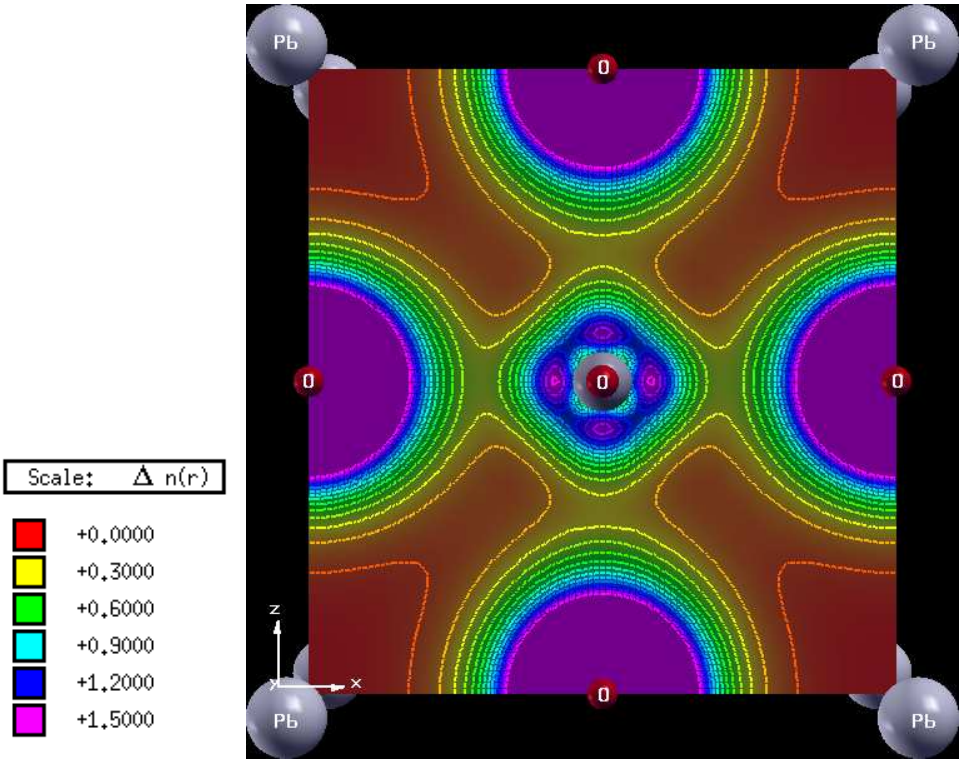

(a) (b)

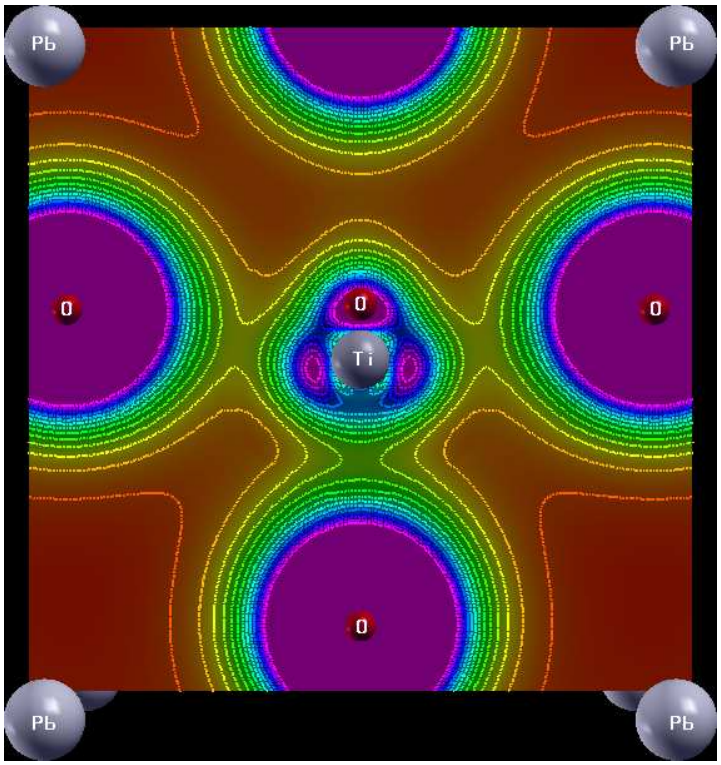

(c)

Figure 5.9: Electronic density of $PbTiO_3$ in the xz TiO_2 plane, for the b) paraelectric and c) ferroelectric structures. The isolines are in units of $e/\text{Å}^3$ [scale in a)].

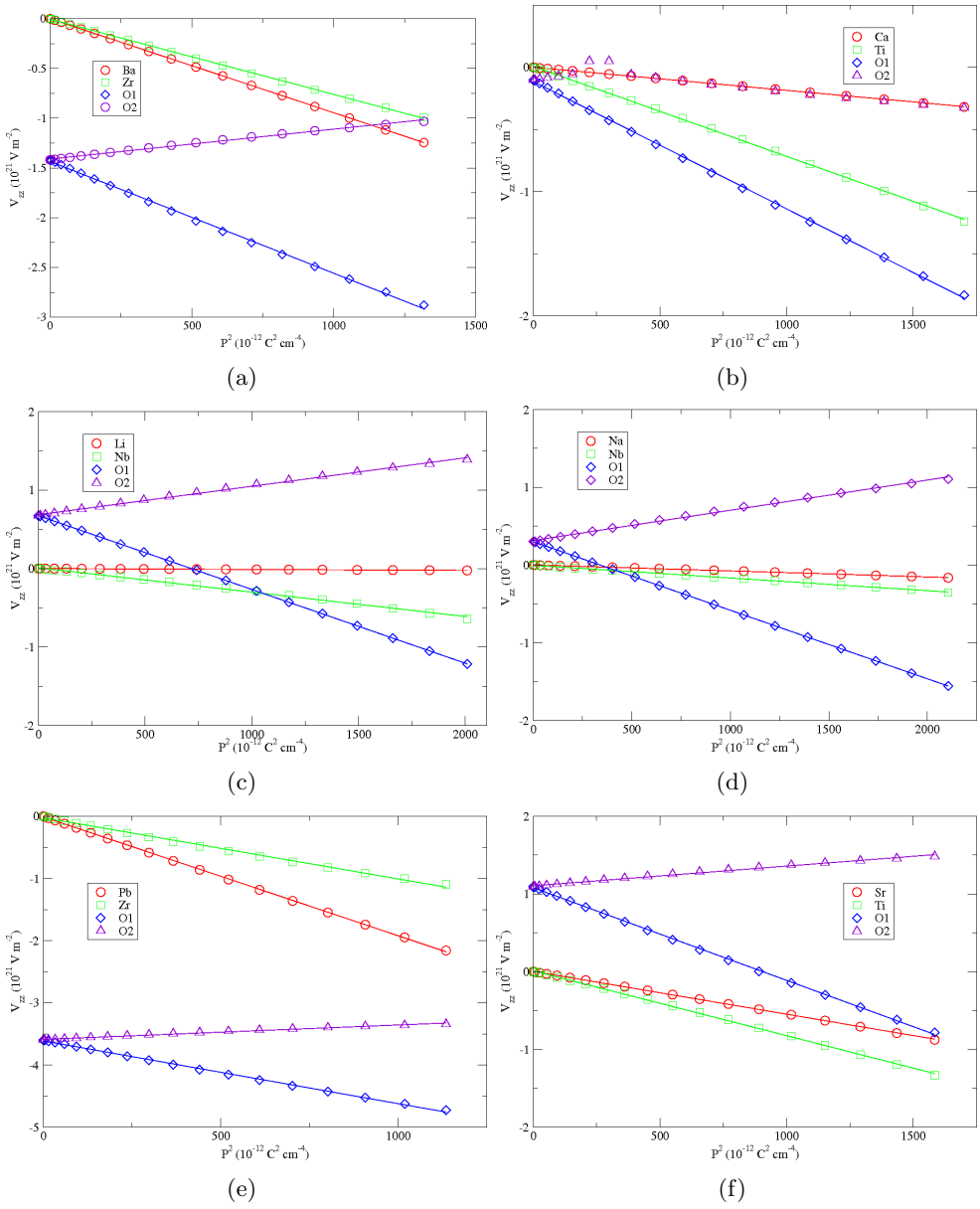

Figure 5.10: V_{zz} of $BaZrO_3$, $CaTiO_3$, $LiNbO_3$, $NaNbO_3$, $PbZrO_3$, $SrTiO_3$, as a function of P^2.

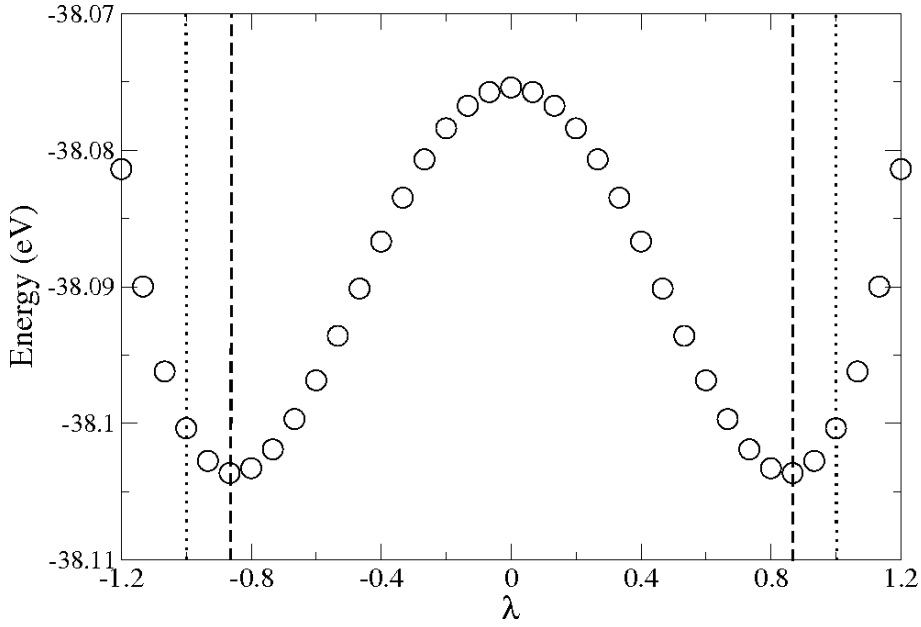

(a)

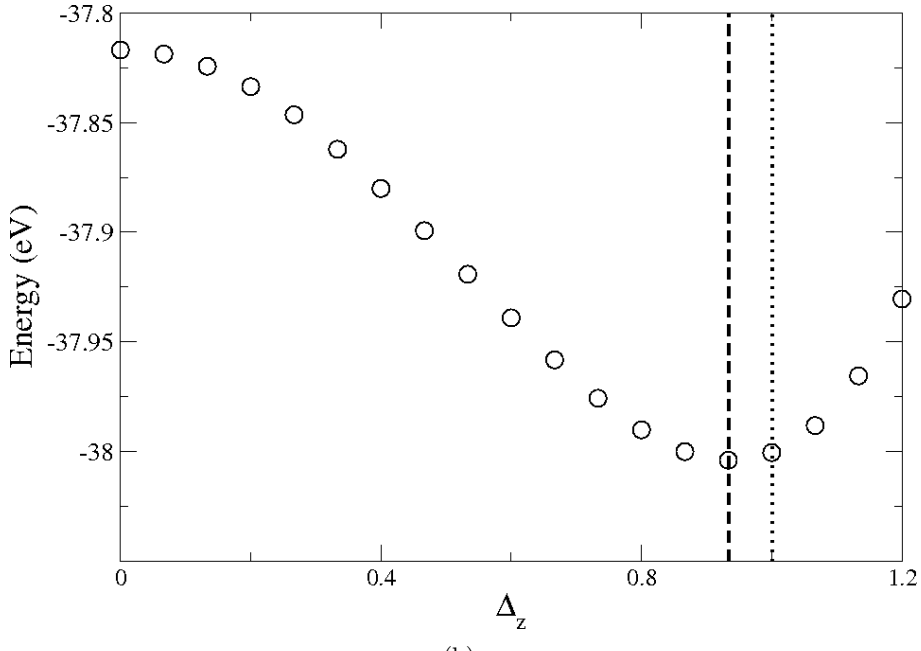

(b)

Figure 5.11: Total energy as a function of the ferroelectric distortion Δ for a) $KNbO_3$ and b) $PbTiO_3$.

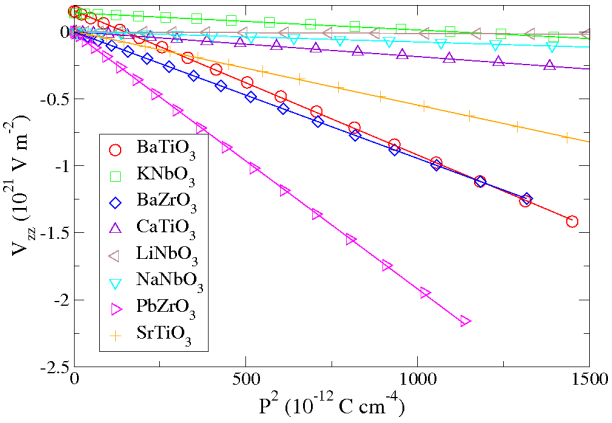

(a)

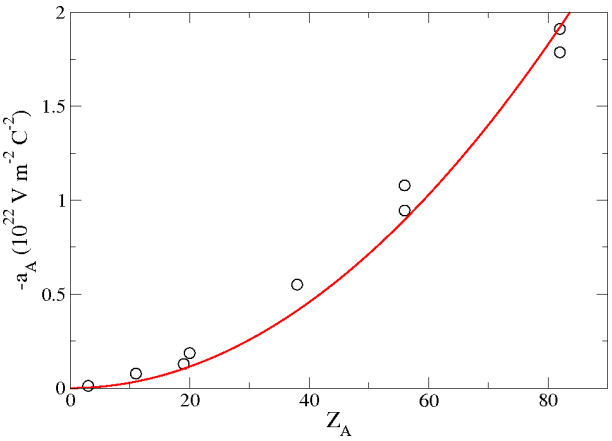

(b)

Figure 5.12: (a) V_{zz} at the A site as a function of P^2, showing the different coefficients (slopes of straight lines). (b) Coefficients of quadratic term of $V_{zz}(P)$, at the A site, for a series of materials with the perovskite structure, as a function of atomic number Z_A. The line is a quadratic fit.

Comparison of $V_{zz}(P)$ in different materials In the following we analyze the relations found in different materials. The quadratic coefficients a in the $V_{zz}(P)$ expression follow an interesting trend with atomic number (Z_A, nuclear charge), shown in figure 5.12. The atoms at the A sites with a larger number of electrons show a larger magnitude of a, that follows a quadratic dependence on Z_A ($V_{zz}(0)$ does not follow any particular trend for the tetragonal structures studied).

Chapter 6

Conclusions

The complementary use of local probe hyperfine interactions experiments with density functional calculations applied to ferroic materials was the main topic of this thesis. The results obtained with different methods complement each other allowing a more confident interpretation of the physical basis behind each situation. The chosen materials show a diversity of behaviors ranging from complicated structural orders, magnetic and electric orders.

The magnetic hyperfine field field worked as a powerful property to the study of the atomic environments in the detailed temperature steps of the irreversible first-order transition in the MnAs compund. The good agreement of calculations with experiments both in manganites and manganese pnictides in general shows the predictive power of density functional theory for the hyperfine measurements. Some exceptions, however, merit further analysis, since they do not appear to conform to the usually considered picture in the simulations of substitutional probes. The approach of using computations as predictions and guides to experiment was also successfully used in the investigation of ferroelectricity and electric field gradients in oxides. In this case, motivated by previous experiments and work in progress, the systematic study of a wide range of compounds allowed the support of previous experimental results and discussions. It also suggests that a more general relationship.

This work shows perspectives for future investigations. The new developments of multiferroism in many bulk and thin film materials, shows a wide variety of cases in which the first-principles calculations are successfully used, and a study of low dimensional materials is also a new avenue for exploration. In the last chapter, only materials with the basic perovskite structure and without magnetic order were studied. It will be interesting to study other materials, e.g. ferroelectric states in sites without inversion symmetry in the paraelectric reference structures, and/or with different types of distortions, or multiferroics where other mechanism for ferroelectricity is at play, and where the influence of magnetic order in the EFG may be large. In this case, one should in first place see if the relationship is still quadratic or not, and how do the values change for different cases. One main objective in the future will be to apply the study of this relationship to previously studied, but more complex cases, such as the $Pr_{1-x}Ca_xMnO_3$ manganite, already with supporting experiments [6].

The following manuscripts are already published and are part of this thesis report:

1. J. N. Gonçalves, H. Haas, A. M. L. Lopes, V. S. Amaral, J. G. Correia. First principles calculations of hyperfine parameters on the Ca manganite with substitutional Cd-modeling of a PAC experiment. Journal of Magnetism and Magnetic Materials. 2010;322(9-12):1170-1173. Proceedings of the Joint European Magnetic Symposia.

DOI: 10.1016/j.jmmm.2009.06.079

2. J. N. Gonçalves, V. S. Amaral, J. G. Correia, A. M. L. Lopes. Hyperfine interactions in MnAs studied by perturbed angular correlations of -rays using the probe $Br^{77} \rightarrow Se^{77}$ and first-principles calculations for MnAs and other Mn pnictides. Physical Review B. 2011;83(10):1-11.

DOI: 10.1103/PhysRevB.83.104421

The following manuscripts are in preparation or submitted for publication at the time of writing, being also included in this thesis report:

1. J. N. Gonçalves, V. S. Amaral, J. G. Correia, H. Haas, A. M. L. Lopes, J. P. Araújo, P. B. Tavares. Hyperfine local probe study of alkaline-earth manganites $BaMnO3_3$ and $SrMnO_3$

2. Hyperfine parameters from first-principles in rare-earth multiferroic hexagonal manganites $RMnO_3$ (R = Y, Ho, Er, Lu). J. N. Gonçalves, V. S. Amaral, J. G. Correia

3. J. N. Gonçalves, A. Stroppa, J. G. Correia, T. Butz, S. Picozzi, and V. S. Amaral. Ferroelectricity and Electric Field Gradients: an ab-initio study.

Other manuscripts with contributions from the author published during the course of the PhD work, not included in this thesis report:

1. T. M. Mendonça, A. M. L. Lopes, J. N. Gonçlves, J. G. Correia, P. B. Tavares, V. S. Amaral, C.show Darie, J. P. Araújo. Perturbed angular correlations investigations on YMnO3 multiferroic manganite. Hyperfine Interactions. 2010;197(1-3):83-88.

DOI: 10.1007/s10751-010-0233-0

2. T. M. Mendonça, J. G. Correia, H. Haas, P. Odier, P. B. Tavares, M. R. da Silva, A. M. L. Lopes, A. M. Pereira, J. N. Gonçalves, J. S. Amaral, C. Darie, J. P. Araújo. Oxygen ordering in the high-T_C superconductor $HgBa_2CaCu_2O_{6+\delta}$ as revealed by perturbed angular correlation. Physical Review B. 2011;84(9):1-10.

DOI: 10.1103/PhysRevB.84.094524

3. A. M. Pereira and E. Kampert and J. M. Moreira and U. Zeitler and J. H. Belo and C. Magen and P. A. Algarabel and L. Morellon and M. R. Ibarra and J. N. Gonçalves and J. S. Amaral and V. S. Amaral and J. B. Sousa and J. P. Araújo, Unveiling the (De)coupling of magnetostructural transition nature in magnetocaloric $R_5Si_2Ge_2$ (R=Tb, Gd) materials. Applied Physics Letters. 2011;99(13):132510.

DOI:10.1063/1.3640213

Bibliography

[1] E. Dagotto, T. Hotta, and A. Moreo. Colossal magnetoresistant materials: the key role of phase separation. *Physics Reports*, 344(1-3):1 – 153, 2001. 1

[2] P. Hohenberg and W. Kohn. Inhomogeneous electron gas. *Phys. Rev.*, 136:B864–B871, 1964. 1, 2.2

[3] W. Kohn and L. J. Sham. Self-consistent equations including exchange and correlation effects. *Phys. Rev.*, 140:A1133–A1138, 1965. 1, 2.2

[4] J. N. Gonçalves, H. Haas, A. M. L. Lopes, V. S. Amaral, and J. G. Correia. First principles calculations of hyperfine parameters on the Ca manganite with substitutional Cd - modeling of a PAC experiment. *Journal of Magnetism and Magnetic Materials, Proceedings of the Joint European Magnetic Symposia*, 322(9-12):1170 – 1173, 2010. 1, 3.2, 3.3.1, 3.3.2, 3.4.2, 4

[5] A. M. L. Lopes, J. P. Araújo, T. M. Mendonça, J. S. Amaral, A. M. Pereira, P. B. Tavares, V. S. Amaral, and J. G. Correia. Studies of local fields in the $Pr_{1-x}Ca_xMnO_3$ system using perturbed angular correlation spectroscopy. *Journal of Non-Crystalline Solids, Proceedings of the 9th International Workshop on Non-Crystalline Solids*, 354(47-51):5315 – 5317, 2008. 1, 3.3.3

[6] A. M. L. Lopes, J. P. Araújo, V. S. Amaral, J. G. Correia, Y. Tomioka, and Y. Tokura. New Phase Transition in the $Pr_{1-x}Ca_xMnO_3$ System: Evidence for Electrical Polarization in Charge Ordered Manganites. *Phys. Rev. Lett.*, 100:155702, 2008. 1, 3.2.2, 3.2.3, 3.3.1, 3.3.2, 3.3.3, 3.3.3, 5, 5.1, 6

[7] J. P. Araújo, A. M. L. Lopes, T. M. Mendonça, E. Rita, J.G. Correia, and V. S. Amaral. Electrical Field Gradient Studies on $La_{1-x}Cd_xMnO_{3+\delta}$ System. *Hyperfine Interactions*, 158:347–351, 2004. 10.1007/s10751-005-9052-0. 1

[8] D. Khomskii. Classifying multiferroics: Mechanisms and effects. *Physics*, 2:20, 2009. 1, 5.1

[9] S.-W. Cheong and M. Mostovoy. Multiferroics: a magnetic twist for ferroelectricity. *Nature materials*, 6(1):13–20, 2007. 1, 5.1

[10] H. L. Yakel, Jnr, W. C. Koehler, E. F. Bertaut, and E. F. Forrat. On the crystal structure of the manganese(III) trioxides of the heavy lanthanides and yttrium. *Acta Crystallographica*, 16(10):957–962, 1963. 1, 3.4.1

[11] V. E. Wood, A. E. Austin, E. W. Collings, and K. C. Brog. Magnetic properties of heavy-rare-earth orthomanganites. *Journal of Physics and Chemistry of Solids*, 34(5):859 – 868, 1973. 1

[12] D. Okuyama, S. Ishiwata, Y. Takahashi, K. Yamauchi, S. Picozzi, K. Sugimoto, H. Sakai, M. Takata, R. Shimano, Y. Taguchi, T. Arima, and Y. Tokura. Magnetically driven ferroelectric atomic displacements in orthorhombic $YMnO_3$. *Phys. Rev. B*, 84:054440, 2011. 1

[13] A. Stroppa and S. Picozzi. Hybrid functional study of proper and improper multiferroics. *Phys. Chem. Chem. Phys.*, 12:5405–5416, 2010. 1

[14] T. M. Mendonça, A. M. L. Lopes, J. N. Gonçalves, J. G. Correia, P. B. Tavares, V. S. Amaral, C. Darie, and J. P. Araújo. Perturbed angular correlations investigations on $YMnO_3$ multiferroic manganite. *Hyperfine Interactions*, 197(1-3):83–88, 2010. 1, 3.4.6

[15] J. N. Gonçalves, V. S. Amaral, J. G. Correia, and A. M. L. Lopes. Hyperfine interactions in MnAs studied by perturbed angular correlations of γ-rays using the probe ^{77}Br$\rightarrow$ ^{77}Se and first-principles calculations for MnAs and other Mn pnictides. *Phys. Rev. B*, 83:104421, 2011. 1

[16] G. Kresse and J. Furthmüller. Efficient iterative schemes for *ab initio* total-energy calculations using a plane-wave basis set. *Phys. Rev. B*, 54:11169–11186, 1996. 1, 2.2

[17] P. Blaha, K. Schwarz, G. K. H. Madsen, D. Kvasnicka, and J. Luitz. *WIEN2k - An Augmented Plane Wave + Local Orbitals Program for Calculating Crystal Properties; www.wien2k.at.* 1, 2.2, 3.2.2, 3.3.2, 4.3

[18] R. King-Smith and D. Vanderbilt. Theory of polarization of crystalline solids. *Physical Review B*, 47(3):1651–1654, 1993. 1, 5, 5.1, 5.2

[19] R. Resta. Macroscopic polarization in crystalline dielectrics: the geometric phase approach. *Reviews of Modern Physics*, 66(3):899–915, 1994. 1, 5, 5.1, 5.2

[20] T. Butz, S. Saibene, T. Fraenzke, and M. Weber. A TDPAC-camera. *Nuclear Instruments and Methods in Physics Research Section A: Accelerators, Spectrometers, Detectors and Associated Equipment*, 284(2-3):417–421, 1989. 2.1, 4.2.1

[21] H. Frauenfelder and R. M. Steffen. *Alpha-, Beta-, and Gamma-Ray Spectroscopy.* North-Holland, 1968. 2.1

[22] G. Schatz and A. Weidinger. *Nuclear Condensed Matter Physics.* Wiley & Sons, Ltd., Sussex, 1996. 2.1, 3.3.3, 4.1, 5.1

[23] N. Barradas, M. Rots, A. Melo, and J. Soares. Magnetic anisotropy and temperature dependence of the hyperfine fields of ^{111}Cd in single-crystalline cobalt. *Physical Review B*, 47(14):8763–8768, 1993. 2.1, 3.3.3, 4.2.2

[24] H. Haas and J. G. Correia. The quadrupole moments of Zn and Cd isotopes – an update. *Hyperfine Interactions*, 198(1):133–137, 2010. 2.1.1, 3.3.3, 4.2.1

[25] K. Schwarz, C. Ambrosch-Draxl, and P. Blaha. Charge distribution and electric-field gradients in $YBa_2Cu_3O_{7-x}$. *Phys. Rev. B*, 42:2051–2061, 1990. 2.1.2

[26] S. Blügel, H. Akai, R. Zeller, and P. H. Dederichs. Hyperfine fields of 3d and 4d impurities in nickel. *Phys. Rev. B*, 35(7):3271–3283, 1987. 2.1.2, 4.3

[27] D. Singh. *Plane waves, pseudopotentials and the LAPW method*. Kluwer Academic, 1994. 2.2.1

[28] P. E. Blöchl. Projector augmented-wave method. *Physical Review B*, 50(24):17953–17979, 1994. 2.2.1, 5.2

[29] G. H. Jonker and J. H. Van Santen. Ferromagnetic compounds of manganese with perovskite structure. *Physica*, 16(3):337 – 349, 1950. 3.1

[30] E. O. Wollan and W. C. Koehler. Neutron Diffraction Study of the Magnetic Properties of the Series of Perovskite-Type Compounds [(1-x)La, xCa]MnO_3. *Phys. Rev.*, 100:545–563, 1955. 3.1, 3.3.2

[31] C. Zener. Interaction Between the d Shells in the Transition Metals. *Physical Review*, 81(3):440–444, 1951. 3.1

[32] C. Zener. Interaction between the d-Shells in the Transition Metals. II. Ferromagnetic Compounds of Manganese with Perovskite Structure. *Physical Review*, 82(3):403–405, 1951. 3.1

[33] R. von Helmolt, J. Wecker, B. Holzapfel, L. Schultz, and K. Samwer. Giant negative magnetoresistance in perovskitelike $La_{2/3}Ba_{1/3}MnO_x$ ferromagnetic films. *Phys. Rev. Lett.*, 71:2331–2333, 1993. 3.1

[34] S. Jin, T. H. Tiefel, M. McCormack, R. A. Fastnacht, R. Ramesh, and L. H. Chen. Thousandfold Change in Resistivity in Magnetoresistive La-Ca-Mn-O Films. *Science*, 264(5157):413–415, 1994. 3.1

[35] I. A. Sergienko, C. Şen, and E. Dagotto. Ferroelectricity in the Magnetic *E*-Phase of Orthorhombic Perovskites. *Phys. Rev. Lett.*, 97:227204, 2006. 3.1

[36] Bernd Lorenz, Ya-Qi Wang, and Ching-Wu Chu. Ferroelectricity in perovskite $HoMnO_3$ and $YMnO_3$. *Phys. Rev. B*, 76:104405, 2007. 3.1

[37] R. Søndenå, S. Stølen, P. Ravindran, T. Grande, and N. L. Allan. Corner- versus face-sharing octahedra in $AMnO_3$ perovskites (A = Ca, Sr, and Ba). *Physical Review B*, 75(18):184105, 2007. 3.2.1, 3.3.1

[38] C. Cardoso, R. P. Borges, T. Gasche, and M. Godinho. *Journal of Physics: Condensed Matter*, (3):035202, 2008. 3.2.1

[39] P. Blaha, K. Schwarz, and P. H. Dederichs. First-principles calculation of the electric-field gradient in hcp metals. *Phys. Rev. B*, 37:2792–2796, 1988. 3.2.1, 5.1

[40] J. G. Correia, H. Haas, V. S. Amaral, A. M. L. Lopes, J. P. Araújo, S. Le Floch, P. Bordet, E. Rita, J. C. Soares, and W. Tröger. Atomic ordering of the fluorine dopant in the $HgBa_2CuO_{4+\delta}$ high-T_c superconductor. *Phys. Rev. B*, 72:144523, 2005. 3.2.1

[41] H. Taguchi, M. Sonoda, and M. Nagao. Relationship between Angles for Mn-O-Mn and Electrical Properties of Orthorhombic Perovskite-Type $(Ca_{1-x}Sr_x)MnO_3$. *Journal of Solid State Chemistry*, 137(1):82–86, 1998. 3.2.2, 3.2.3

[42] L. A. Errico, G. Fabricius, M. Rentería, P. de la Presa, and M. Forker. Anisotropic Relaxations Introduced by Cd Impurities in Rutile TiO_2: First-Principles Calculations and Experimental Support. *Phys. Rev. Lett.*, 89:055503, 2002. 3.2.2

[43] J. P. Perdew, K. Burke, and M. Ernzerhof. Generalized Gradient Approximation Made Simple. *Physical review letters*, 77(18):3865–3868, 1996. 3.2.3, 3.3.2, 4.3, 5.2

[44] Zhigang Wu and R. E. Cohen. More accurate generalized gradient approximation for solids. *Physical Review B*, 73(23):235116, 2006. 3.2.3, 3.3.2

[45] R. M. Sternheimer. Shielding and antishielding effects for various ions and atomic systems. *Phys. Rev.*, 146:140–160, 1966. 3.2.3

[46] F. D. Feiock and W. R. Johnson. Atomic Susceptibilities and Shielding Factors. *Phys. Rev.*, 187:39–50, 1969. 3.2.3, 3.3.2

[47] V. M. Goldschmidt. Die Gesetze der Krystallochemie. *Die Naturwissenschaften*, 14(21):477–485, 1926. 3.3.1

[48] J. J. Adkin and M. A. Hayward. $BaMnO_{3-x}$ Revisited: A Structural and Magnetic Study. *ChemInform*, 38(19):no–no, 2007. 3.3.1, 3.3.2, 3.3.3, 3.3.3

[49] E. J. Cussen and P. D. Battle. Crystal and Magnetic Structures of 2H $BaMnO_3$. *Chemistry of Materials*, 12(3):831–838, 2000. 3.3.1, 3.3.2

[50] B. L. Chamberland, A. W. Sleight, and J. F. Weiher. Preparation and characterization of $BaMnO_3$ and $SrMnO_3$ polytypes. *Journal of Solid State Chemistry*, 1(3-4):506 – 511, 1970. 3.3.1, 3.3.3

[51] A. Hardy. Structures cristallines de deux variétés allotropiques de manganite de baryum. Nouvelle structure ABO_3. *Acta Crystallographica*, 15(3):179–181, 1962. 3.3.1

[52] T. Negas and R. S. Roth. Phase equilibria and structural relations in the system $BaMnO_{3-x}$. *Journal of Solid State Chemistry*, 3(3):323 – 339, 1971. 3.3.1

[53] A. Norlund Christensen and G. Ollivier. Hydrothermal and high-pressure preparation of some $BaMnO_3$ modifications and low-temperature magnetic properties of $BaMnO_3$(2H). *Journal of Solid State Chemistry*, 4(1):131 – 137, 1972. 3.3.1

[54] P. D. Battle, T. C. Gibb, and C. W. Jones. The structural and magnetic properties of $SrMnO_3$: A reinvestigation. *Journal of Solid State Chemistry*, 74(1):60 – 66, 1988. 3.3.1, 3.3.2, 3.3.3

[55] R. Søndenå, P. Ravindran, S. Stølen, T. Grande, and M. Hanfland. Electronic structure and magnetic properties of cubic and hexagonal $SrMnO_3$. *Physical Review B*, 74(14):144102, 2006. 3.3.1

[56] F.F. Fava, P. D'Arco, R. Orlando, and R. Dovesi. A quantum mechanical investigation of the electronic and magnetic properties of $CaMnO_3$ perovskite. *Journal of Physics: Condensed Matter*, 9:489498, 1997. 3.3.1

[57] S. Bhattacharjee, E. Bousquet, and P. Ghosez. Engineering Multiferroism in $CaMnO_3$. *Physical Review Letters*, 102(11):117602, 2009. 3.3.1

[58] J. H. Lee and K. M. Rabe. Epitaxial-Strain-Induced Multiferroicity in $SrMnO_3$ from First Principles. *Phys. Rev. Lett.*, 104:207204, 2010. 3.3.1

[59] J. M. Rondinelli, A. S. Eidelson, and N. A. Spaldin. Non-d^0 Mn-driven ferroelectricity in antiferromagnetic $BaMnO_3$. *Physical Review B*, 79(20):205119, 2009. 3.3.1

[60] H. Sakai, J. Fujioka, T. Fukuda, D. Okuyama, D. Hashizume, F. Kagawa, H. Nakao, Y. Murakami, T. Arima, A. Q. R. Baron, Y. Taguchi, and Y. Tokura. Displacement-Type Ferroelectricity with Off-Center Magnetic Ions in Perovskite $Sr_{1-x}Ba_xMnO_3$. *Phys. Rev. Lett.*, 107:137601, 2011. 3.3.1

[61] P. C. Schmidt, P. D. Das, and A. Weiss. Effect of self-consistency and crystalline potential in the solid state of nuclear quadrupole Sternheimer antishielding factors in closed shell ions. 22:4167–4179, 1980. 3.3.2

[62] K. D. Sen. Nuclear quadrupole Sternheimer shielding-antishielding function for $N3^-$, Cl^- and Cd^{2+} ions in crystals. *Journal of Physics C: Solid State Physics*, 18:3153–3156, 1985. 3.3.2

[63] W. S. Ferreira, J. Agostinho Moreira, A. Almeida, J. P. Araújo, P. B. Tavares, T. M. Mendona, P. Simeo Carvalho, and S. Mendona. Dielectric and Magnetic Properties of $ReMnO_3$ (Re = Eu, Gd) Ceramics. *Ferroelectrics*, 368(1):107–113, 2008. 3.3.3

[64] W. Kraus and G. Nolze. Powdercell for windows, version 2.3. 3.3.3

[65] A. M. L. Lopes, J. P. Araújo, J. J. Ramasco, V. S. Amaral, R. Suryanarayanan, and J. G. Correia. Percolative transition on ferromagnetic insulator manganites: Uncorrelated to correlated polaron clusters. *Physical Review B*, 73(10):1–4, 2006. 3.3.3, 4.5

[66] J. P. Araújo, A. M. L. Lopes, T. M. Mendonça, E. Rita, J. G. Correia, and V. S. Amaral. *Hyperfine Interactions*, 158(1-4):347–351, 2005. 3.3.3

[67] J. P. Araújo, J. G. Correia, V. S. Amaral, P. B. Tavares, J. B. Sousa, J. M. Vieira, and J. C. Soares. *Hyperfine Interactions*, pages 89–94, 2001. 3.3.3

[68] F. Bertaut, F. Forrat, and P. Fang. Les manganites de terres rares et d'yttrium: une nouvelle classe de ferroélectriques. *Comptes Rendus Hebdomadaires des Séances de l'Académie des Sciences*, 256(9):1958–1961, 1963. 3.4.1

[69] G. Nénert, M. Pollet, S. Marinel, G. R. Blake, A. Meetsma, and T. T. M. Palstra. Experimental evidence for an intermediate phase in the multiferroic $YMnO_3$. *Journal of Physics: Condensed Matter*, 19(46):466212, 2007. 3.4.1

[70] Alexandra S. Gibbs, Kevin S. Knight, and Philip Lightfoot. High-temperature phase transitions of hexagonal $YMnO_3$. *Phys. Rev. B*, 83:094111, 2011. 3.4.1

[71] C. J. Fennie and K. M. Rabe. Ferroelectric transition in $YMnO_3$ from first principles. *Phys. Rev. B*, 72:100103, 2005. 3.4.1

[72] Bas B Van Aken, Thomas T M Palstra, Alessio Filippetti, and Nicola A Spaldin. The origin of ferroelectricity in magnetoelectric YMnO3. *Nature materials*, 3(3):164–70, 2004. 3.4.1

[73] R. E. Cohen. Origin of ferroelectricity in perovskite oxides. *Nature*, 358(6382):136–138, 1992. 3.4.1

[74] D.-Y. Cho, J.-Y. Kim, B.-G. Park, K.-J. Rho, J.-H. Park, H.-J. Noh, B.J. Kim, S.-J. Oh, H.-M. Park, J.-S. Ahn, H. Ishibashi, S-W. Cheong, J. Lee, P. Murugavel, T. Noh, A. Tanaka, and T. Jo. Ferroelectricity Driven by Y d_0-ness with Rehybridization in $YMnO_3$. *Physical Review Letters*, 98(21):1–4, 2007. 3.4.1

[75] T. A. Tyson, T. Wu, H. Y. Chen, J. Bai, K. H. Ahn, K. I. Pandya, S. B. Kim, and S. -W. Cheong. Measurements and ab initio Molecular Dynamics Simulations of the High Temperature Ferroelectric Transition in Hexagonal $RMnO_3$. *ArXiv e-prints*, 2011. 3.4.1

[76] Min-Ae Oak, Jung-Hoon Lee, and Hyun Myung Jang. Asymmetric Ho $5d$-O $2p$ hybridization as the origin of hexagonal ferroelectricity in multiferroic $HoMnO_3$. *Phys. Rev. B*, 84:153106, 2011. 3.4.1

[77] S. Blügel, H. Akai, R. Zeller, and P. H. Dederichs. Hyperfine fields of $3d$ and $4d$ impurities in nickel. *Phys. Rev. B*, 35:3271–3283, 1987. 3.4.1, 3.4.2

[78] K. Schwarz. Electronic structure calculations of solids using the WIEN2K package for material sciences. *Computer Physics Communications*, 147(1-2):71–76, 2002. 3.4.1

[79] Peter E. Blöchl, O. Jepsen, and O. K. Andersen. Improved tetrahedron method for brillouin-zone integrations. *Phys. Rev. B*, 49:16223–16233, 1994. 3.4.1

[80] D. D. Koelling and B. N. Harmon. A technique for relativistic spin-polarised calculations. *Journal of Physics C: Solid State Physics*, 10:3107–3114, 1977. 3.4.1

[81] A. H. MacDonald, W. E. Picket, and D. D. Koelling. A linearised relativistic augmented-plane-wave method utilising approximate pure spin basis functions. *Journal of Physics C: Solid State Physics*, 13(14):2675, 1980. 3.4.1, 3.4.2

[82] Łukaszewicz, Kazimierz and Karut-Kalicińska, Jarosława. X-Ray investigations of the crystal structure and phase transitions of $YMnO_3$. *Ferroelectrics*, 7(1):81–82, 1974. 3.4.2

[83] JE Medvedeva, VI Anisimov, and MA Korotin. The effect of Coulomb correlation and magnetic ordering on the electronic structure of two hexagonal phases of ferroelectromagnetic $YMnO_3$. *Journal of Physics:*, 2000. 3.4.2, 3.4.2, 3.4.2, 3.4.3, 3.4.3

[84] C. Zhong, X. Jiang, H. Yu, Q. Jiang, J. Fang, and Z. Li. First-principles studies of the magnetic structure and exchange interactions in the frustrated multiferroic $YMnO_3$. *Journal of Magnetism and Magnetic Materials*, 321(9):1260 – 1265, 2009. 3.4.2, 3.4.2, 3.4.2

[85] J. P. Perdew and Y. Wang. Accurate and simple analytic representation of the electron-gas correlation energy. *Phys. Rev. B*, 45:13244–13249, 1992. 3.4.2

[86] V. Anisimov, I. Solovyev, M. Korotin, M. Czyyk, and G. Sawatzky. Density-functional theory and NiO photoemission spectra. *Physical Review B*, 48(23):16929–16934, 1993. 3.4.2

[87] M. Qian, J. Dong, and Q. Zheng. Electronic structure of the ferroelectromagnet $YMnO_3$. *Physics Letters A*, 270(1-2):96 – 101, 2000. 3.4.2

[88] B. B. van Aken, A. Meetsma, and T. T. M. Palstra. Hexagonal $YMnO_3$. *Acta Crystallographica Section C*, 57(3):230–232, 2001. 3.4.3

[89] I. Rungger and S. Sanvito. Ab initio study of the magnetostructural properties of MnAs. *Physical Review B*, 74(2):024429, 2006. 4.2, 4.1

[90] H. Wada and Y. Tanabe. Giant magnetocaloric effect of $MnAs_{1-x}Sb_x$. *Applied Physics Letters*, 79(20):3302–3304, 2001. 4.1

[91] S. Gama, A. A. Coelho, A. de Campos, A. M. G. Carvalho, F. C. G. Gandra, P. J. von Ranke, and N. A. de Oliveira. Pressure-Induced Colossal Magnetocaloric Effect in MnAs. *Phys. Rev. Lett.*, 93(23):237202, 2004. 4.1

[92] A. de Campos, D. L. Rocco, A. M. G. Carvalho, L. Caron, A. A. Coelho, S. Gama, L. M. da Silva, F. C. G. Gandra, A. O. dos Santos, L. P. Cardoso, P. J. von Ranke, and N. A. de Oliveira. Ambient pressure colossal magnetocaloric effect tuned by composition in $Mn_{1-x}Fe_xAs$. *Nature Materials*, 5(10):802–804, 2006. 4.1

[93] L. Däweritz. Interplay of stress and magnetic properties in epitaxial MnAs films. *Reports on Progress in Physics*, 69(9):2581–2629, 2006. 4.1

[94] M. Ramsteiner, H. Y. Hao, A. Kawaharazuka, H. J. Zhu, M. Kästner, R. Hey, L. Däweritz, H. T. Grahn, and K. H. Ploog. Electrical spin injection from ferromagnetic MnAs metal layers into GaAs. *Phys. Rev. B*, 66(8):081304, 2002. 4.1

[95] L. M. Sandratskii and E. Şaşıoğlu. Unusual sequence of phase transitions in MnAs: First-principles study. *Phys. Rev. B*, 74:214422, 2006. 4.1

[96] M. K. Niranjan, B. R. Sahu, and L. Kleinman. Density functional determination of the magnetic state of β-MnAs. *Physical Review B*, 70(18):180406, 2004. 4.1

[97] P. Ravindran, A. Delin, P. James, B. Johansson, J. M. Wills, R. Ahuja, and O. Eriksson. Magnetic, optical, and magneto-optical properties of MnX (X=As, Sb, or Bi) from full-potential calculations. *Physical Review B*, 59(24):15680, 1999. 4.1, 4.3, 4.4, 4.4

[98] J. Łażewski, P. Piekarz, J. Toboła, B. Wiendlocha, P. T. Jochym, M. Sternik, and K. Parlinski. Phonon Mechanism of the Magnetostructural Phase Transition in MnAs. *Phys. Rev. Lett.*, 104(14):147205, 2010. 4.1

[99] J. Mira, F. Rivadulla, J. Rivas, A. Fondado, T. Guidi, R. Caciuffo, F. Carsughi, P. G. Radaelli, and J. B. Goodenough. Structural Transformation Induced by Magnetic Field and Colossal-Like Magnetoresistance Response above 313 K in MnAs. *Physical Review Letters*, 90(9):097203, 2003. 4.1, 4.2.3

[100] C. P. Bean and D. S. Rodbell. Magnetic Disorder as a First-Order Phase Transformation. *Physical Review*, 126(1):104, 1962. 4.1

[101] J. B. Goodenough and J. A. Kafalas. High-Pressure Study of the First-Order Phase Transition in MnAs. *Physical Review*, 157(2):389, 1967. 4.1, 4.2.3

[102] F. C. Nascimento, A. O. dos Santos, A. De Campos, S. Gama, and L. P. Cardoso. Structural and magnetic study of the MnAs magnetocaloric compound. *Materials Research*, 9:111–114, 2006. 4.1, 4.2.3

[103] R. H. Wilson and J. S. Kasper. The crystal structure of MnAs above 40 degrees C. *Acta Crystallographica*, 17(2):95–101, 1964. 4.1, 4.2.3

[104] F. Ishikawa, K. Koyama, K. Watanabe, and H. Wada. Field Induced Structural Transformation in MnAs. *Japanese Journal of Applied Physics*, 42(Part 2, No. 8A):L918–L920, 2003. 4.1, 4.2.3

[105] F. Ishikawa, K. Koyama, K. Watanabe, and H. Wada. X-ray diffraction study of the structural phase transition in mnas under high magnetic fields. *Physica B: Condensed Matter*, 346-347:408 – 412, 2004. Proceedings of the 7th International Symposium on Research in High Magnetic Fields. 4.1, 4.2.3

[106] S. Gama, A. de Campos, A. A. Coelho, C. S. Alves, Y. Ren, F. Garcia, D. E. Brown, L. M. da Silva, A. Ma. G. Carvalho, F. C. G. Gandra, A. O. dos Santos, L. P. Cardoso, and P. J. von Ranke. A General Approach to First Order Phase Transitions and the Anomalous Behavior of Coexisting Phases in the Magnetic Case. *Advanced Functional Materials*, 19(6):942–949, 2009. 4.1, 4.2.3

[107] B. Kirchschlager, H. Berg, and K. Bärner. Mössbauer spectra of ^{57}Fe in MnAs. *Physics Letters*, 82(1):46–50, 1981. 4.1

[108] M. A. Abdelgadir, L. Häggström, T. Sundqvist, and G. H. Fjellvå. A Mössbauer study of 57 Fe in MnAs. *Physica Scripta*, 37(3):373–380, 1988. 4.1

[109] Y. Amako, H. Nagai, and H. Ido. ^{55}Mn NMR study in $Mn_{1-x}Ti_xAs$. *Journal of Magnetism and Magnetic Materials*, 272-276(Supplement 1):E1617 – E1618, 2004. Proceedings of the International Conference on Magnetism (ICM 2003). 4.1, 4.6.2, 4.16

[110] S. Pinjare and K. Rama Rao. Nuclear magnetic resonance of ^{55}Mn and ^{75}As in MnAs. *Journal of Magnetism and Magnetic Materials*, 30(1):27–32, 1982. 4.1, 4.6.2, 4.16

[111] A. Svane. Calculations of hyperfine parameters in antimony compounds. *Physical Review B*, 68(6):064422, 2003. 4.3

[112] M. Jamal, S. J. Hashemifar, and H. Akbarzadeh. Electric field gradient and magnetic hyperfine field in the bulk and surfaces of α-MnAs compound. *Journal of Magnetism and Magnetic Materials*, 322(24):3841 – 3850, 2010. 4.3, 4.3, 4.8

[113] Yu-Jun Zhao, W. T. Geng, A. J. Freeman, and B. Delley. Structural, electronic, and magnetic properties of α- and β-MnAs: LDA and GGA investigations. *Phys. Rev. B*, 65(11):113202, 2002. 4.3

[114] T. Suzuki and H. Ido. Relation between Structural and Magnetic Properties of Compound $MnAs_{1-x}P_x$ ($0 \leqq x \leqq 0.275$). *Journal of the Physical Society of Japan*, 51(10):3149–3156, 1982. 4.3

[115] D. Torumba, K. Parlinski, M. Rots, and S. Cottenier. Temperature dependence of the electric-field gradient in hcp-Cd from first principles. *Physical Review B*, 74(14):1–6, 2006. 4.3

[116] K. S. Liang and T. Chen. X-Ray Photo-Emission Study of Transition-Metal Antimonides. *Solid State Communications*, 23(12):975978, 1977. 4.4

[117] Y. Yamaguchi and H. Watanabe. Magnetic polarization of anions in MnAs and MnSb. *Journal of Magnetism and Magnetic Materials*, 31-34(Part 2):619 – 620, 1983. 4.8

[118] K. Katoh, A. Yanase, and K. Motizuki. Electronic band structures of NiAs-type transition metal compounds. *Journal of Magnetism and Magnetic Materials*, 54-57(Part 2):959 – 960, 1986. 4.8

[119] P. M. Oppeneer, V. N. Antonov, T. Kraft, H. Eschrig, A. N. Yaresko, and A. Ya. Perlov. First-principles study of the giant magneto-optical Kerr effect in MnBi and related compounds. *Journal of Applied Physics*, 80(2):1099–1105, 1996. 4.8

[120] J. Bouwma, C. van Bruggen, C. Haas, and B. Van Laar. Neutron diffraction and magnetic properties of $Mn_{1+x}Sb_{1-y}Sn_y$. *Physica*, (2):78–80, 1971. 4.8

[121] T. Chen, G. B. Charlan, and R. C. Keezer. Growth of MnSb single crystals by pulling with a seed from nonstoichiometric molten solution. *Journal of Crystal Growth*, 37(1):29 – 36, 1977. 4.8

[122] N. Vast, B. Siberchicot, and P. G. Zerah. First-principles calculation of the magnetocrystalline anisotropy energy of the pnictide MnSb. *Journal of Physics: Condensed Matter*, 4(50):10469–10478, 1992. 4.8

[123] R. Coehoorn, C. Haas, and R. A. de Groot. Electronic structure of MnSb. *Phys. Rev. B*, 31(4):1980–1996, 1985. 4.8

[124] R. Podloucky. Electronic structure of MnSb. *Solid State Communications*, 50(8):763 – 767, 1984. 4.8

[125] Li Zhiqiang, Luo Helie, Lai Wuyan, Zeng Zhi, and Zheng Qingqi. Electronic structure and magnetic properties of MnBi(Al,Nd). *Solid State Communications*, 79(10):791 – 794, 1991. 4.8

[126] Tu Chen and W. Stutius. The phase transformation and physical properties of the MnBi and $Mn_{1.08}Bi$ compounds. *Magnetics, IEEE Transactions on*, 10(3), 1974. 4.8

[127] R. R. Heikes. Magnetic Transformation in MnBi. *Phys. Rev.*, 99(2):446–447, 1955. 4.8

[128] J. Köhler and J. Kübler. Calculated magneto-optical properties of pure and doped MnBi. *Physica B: Condensed Matter*, 237-238:402 – 406, 1997. 4.8

[129] C. Narasimha Rao. Investigation of spin reorientation phenomena in ferromagnetic MnSb by NMR. *Journal of Magnetism and Magnetic Materials*, 50(1):107–110, 1985. 4.4

[130] H. Koyama, K. Nagamine, N. Nishida, K. Tanaka, and T. Yamazaki. Nuclear orientation of Bi isotopes in a ferromagnetic BiMn compound. *Hyperfine Interactions*, 5(1):2744, 1977. 4.4

[131] N. Menyuk, J. A. Kafalas, K. Dwight, and J. B. Goodenough. Effects of Pressure on the Magnetic Properties of MnAs. *Physical Review*, 177(2):942, 1969. 4.15

[132] V. Bhide and M. Multani. Mössbauer Effect for Fe57 in Ferroelectric BaTiO3. II. The Vacancy-Impurity Associated State. *Physical Review*, 149(1):289–295, 1966. 5, 5.1

[133] T. Oja and P. Casabella. Nuclear-Magnetic-Resonance Studies of Ferroelectricity in Normal and Irradiated Rochelle Salt. *Physical Review*, 177(2):830–838, 1969. 5, 5.1

[134] D. Dening. Nuclear quadrupole coupling constants and spontaneous polarization in ferroelectrics. *Journal of Magnetic Resonance (1969)*, 38(2):277–282, 1980. 5.1, 5.2, 5, 5.1, 5.3.1

[135] Y. Yeshurun. Static and dynamic aspects of perturbed angular correlation measurements in perovskite crystals. *Solid State Communications*, 27(2):181–184, 1978. 5, 5.1

[136] K. Rabe, C. H. Ahn, and J.-M. Triscone, editors. *Physics of Ferroelectrics: A Modern Perspective*. Springer, 2007. 5.1

[137] P. Blaha, K. Schwarz, and P. Herzig. First-Principles Calculation of the Electric Field Gradient of Li_3N. *Physical Review Letters*, 54(11):1192–1195, 1985. 5.1

[138] P. Blaha and K. Schwarz. A full-potential LAPW study of structural and electronic properties of beryllium. *Journal of Physics F: Metal Physics*, 17(4):899, 1987. 5.1

[139] P. Blaha and K. Schwarz. Electric field gradient in Cu_2O from band structure calculations. *Hyperfine Interactions*, 52:153–159, 1989. 5.1

[140] C. Ambrosch-Draxl, P. Blaha, and K. Schwarz. Electric-field gradient calculations for $YBa_2Cu_3O_{7-x}$. *Journal of Physics: Condensed Matter*, 1(27):4491, 1989. 5.1

[141] C. Ambrosch-Draxl, P. Blaha, and K. Schwarz. Electronic structure and electric-field gradients for $YBa_2Cu_4O_8$ from density-functional calculations. *Phys. Rev. B*, 44:5141–5147, 1991. 5.1

[142] P. Blaha, D. J. Singh, P. I. Sorantin, and K. Schwarz. Electric-field-gradient calculations for systems with large extended-core-state contributions. *Phys. Rev. B*, 46:1321–1325, 1992. 5.1

[143] M. Fitzgerald and P. Casabella. NMR Study of Phase Transitions in Rochelle Salt. *Physical Review B*, 2(5):1350–1354, 1970. 5.1

[144] M. Fitzgerald and P. Casabella. Temperature Dependence of the Na^{23} Quadrupole Coupling Constants in Rochelle Salt. *Physical Review B*, 7(5):2193–2195, 1973. 5.1

[145] Y. Yeshurun. Temperature dependence of the electric quadrupole interaction in $PbHfO_3$. *Journal of Physics and Chemistry of Solids*, 40(3):231–237, 1979. 5.1

[146] R. King-Smith and D. Vanderbilt. First-principles investigation of ferroelectricity in perovskite compounds. *Physical Review B*, 49(9):5828–5844, 1994. 5.2, 5.1

[147] G. H. Kwei, A. C. Lawson, S. J. L. Billinge, and S. W. Cheong. Structures of the ferroelectric phases of barium titanate. *The Journal of Physical Chemistry*, 97(10):2368–2377, 1993. 5.1, 5.3.2

[148] G. Shirane, R. Newnham, and R. Pepinsky. Dielectric Properties and Phase Transitions of $NaNbO_3$ and (Na,K)NbO_3. *Physical Review*, 96(3):581–588, 1954. 5.1

[149] A. W. Hewat. Soft modes and the structure, spontaneous polarization and Curie constants of perovskite ferroelectrics: tetragonal potassium niobate. *Journal of Physics C: Solid State Physics*, 1074(6):1074, 1973. 5.1

[150] S. A. Mabud. Lattice parameters and birefringence in $PbTiO_3$ single crystals. *Journal of Applied Crystallography*, pages 49–53, 1979. 5.1

[151] W. F. Nelmes. The crystal structure of tetragonal $PbTiO_3$ at room temperature and at 700 K. *Solid State Communications*, (8):721–723, 1985. 5.1

[152] R. Resta, M. Posternak, and A. Baldereschi. Towards a quantum theory of polarization in ferroelectrics: The case of $knbo_3$. *Phys. Rev. Lett.*, 70:1010–1013, 1993. 5.3.1

[153] G. Czjzek. Distribution of nuclear quadrupole splittings in amorphous materials and the topology of the (V_{zz}, η)-parameter space. *Hyperfine Interactions*, 14:189–194, 1983. 10.1007/BF02043468. 5.3.3

[154] T. Butz, M. Ceolín, P. Ganal, P. Schmidt, M. A. Taylor, and W. Tröger. A new approach in nuclear quadrupole interaction data analysis: cross-correlation. *Physica Scripta*, 54(3):234–239, 1996. 5.3.3

[155] T. Butz. How to analyse powder nuclear quadrupole interaction data with non-axial symmetry for interdependent electric field gradient tensor components. *Physica Scripta*, 82(2):025702, 2010. 5.3.3